

Imaging Mass Spectrometry of *Staphylococcus aureus* Infection:
Mapping Pathogenic Adaptations that Circumvent Immunity

By

William Joseph Perry

Dissertation

Submitted to the Faculty of the
Graduate School of Vanderbilt University
in partial fulfillment of the requirements
for the degree of

DOCTOR OF PHILOSOPHY

In

Chemistry

August 31, 2020

Nashville, Tennessee

Approved:

Richard M. Caprioli, Ph.D.

Eric P. Skaar, Ph.D., M.P.H.

Jeffrey M. Spraggins, Ph.D.

John A. McLean, Ph.D.

Kevin L. Schey, Ph.D.

Copyright © 2020 by William Joseph Perry

All Rights Reserved

ACKNOWLEDGEMENTS

I would like to thank all who assisted me on my educational endeavors. I would not have completed this journey without the support of my mentors and loved ones. Thank you to Drs. Richard Caprioli, Eric Skaar, and Jeff Spraggins. I have been fortunate enough to be led by three talented and intellectual individuals. Thank you to my committee members, Drs. Kevin Schey and John McLean, for challenging me and pushing me to excel. I am thankful have worked alongside such helpful, caring colleagues and friends in both the Caprioli and Skaar laboratories. Without the frequent laughs and occasional happy hour trips, I am sure that my experience at Vanderbilt would have become quite humdrum. Specifically, I thank Dr. Andy Weiss for educating me in *S. aureus* biology and being my constant confidant in translational research, Dr. Daniel Ryan for his words of reality, and Emilio Rivera for his friendship that reminded me of my home. To Mom, Dad, and Adam, I am thankful for your unquestionable love and never-ending support. From our constant conversations to our occasional arguments, I would not be here without you. To my partner Megan (and our wiener dogs), you have served as my rock and voice of reason. I look forward to our future endeavors. With you alongside, I am confident that we (Copper and Romeo included) can conquer the world. For all other loved ones and friends, thank you all for the support, comradery, late nights, and questionable decisions. Finally, I am to end my experience with a quote: “Finish each day and be done with it. You have done what you could. Some blunders and absurdities no doubt crept in; forget them as soon as you can. Tomorrow is a new day. You shall begin it serenely and with too high a spirit to be encumbered with your old nonsense” – Ralph Waldo Emerson.

TABLE OF CONTENTS

	Page
ACKNOWLEDGEMENTS	iii
LIST OF FIGURES	vii
LIST OF TABLES	ix
LIST OF ABBREVIATIONS	x
Chapter	
I. INTEGRATED MOLECULAR IMAGING AND APPLICATIONS TO INFECTION	
Overview	1
Insight into Biological Processes through Application of Molecular Imaging Modalities	3
Matrix-Assisted Laser Desorption/Ionization and Imaging Mass Spectrometry	4
<i>Time-of-Flight Mass Spectrometry</i>	6
<i>Fourier Transform Ion Cyclotron Resonance Mass Spectrometry</i>	8
<i>Sample Preparation Considerations for Imaging Mass Spectrometry</i>	11
<i>MALDI Matrix Selection and Application</i>	13
Elemental Imaging Modalities for the Investigation of Metal Content and Distributions	16
Applications of MALDI IMS to Infections by <i>Staphylococcus aureus</i>	19
Use and Utility of Fluorescence and Autofluorescence Microscopy in Multimodal Imaging	25
Applications of Integrating Multiple 2-Dimensional Molecular Imaging Modalities	25
Research Summary and Objectives	30
II. UNCOVERING MATRIX EFFECTS ON LIPID ANALYSES IN MALDI IMAGING MASS SPECTROMETRY EXPERIMENTS	
Overview	31
Introduction	32
Results	34
<i>Matrix Effects on Positive Ion Mode Lipid Analysis</i>	34
<i>Matrix Effects on Negative Ion Mode Lipid Analysis</i>	44
Discussion	52
Methods	53
<i>Materials and Sample Preparations</i>	53
<i>Imaging Mass Spectrometry</i>	54
<i>Data Analysis</i>	56

III. VISUALIZATION OF *STAPHYLOCOCCUS AUREUS* PATHOGENIC MEMBRANE MODIFICATION WITHIN THE INFECTION ENVIRONMENT BY A MULTIMODAL IMAGING MASS SPECTROMETRY APPROACH

Overview	59
Introduction	59
Results	62
<i>Differential Distributions of S. aureus Lysyl-PGs are observed within Murine Abscesses</i> ...	62
<i>S. aureus Lysyl-PGs and Host Cationic Antimicrobial Peptides are Present in Human Endocarditis Infections</i>	67
Discussion	73
Methods	75
<i>Materials</i>	75
<i>Bacterial Strains and Growth Conditions</i>	75
<i>Murine Model Procedures</i>	76
<i>Patients and Endocarditis Vegetations</i>	76
<i>Sample Preparation</i>	77
<i>Fluorescence Microscopy Image Acquisition</i>	77
<i>Molecular Image Acquisition and Visualization</i>	78
<i>Data-driven Image Fusion</i>	80
<i>Protein Extraction for LC-MS/MS</i>	80
<i>LC-MS/MS Data Acquisition and Analysis</i>	81

IV. *STAPHYLOCOCCUS AUREUS* EXHIBITS HETEROGENEOUS SIDEROPHORE PRODUCTION WITHIN THE VERTEBRATE HOST

Overview	82
Introduction	82
Results	84
<i>Comparison of Surface Coatings to Visualize Siderophores within Infected Tissue</i>	84
<i>Multimodal Imaging Mass Spectrometry to Visualize Nutritional Heterogeneity</i>	85
<i>Comparing Siderophore Distributions across Abscesses within Multiple Tissue Types</i>	89
Discussion	92
Methods	93
<i>Bacterial Strains and Growth Conditions</i>	93
<i>Animal Procedures</i>	93
<i>Materials and Sample Preparations</i>	94
<i>Fluorescence Microscopy Image Acquisition and Data Analysis</i>	95
<i>Molecular Image Acquisition and Data Analysis</i>	96
<i>Elemental Image Acquisition and Data Analysis</i>	97

V. CONSPECTUS

Overview	98
MALDI Matrix Influence on Analyte Observation.....	99

Multimodal Imaging Approaches to Investigate Bacterial Pathogenesis.....	100
Molecular Heterogeneity of <i>Staphylococcus aureus</i> Infections.....	102
Future Directions: Applications of Integrating Multiple 3-Dimensional Molecular Imaging Modalities.....	103
Concluding Remarks	106
REFERENCES.....	108
CURRICULUM VITAE	121

LIST OF FIGURES

Figure	Page
1.1 MALDI Schematic.....	5
1.2 MALDI IMS Schematic.....	6
1.3 MALDI Time-of-Flight Mass Analyzer	8
1.4 Fourier Transform Ion Cyclotron Resonance Mass Analyzer.....	10
1.5 MALDI IMS Sample Preparation.....	11
1.6 Laser Ablation Inductively Coupled Plasma Mass Spectrometry	19
1.7 <i>Staphylococcus aureus</i> Tissue Abscess Morphology	21
1.8 MALDI FT-ICR IMS Isotopic Resolution of Proteoforms and Elemental Context to the Host-Pathogen Interface	24
1.9 Overview of Recent Studies Employing Elemental Imaging in 2D	27
1.10 Data-Driven Image Fusion Applied to MALDI FT-ICR IMS of Intact Proteins from a <i>S. aureus</i> Infected Murine Renal Tissue Section.....	29
2.1 Comparisons of Positive Ion Mode Lipid Analyses Using Several MALDI Matrices.....	36
2.2 PCA of Positive Ion Mode Data for Several MALDI Matrices.....	38
2.3 Positive Ion Mode Heat Maps to Compare Lipid Abundances	40
2.4 DHA Positive Ion Mode Heat Maps to Compare Matrix Application Methods	42
2.5 Positive Ion Mode Ion Images to Visually Compare Lipid Presence and Abundance.....	44
2.6 Comparisons of Negative Ion Mode Lipid Analyses Using Several MALDI Matrices.....	46
2.7 PCA of Negative Ion Mode Data for Several MALDI Matrices	48
2.8 Negative Ion Mode Heat Maps to Compare Lipid Abundances.....	49

2.9 DAN Matrix Results in Modifications to Phosphatidylcholine Lipids During Negative Ion Mode Analysis	50
2.10 Negative Ion Mode Ion Images to Visually Compare Lipid Presence and Abundance	51
2.11 Bioinformatics Workflow to Compare the Lipid Sensitivity and Specificity of Several MALDI Matrices	58
3.1 MALDI IMS Informed by Bacterial Fluorescent Reporters Isolates <i>S. aureus</i> Lipids	65
3.2 MALDI MS/MS Profiling of Lysyl-phosphatidylglycerol Lipids at Sites of Infection	66
3.3 Tissue Stains from an Infection Model using a <i>S. aureus</i> Genetic Mutant Inactivated for Lysyl-phosphatidylglycerol Production.....	67
3.4 <i>S. aureus</i> Lysyl-phosphatidylglycerol Lipids from Human Infective Endocarditis Tissue.....	69
3.5 Single Extracted Spectra from MALDI IMS of Human Infective Endocarditis Tissue	70
3.6 Averaged IMS Spectrum of Intact Protein Distributions from Human Infective Endocarditis Tissue	71
3.7 MALDI IMS of Intact Proteins and Subsequent LC-MS/MS Analysis from Human Infective Endocarditis Tissue.....	72
4.1 IMS Surface Coatings Comparison for Visualization of Staphyloferrin A Siderophore.....	85
4.2 IMS of <i>S. aureus</i> Siderophores and Fe to Investigate Nutritional Immunity	87
4.3 Confirmation of Staphyloferrin A using a <i>S. aureus</i> Genetic Mutant	88
4.4 Multimodal IMS to Visualize Nutritional Immunity across Tissue Lesions	91
5.1 Overview of Recent Studies Employing Elemental Imaging in 3D	106

LIST OF TABLES

Table	Page
1.1 Common MALDI Matrices and Uses.....	15
2.1 MALDI Matrix Spray Application Parameters.....	54
3.1 Image Fusion Data Mining Results.....	64
3.2 <i>S. aureus</i> Strain, Plasmids, and Primers Used	76

LIST OF ABBREVIATIONS

Δsfa : A *S. aureus* mutant genetically inactivated for staphyloferrin A production

2D: 2 dimensional

2MeN: 2-methyl amino phospholipid head group

3D: 3 dimensional

9AA: 9-aminoacridine

AF: Autofluorescence microscopy

AmF: Ammonium formate buffer

Ar: Argon

ArO: Argon oxide

AUC: Area under the receiver operating characteristic curve

B: Magnetic field strength

BLI: Bioluminescent imaging

CA-MSSA: Community acquired- methicillin sensitive *Staphylococcus aureus*

CAMP: Cationic antimicrobial peptide

cDHA: (E)-4-(2,5-dihydroxyphenyl)but-3-en-2-one

CFU: Colony forming units

CMBT: 5-chloro-2-mercaptobenzothiazole

CMC: Carboxymethylcellulose

CP: Calprotectin

d: Distance

Da: Dalton

DABP: 3,4-diaminobenzophenone

DAN: 1,5-diaminonaphthalene

DHA: 2,5-dihydroxyacetophenone

DHB: 2,5-Dihydroxybenzoic acid

DPI: Days post infection

ESI: Electrospray ionization

FDR: False discovery rate

Fe: Iron

FFPE: Formalin fixed paraffin embedded

FT-ICR: Fourier transform ion cyclotron resonance

FTIR: Fourier transform infrared spectroscopy

Fur: Ferric uptake regulator

GFP: Green fluorescent protein

H&E: Hematoxylin and eosin

Hz: Hertz

IHC: Immunohistochemistry

IMS: Imaging mass spectrometry

ICP: Inductively coupled plasma

isdA: A *S. aureus* gene whose expression increases upon Fe starvation

ITO: Indium-tin-oxide

K_d : Dissociation constant

KE: kinetic Energy

LA: Laser ablation

LC: Liquid chromatography

Lysyl-PG: a bacterial phosphatidylglycerol lipid species modified with a lysine amino acid to the glycerol headgroup

m/z: Mass-to-charge ratio

m: mass of an ion

MALDI: Matrix-assisted laser desorption ionization

mntA: A *S. aureus* gene whose expression increases upon manganese starvation

mprF: Multiple peptide resistance factor

MRI: Magnetic resonance imaging

MS: Mass spectrometry

MS/MS: Tandem mass spectrometry

Nd:YAG: Neodymium-doped yttrium aluminum garnet

Nd:YLF: Neodymium-doped yttrium lithium fluoride

NET: Neutrophil extracellular trap

nm: Nanometer

OD_{600nm}: Optical density at 600 nm

OCT: Optimal cutting temperature

PBS: Phosphate buffered saline

PCA: Principle component analysis

P_{isdA}gfp: A strain of *S. aureus* where green fluorescent protein expression is driven from the Fur-regulated *isdA* promoter

P_{mntA}rfp: A strain of *S. aureus* where red fluorescent protein expression is driven by the *mntA* promoter

PMN: Polymorphonuclear neutrophil

ppm: Parts per million

q: Charge

R: Resolving power

r: Radius

RFP: Red fluorescent protein

ROC: Receiver operating characteristic curve

ROS: Reactive oxygen species

SAC: Staphylococcal abscess community

SIMS: Secondary ion mass spectrometry

T: Tesla

t: Time

TMGN: 1,8-bis(tetramethylguanidino)naphthalene

TOF: Time-of-flight

TSA: Tryptic Soy Broth

TSB: Tryptic Soy Agar

UV: Ultraviolet

V: Voltage

V_{pp} : Peak to peak voltage

XFI: X-ray fluorescence imaging

XRF: X-ray fluorescence microscopy

z: Charge

λ : Wavelength

μ CT: Micro-computed tomography

μ m: Micrometer

μ XFI: Micro-X-ray fluorescence imaging

μ XRF: Micro-X-ray fluorescence microscopy

v : Velocity

v_c : Cyclotron frequency

ω_c : Angular frequency

CHAPTER I

Integrated Molecular Imaging and Applications to Infection

A version of the following chapter was previously published and has been adapted from Perry et al., *Current Opinion in Chemical Biology*, Copyright 2020 by Elsevier¹, and from McMillen, Perry, et al., *Proceedings of the NATO Advanced Study Institute in Rapid Threat Detection*, Copyright 2020 by Springer.²

Overview

Human infection and disease are rooted in chemical changes at or below the cellular level. Many of the causative chemical changes that result in potentially deadly conditions localize to specific structures or cells within tissues such as cancerous tumors or infectious foci. The complex matrix of tissue makes it challenging to detect, characterize, and localize chemical changes to diagnose adverse health and prescribe a therapeutic. Use of modern analytical technologies to obtain and visualize molecular information demonstrate their worth in clinical and hospital settings. Specifically, matrix-assisted laser desorption/ionization mass spectrometry (MALDI MS) has revolutionized the research, diagnostic, and clinical microbiology communities, allowing measurement of analytes from complex samples with high levels of sensitivity and reproducibility. An advance of MALDI MS allows for the visualization of molecular distributions from tissue sections, termed imaging mass spectrometry (IMS). MALDI IMS has been applied to a variety of biological samples, defining chemical changes associated with disease.

Many technologies exist to acquire information from a tissue section, varying in resultant data complexity. However, there is currently no technique that captures elemental, molecular, and

morphological information in a single experiment. To fully characterize complex biological interactions or processes within tissue environments, multiple levels of information must be obtained and combined. Many critical developments have been made towards correlative multimodal imaging. Recent efforts to apply molecular imaging approaches in tandem with anatomical, morphological, or elemental imaging modalities have placed a precedent on how multimodal strategies can provide insight to biological systems. Specifically, decreased pixel sizes without the sacrifice of molecular or elemental information have allowed for subcellular localization of analytes, complemented and spatially verified by other imaging modalities. Increased acquisition speeds of molecular imaging technologies have allowed feasibility of large 3-dimensional (3D) data volumes. The utility of these approaches is highlighted by the broad nature of studies that employ multiple imaging strategies, reaching from basic physiology and plant biology to various human diseases including bacterial infections. However, the combination of imaging information still faces many challenges, including registration, alignment, 3D volume constructions, and data analysis. Implementation of accurate registration techniques, data fusion, and data analysis automation to 2-dimensional (2D) and 3D imaging approaches will not only lessen analysis times, but also increase the use of multiple imaging strategies throughout the scientific community. Nevertheless, the wealth of elemental, molecular, and morphological information acquired through the combination of imaging modalities, outweighs the technical challenges and allows unparalleled insight into biological systems.

Insight into Biological Processes through Application of Molecular Imaging Modalities

Tissue imaging strategies can provide morphological or molecular information allowing the study of complex biological systems. Among the strategies that can be interfaced, histology using color stains (*e.g.*, hematoxylin and eosin (H&E)) is the most basic and allows for the determination of gross tissue morphologies and cellular differentiation.³ Immunohistochemistry (IHC) relies on antibody-based staining, targeting specific antigens within a tissue section.⁴ Visualization of fluorophore-conjugated antibodies using fluorescence microscopy offers advantages over traditional IHC, including the potential for multiplexing through use of multiple fluorophores with different emission/excitation spectra. A further expansion of immunostaining incorporates heavy metal-conjugated antibodies, termed imaging mass cytometry. This experimental strategy allows the application of up to 30 antibody tags to be analyzed in a single experiment, although with limited throughput due to extensive data acquisition times.⁵ In addition to using histological or antibody-based methods to characterize a tissue of interest, fluorescent or bioluminescent reporters can be employed and detected via fluorescent microscopy or *in vivo* (3D) bioluminescent imaging (BLI). Transcriptional or translational reporter constructs can be designed to address an array of biological questions and can help delineate the cellular, organellar, or molecular makeup of a sample in question.

Additional methods are available and frequently employed to allow unbiased and unlabeled analysis of tissues. For example, Fourier transform infrared spectroscopy (FTIR) results in a spectral “fingerprint” of a sample without providing specific biochemical information. Here, infrared radiation directed on a sample is absorbed through transitions in molecular vibrational energy states to be recorded as a spectrum.⁶

IMS is a technology that can map the distribution of thousands of molecular analytes directly from a tissue sample without *a priori* knowledge.⁷ Amongst a variety of molecular IMS sampling/ionization techniques, MALDI IMS is the most common, and the number of published studies using this technology suggests that it is the most robust.⁷⁻⁹ Recent studies have leveraged MALDI IMS as a discovery approach in tandem with other imaging modalities to probe various biological systems, many comprised of multiple organisms.¹⁰⁻¹³

Matrix-Assisted Laser Desorption/Ionization and Imaging Mass Spectrometry

MALDI is an ionization technique that relies on the presence of a low molecular weight, organic molecule, termed a matrix, with strong ultraviolet (UV) absorbance. Analytes co-crystallized with a matrix solution are irradiated by a UV laser, facilitating desorption and ionization. Many small aromatic, organic compounds can be employed as MALDI matrices. Matrices are typically categorized based on their efficiency to assist in the desorption and ionization of a broad molecular class of analytes (*e.g.*, low molecular weight metabolites, lipids, proteins, polymers, and inorganic compounds) when irradiated with a UV laser. While any UV wavelength laser can be used to generate ions with MALDI with varying efficiency, solid state lasers are most commonly employed, such as frequency tripled neodymium-doped yttrium aluminum garnet (Nd:YAG, 355 nm) and neodymium-doped yttrium lithium fluoride (Nd:YLF, 349 nm). Post laser irradiation, gaseous ions are separated based on mass-to-charge ratio (m/z) using a mass analyzer, detected, and recorded as a mass spectrum. A schematic of this ionization technique is present in Figure 1.1. MALDI MS can be used to measure a variety of biological analytes, ranging from small metabolites to intact proteins. The rapid ability to analyze complex

mixtures with limited sample preparation has resulted in MALDI MS present in many clinics and diagnostic settings.

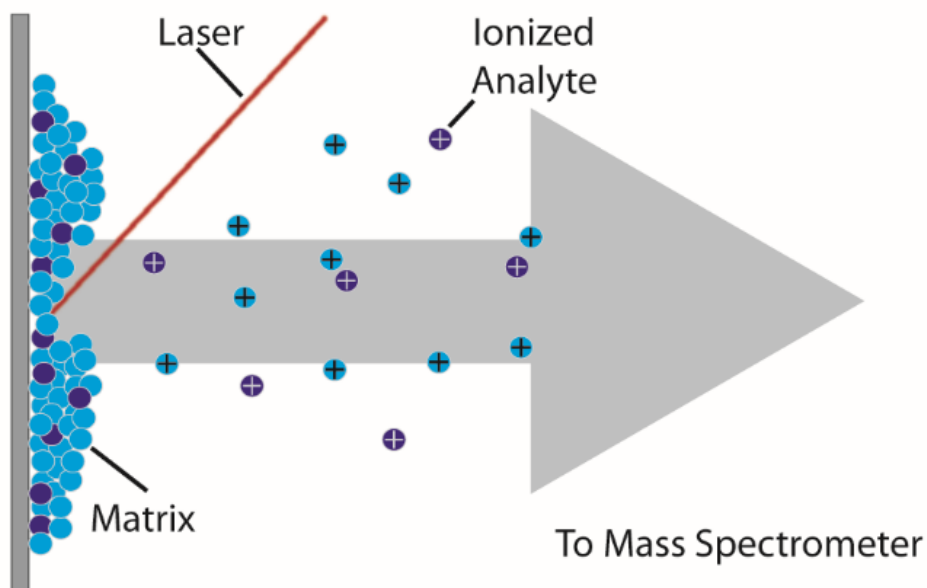


Figure 1.1: MALDI Schematic

A schematic depicts matrix-assisted laser desorption/ionization. A UV laser, depicted as a red line, irradiates a co-crystallized mixture of analyte and matrix molecules, represented as purple and blue circles, respectively. The matrix molecules absorb the laser energy to facilitate the desorption and/or generation of ions from the surface. Ions are then transmitted and measured using a mass spectrometer. Desorption of neutral molecules is not shown.

MALDI MS can be leveraged to allow the visualization of molecular distributions within thin tissue sections, termed MALDI IMS. In MALDI IMS, a tissue section is homogeneously coated with a crystallized matrix. The raster of the sample surface with a UV laser allows for acquisition of mass spectra at discrete x,y positions. Following acquisition, intensity maps of molecular distributions can be generated for any ion of interest. Both the laser incident spot size on the prepared sample and the pitch between positions determine the spatial resolution of the resultant IMS data set and the pixel sizes of the ion image. Using this technology, ions can be mapped to specific areas within a tissue section.¹⁴

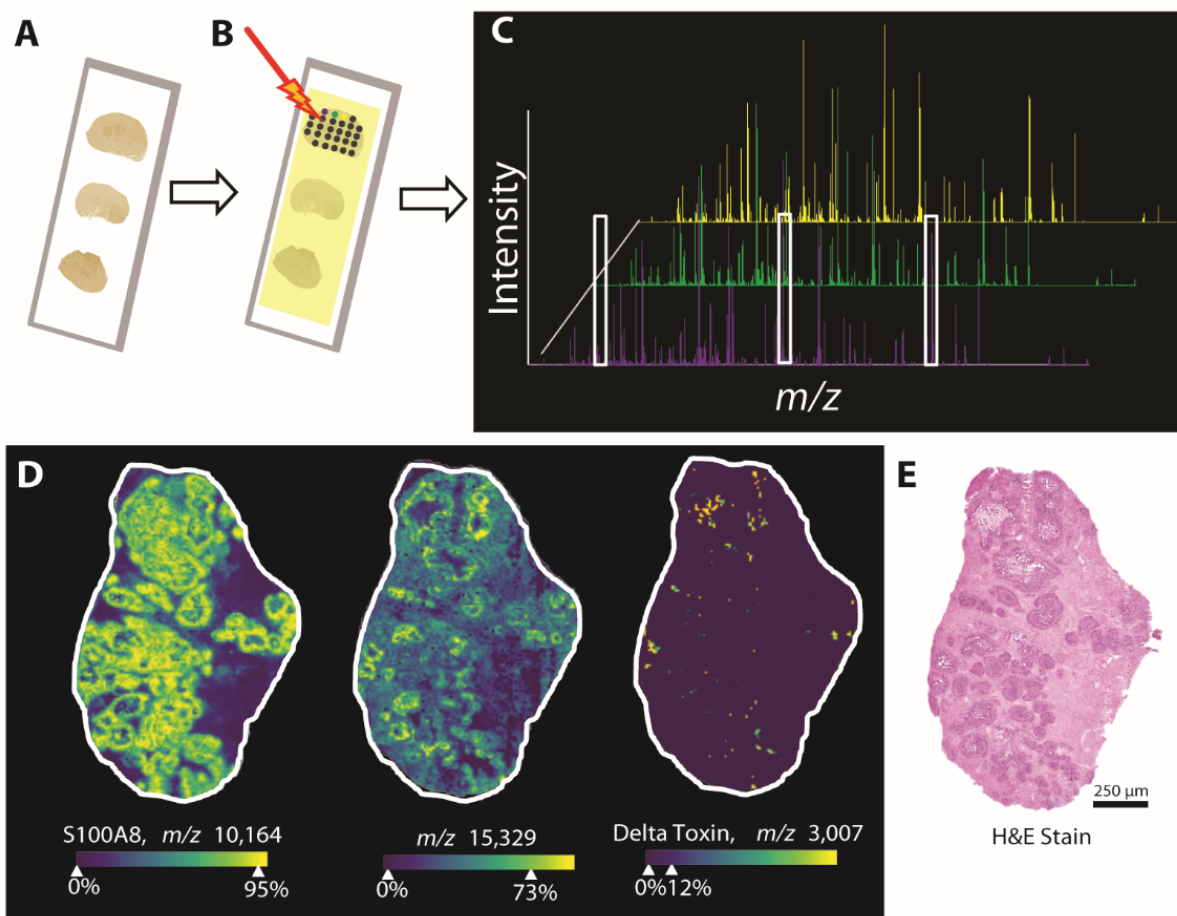


Figure 1.2: MALDI IMS Schematic

Schematic depicting steps to acquire and visualize MALDI IMS. (A) Sample preparation begins with thinly sectioning a tissue to mount on a conductive microscope slide. (B) A matrix solution is homogeneously deposited on the tissue. The sample is then irradiated by a UV laser at discrete x/y locations. (C) Ions are recorded as mass spectra. (D) Ion images can be generated for any ion of interest from mass spectra, identified or unknown. (E) After IMS acquisition, tissue sections can be washed of matrix and stained to compare tissue morphology with molecular distributions.

Time-of-Flight Mass Spectrometry

Most commercial MALDI mass spectrometers employ a time-of-flight (TOF) mass analyzer, Figure 1.3. A TOF mass analyzer measures m/z values based on the time that it takes an ion to traverse a field-free region or flight tube. The components of a TOF mass analyzer are relatively limited in comparison to other mass analyzers and consist of an accelerating electrode, a field-free drift region, and a detector. All ions are given the same starting kinetic energy by an

accelerating electrode. As ions traverse the field-free region, varying velocities based on the m/z value will result in a separation of the ions in time. Kinetic energy (KE) is defined as the product of the charge (z) and the accelerating voltage (V).

$$KE = zV$$

This product can then be set equal to the traditional definition of KE, where the mass of an ion (m) is multiplied by the velocity (v).

$$KE = zV = \frac{mv^2}{2}$$

The velocity of the ions can be further defined by the distance (d) traveled over time (t). Rearrangement of the equation after substitution of these parameters allows the time-of-flight to determine an m/z value since the distance traveled and the accelerating voltage are constant.¹⁵

$$t = d \sqrt{\frac{m}{2zV}}$$

Due to their relatively low cost, high duty cycle, and theoretically infinite mass range, MALDI TOF mass spectrometers are the most common instrumental platform used to acquire IMS data. Newer generation MALDI TOF mass spectrometers now allow for routine IMS data acquisition at a spatial resolution of 10 μm and at speeds of 10,000 laser shots per second; however, the resolving power (R) or ability to separate two ions of similar m/z values of TOF mass spectrometers is relatively low in comparison to other mass analyzers at approximately 10,000.¹⁶

$$R = \frac{M}{\Delta M}$$

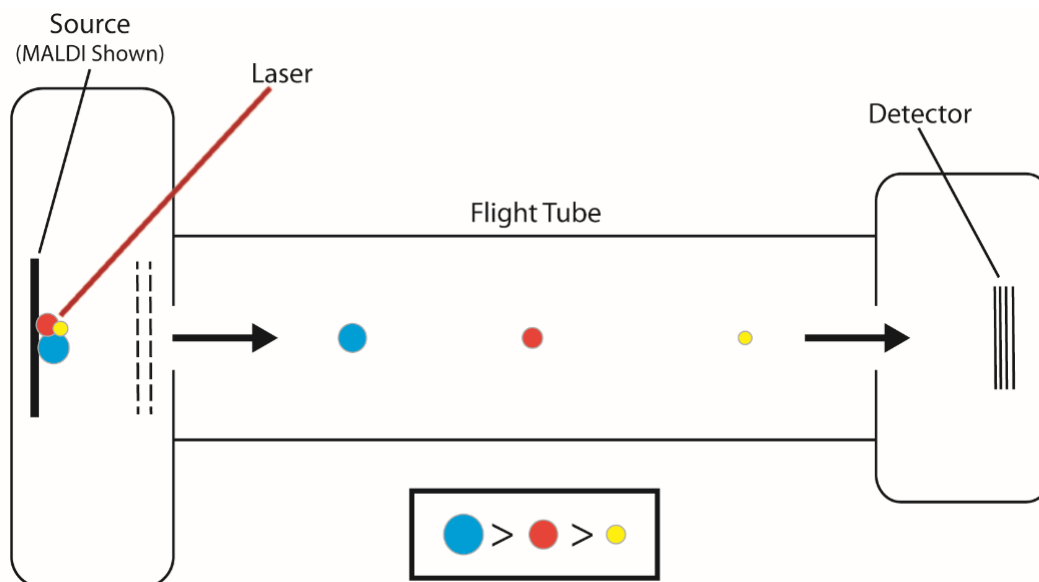


Figure 1.3: MALDI Time-of-Flight Mass Analyzer

A schematic depicts a MALDI linear time-of-flight mass spectrometer. Ions are generated using MALDI and accelerated by a high voltage grid. Ions are separated based on their velocities through a field free region to be detected as a mass-to-charge ratio and recorded as a mass spectrum.

Fourier Transform Ion Cyclotron Resonance Mass Spectrometry

A MALDI ion source can be incorporated on virtually any instrumental platform to allow for IMS, including high performance instruments such as Fourier transform ion cyclotron resonance (FT-ICR) mass spectrometers. FT-ICR mass analyzers allow the highest mass resolution and measurement accuracy, with a resolving power capable of reaching >1 million. This mass analyzer consists of an ICR cell centered within the uniform magnetic field of a superconducting magnet. Analysis of ions within the cell relies on three forces. Ions are injected into the cell where they experience a Lorentz force as they perpendicularly move in the direction of the magnetic field, where (m) is the mass of the ion, (q) is the charge, (v) is the velocity, (B) is the magnetic field strength, and (t) is time.

$$\text{Force} = m \times \text{acceleration} = m \frac{dv}{dt} = qv \times B$$

Ions orbit the cell in a radius (r) proportional to the magnetic field strength, with a frequency that is directly proportional to the m/z value of the ion, or the third force which is the cyclotron frequency. The unperturbed cyclotron frequency, or one where no collisions with other ions take place can be defined, where (ν_c) is the cyclotron frequency, (ω_c) is the angular frequency, (m/z) is the mass-to-charge ratio, and (B) is the field strength of the magnetic field.

$$\nu_c = \frac{\omega_c}{2\pi} = \frac{1.535611 \times 10^7 B}{\frac{m}{z}}$$

A schematic of FT-ICR mass analysis is shown in Figure 1.4. The ICR cell consists of two trapping plates to axially confine ions. The walls of the cell consist of excitation and detection plates. A radio frequency that matches the cyclotron frequency of ions is applied to the excitation plates. The radii of ions expand upon excitation and acceleration, resulting in a detectable signal. As excited ions orbit the cell, an image current is induced on the detection plates, allowing measurement in a time domain signal. A Fourier transform to the time domain signal results in a frequency spectrum. The measured frequencies can then be converted to a mass spectrum by a mass correlation.¹⁷

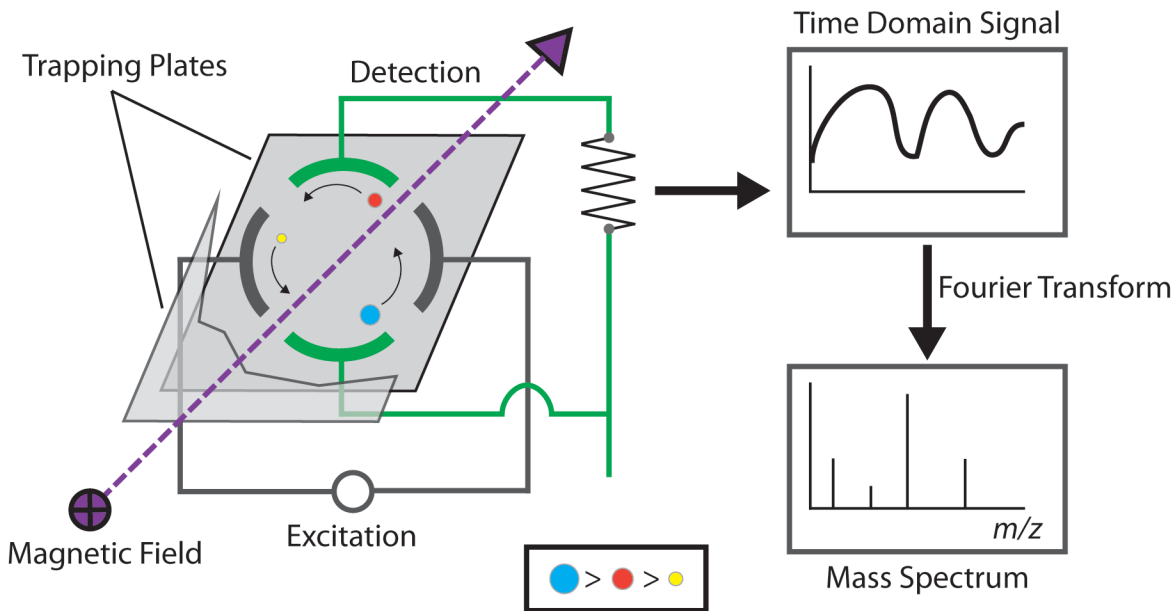


Figure 1.4: Fourier Transform Ion Cyclotron Resonance Mass Analyzer

A schematic represents mass analysis by a Fourier transform ion cyclotron resonance mass spectrometer. Ions undergo cyclotron motion within a uniform magnetic field, where they are excited using a radio frequency and detected using perpendicular electronic plates. An obtained time domain signal undergoes a Fourier transform to produce a frequency domain spectrum. A mass correlation or the frequency domain spectrum results in a mass spectrum.

A single ion can be measured multiple times by an FT-ICR mass spectrometer after an ion generation event, resulting in high accuracy measurements after signal averaging. This is increasingly important for IMS, where the chemical content from one specific location to another can be highly variable. The ability to measure this content with high resolving power and accuracy through multiple measurements is an overwhelming advantage when compared to a TOF mass analyzer; however, FT-ICR MS analyses can take up to seconds from a single ion generation event. This results in significantly longer data acquisition times when compared to a TOF mass spectrometer. Instrumental parameters should be considered for each experiment, selecting the instrument to most accurately and quickly answer a hypothesis.

Sample Preparation Considerations for Imaging Mass Spectrometry

IMS is highly dependent on the quality of sample preparation. Many factors must be taken into account when preparing a sample, including tissue stabilization or preservation, embedding material, the washing procedure, matrix choice, and matrix application method.¹⁸ An example workflow consists of tissue sectioning, an optional washing procedure, matrix application, and an optional recrystallization procedure (Figure 1.5). The primary goal of any sample preparation is to minimize analyte delocalization and degradation while maximizing sensitivity.¹⁹ Sample preparation protocols are typically developed for specific tissue types and analytes of interest, although common methods and protocols can be established.²⁰⁻²⁴

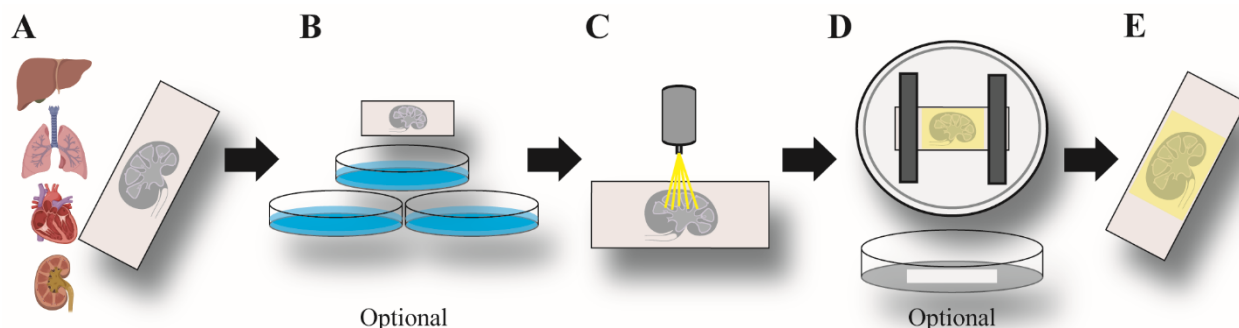


Figure 1.5: MALDI IMS Sample Preparation

A schematic depicts common sample preparation procedures for imaging mass spectrometry. (A) Biological tissues are thinly sectioned, and then mounted onto conductive microscope slides. (B) Sections may undergo optional washing protocols to select for analytes of interest or lessen chemical interferences. (C) MALDI matrix is homogeneously applied to a sample using a robotic aerosol sprayer. (D) An optional recrystallization procedure can be applied to samples when needed to ensure analyte-matrix layer co-crystallization. (E) Prepared samples are ready when needed for IMS analysis. Reprinted from *Proceedings of the NATO Advanced Study Institute in Detection, diagnosis, and health concerns of toxic chemical and biological agents*, 2019, “Matrix-assisted laser desorption/ionization imaging mass spectrometry: technology and applications” with permission from Springer Publishing Company.²

Sample preparation of formalin fixed tissue begins by sectioning to 10-12 μm thickness and thaw mounting onto a conductive microscope slide (Figure 1.5A).²⁵ Fixation, offering the most accurate morphological tissue representation, is performed by incubating a harvested tissue in a paraformaldehyde solution for up to 7 days. Intramolecular crosslinks are formed between proteins during this incubation. The fixed tissue is then submerged in paraffin wax and is termed formalin fixed paraffin embedded (FFPE) tissue. While this method allows ambient storage, the fixative can induce unwanted chemical artifacts.²⁶ These artifacts can compromise analysis of metabolites, lipids, and intact proteins. However, some studies observe limited MS effects after paraffin removal or alternative procedures.²⁷⁻²⁹ For proteins, developed protocols utilize proteolytic digestion of FFPE tissues and subsequent peptide analysis.^{21, 30} Fresh frozen tissues are preferred for IMS.²⁵ However, freezing can induce morphological changes to a tissue. Histological stains of fresh frozen tissue sections are typically inferior to those of FFPE sections.

For fresh frozen preservation, a tissue is cryosectioned prior to thaw mounting onto a slide. Optimal cutting temperature (OCT) compound may be used to improve section quality. However, OCT compound contains a polymer that introduces high intensity ions during MS analysis that can significantly complicate mass spectra. Tissue washing procedures have been shown to lessen or remove OCT artifacts, but these washes may also wash away compounds of interest.¹⁹ Other materials have been purposed as embedding materials with limited MS effects, including carboxymethylcellulose (CMC) and gelatin.^{31, 32} Use of these materials typically introduces minimal effects, while still assisting in sectioning.

Washing can remove potential chemical interferences and select for specific analytes (Figure 1.5B).^{19, 30, 33, 34} Ammonium formate (AmF) buffer is used to remove salts from tissue for the analysis of lipids.³⁰ In the positive ion mode, protonated ions dominate the spectra after AmF

tissue washing. Decreased salt presence also increases sensitivity in the negative ion mode. Sensitivity for intact proteins can be increased by removing both lipids and salts from tissue using Carnoy's fluid (ethanol, chloroform, and acetic acid), water, and ethanol.¹⁹ Recently washes have been developed to select for metabolites.^{33,34} Chloroform and acetone washes remove hydrophobic lipids, leaving behind many water soluble metabolites. Washes may delocalize some molecules, so care and validation are recommended. Other washes are being developed to either select or analyze analytes of interest or eliminate chemical interferences.³⁵⁻³⁹

MALDI Matrix Selection and Application

MALDI matrices are chosen based on their ability to provide sufficient ionization efficiency for a given analyte class (*e.g.* low molecular weight metabolites, lipids, proteins, polymers, or organometallics). A MALDI matrix is typically a small, organic molecule consisting of a UV absorbing chemical moiety. Differences in observed analyte sensitivities can be attributed to the physical properties of a matrix such as molecular structure, pH, proton affinity, and peak wavelength absorbance.^{18, 40-47} However, several studies have successfully employed various inorganic materials such as nanoparticles or thin layers of metals.⁴⁸ 2,5-dihydroxybenzoic acid (DHB) is widely employed as a MALDI matrix, offering sufficient sensitivities for many analyte classes in positive ion mode MS analysis.^{46, 49, 50} 9-Aminoacridine (9AA) is often used for the analysis of metabolites in negative ion mode and 1,5-diaminonaphthalene (DAN) for lipids with high sensitivity in both polarities.^{18, 47} However, the energy transferred during the ablation process can result in analyte modification or fragmentation, complicating data interpretation.^{49, 51} Volatility is also a consideration when selecting a MALDI matrix because the matrix layer must remain stable for lengthy acquisition times (hours) to avoid signal loss during an imaging experiment. 2,5-

Dihydroxyacetophenone (DHA) is an excellent matrix for MS analysis of multiple analyte classes; however, its high volatility limits acquisition times.⁴⁰ (E)-4-(2,5-dihydroxyphenyl)but-3-en-2-one (cDHA) is a vacuum stable matrix providing high sensitivity for lipids, peptides, and intact proteins.⁴¹ Table 1.1 lists many commonly used matrices.

Matrix	Other Names	Chemical Structure	Application
(E)-4-(2,5-dihydroxyphenyl)but-3-en-2-one	2,5-cDHA		Lipids Peptides Proteins Positive and Negative Ionization Modes
2,5-dihydroxyacetophenone	2,5-DHA		Lipids Peptides Proteins Positive and Negative Ionization Modes
9-Aminoacridine	9-AA		Low Molecular Weight Metabolites Lipids Negative Ionization Mode
α -Cyano-4-hydroxycinnamic acid	CHCA		Peptides Proteins Positive Ionization Mode
5-Chloro-2-mercaptobenzothiazole	CMBT		Lipids Peptides Positive and Negative Ionization Modes
1,5-Diaminonaphthalene	DAN		Lipids Positive and Negative Ionization Modes
trans-2-[3-(4-tert-Butylphenyl)-2-methyl-2-propenylidene]malononitrile	DCTB		Carbohydrates Polymers Inorganic Materials Organometallics Positive and Negative Ionization Modes
2,5-Dihydroxybenzoic acid	DHB		Low Molecular Weight Metabolites Pharmaceuticals Lipids Positive Ionization Mode
3,5-Dimethoxy-4-hydroxycinnamic acid	Sinapic Acid		Peptides Proteins Positive Ionization Mode
2',4',6'-Trihydroxyacetophenone	THAP		Carbohydrates Nucleic Acids Lipids Peptides Positive and Negative Ionization

Table 1.1: Commonly Used MALDI Matrices

Table 1.1 lists common MALDI matrices and typical applications to analyze analyte classes. Reprinted from *Proceedings of the NATO Advanced Study Institute in Detection, diagnosis, and health concerns of toxic chemical and biological agents*, 2019, “Matrix-assisted laser desorption/ionization imaging mass spectrometry: technology and applications” with permission from Springer Publishing Company.²

The method of MALDI matrix application can dictate crystal size, analyte extraction, and analyte delocalization (Figure 1.5C). MALDI matrices are most commonly applied by either aerosol spray or sublimation. Aerosol application can be accomplished using an airbrush sprayer or more homogeneously and reproducibly using a robotic sprayer. Temperature, gas flow, and solvent composition all influence analyte extraction and unwanted delocalization. Ideally, matrix application is wet enough to ensure analyte extraction yet does not induce analyte delocalization. Optimal matrix concentration and deposition density are determined empirically, and delocalization is evaluated by MS acquisition off tissue.⁵² Matrix application by sublimation has been shown to produce small crystal sizes.⁵³ However, sublimation does not provide the level of analyte extraction achieved by aerosol spray. A recrystallization procedure can assist analyte extraction after matrix application by sublimation (Figure 1.5D).¹⁹ Any slight variation in sublimation time or temperature can impact the amount of matrix deposited, affecting reproducibility. Therefore, sublimation is not commonly used for large sample cohorts.^{19, 30, 40, 54} Sample preparation and matrix selection are important considerations when developing a method for IMS analysis.

Elemental Imaging Modalities for the Investigation of Metal Content and Distributions

Metals play a pivotal role in biology and are required by approximately 40% of enzymes for proper function.⁵⁵ This dependency is largely due to the unique inorganic and electronic properties of transition metals, supporting a myriad of functions in their proteinaceous clients. As such, transition metals have been studied extensively, and metallomics has emerged as a rapidly expanding field.⁵⁶ Metals must be obtained externally to maintain sufficient cellular or organismal pools. However, metal levels must also be strictly regulated to prevent toxicity at high

concentrations. Disruption of metal homeostasis can have detrimental effects on an organism, and various neurodegenerative and cardiovascular diseases as well as cancers have been associated with alterations in metal levels.⁵⁷⁻⁶⁰ Analogous to eukaryotic systems, bacterial pathogens rely on metals to replicate.⁶¹ In response to the broad importance of metals in biologic systems, analytical technologies have emerged for metal analysis and imaging. Elemental imaging technologies allow visualization of both distributions and relative abundances of metals within tissue samples.⁶² Imaging studies have focused on many aspects of metal biology, ranging from analysis of individual metalloproteins to complex pathways in mammalian organ systems.

A variety of strategies can be used to visualize metals within a thin tissue section.⁶² Stains and chemical probes are the most basic and accessible reagents to enable visualization of endogenous metals within a tissue section. Here, introduction of chemicals to the surface of a tissue enables metal observation by either a visual or fluorescent signature. Chemicals required for this type of visualization typically select for only one elemental species and vary in sensitivity.³

An unbiased and more sensitive method to simultaneously image multiple metals is X-ray fluorescence (XRF). This technology relies on atomic excitation and relaxation principles. In XRF, an atom is excited by an electron, proton, or photon (X-ray) beam. Multiple elements can then be identified and quantified by the light emitted upon relaxation. Depending on the specific adaptation of these principles, distinct modalities can allow for subcellular resolution (*e.g.*, micro X-ray fluorescence microscopy (μ XRF), electron probe X-ray microanalysis, particle induced x-ray emission, and synchrotron X-ray fluorescence microscopy). Resultant XRF datasets can be represented as false colored images, termed X-ray fluorescence imaging (XFI).⁶³⁻⁶⁵

Metal ion analysis is routinely accomplished using inductively coupled plasma (ICP)-MS. Using this ionization strategy, a high energy plasma is used to produce elemental ions from a

sample. A plasma is generated using a radio frequency to excite argon (Ar) gas. This ion source simultaneously eliminates molecular structures and most chemical interferences; however, polyatomic interferences persist or are formed.⁶⁶ Specifically, many Ar clusters, such as argon oxide (ArO), are present and introduce spectral interferences with many ions. Two strategies exist to overcome polyatomic interferences. The first is to use a higher resolving power instrument such as a high field dual sector MS. As an example, the most abundant isotopes of ArO (m/z 56.970) and Fe (m/z 56.942) require a resolving power of roughly 2,550 to separate the ions. The second strategy is to disrupt polyatomic ion presence. This is accomplished using a collision gas chamber prior to entrance to the mass spectrometer. This is a highly effective strategy and allows for the use of a lower resolving power mass spectrometer, such as a linear ion trap; however, collisions with neutral gas can lessen the abundance of ions of interest. Both strategies to limit polyatomic ion interferences have been successfully coupled to a laser ablation (LA) stage to measure endogenous metals from a tissue section. A LA stage can sample specific x,y locations across a surface using a high energy UV laser. This laser is commonly a quintupled Nd:YAG (213 nm). A sample is ablated in a sealed chamber at a specific location to be carried to an ICP-MS by an inert gas. IMS can be conducted by performing systematic ablations and MS measurements across a sample, or LA-ICP IMS, Figure 1.6.^{67, 68}

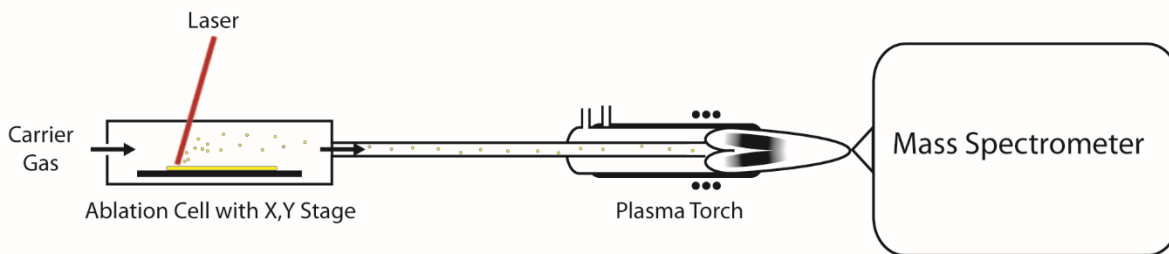


Figure 1.6: Laser Ablation Inductively Coupled Plasma Mass Spectrometry

A schematic depicts laser ablation inductively coupled plasma mass spectrometry. Material is ablated from specific x,y locations to be carried to a plasma torch by an inert gas. Material ionized by the torch is analyzed by a mass spectrometer.

Secondary ion mass spectrometry (SIMS) is an MS-based technology that enables imaging of metals from a tissue section with subcellular spatial resolution. High energy primary ions generated by an ion gun are targeted to specific x,y locations on the sample surface. Impact of the primary ions both eject and facilitate the formation of secondary ions to be analyzed by MS.^{69, 70} Although the spatial resolution of SIMS surpasses that achievable with LA-ICP IMS (e.g., $\sim 1 \mu\text{m}$ / pixel with LA-ICP IMS and $\sim 500 \text{ nm}$ / pixel with SIMS), few metallic species ionize using SIMS.^{14, 67, 69}

Applications of MALDI IMS to Infections by *Staphylococcus aureus*

Antibiotic-resistant bacteria are no longer confined to healthcare settings.⁷¹ Isolated from many community settings, resistant strains of *Staphylococcus aureus* are a public health threat that cause an estimated 40,000 deaths per year in the United States alone.⁷²⁻⁷⁴ Infections by *S. aureus* can cause life-threatening illnesses, ranging from soft tissue infections to systemic conditions such as sepsis.⁷⁵ Infections present with architecture consisting of staphylococcal abscess communities (SACs) segregated from normal tissue by layers of healthy and necrotic polymorphonuclear neutrophils (PMNs) in structures termed abscesses (Figure 1.7).⁷⁶ Unique molecules co-localize with host and pathogen pathological features of *S. aureus* tissue abscesses.^{76, 77} Upon recognition

of a pathogen, a vertebrate host will deploy mechanisms of immunity. These mechanisms vary from innate immune pathogen killing to more specialized responses, such as nutrient metal sequestration in processes known as nutritional immunity.⁷⁸⁻⁸¹ Alternatively, *S. aureus* has evolved virulence factors to allow for proliferation within a host. Inhibitive, evasive, or defensive biochemical responses contribute to the success of *S. aureus* as a pathogen.⁸²

Mechanisms of *S. aureus* infectious disease progression and proliferation are not fully understood. Abscesses observed in murine models vary in size, time of formation, and organ occupancy. Abscess formation and bacterial proliferation in a murine model of infection have been previously described in four stages: survival of *S. aureus* in the blood, preparation of a tissue lesion site, crisis and disease, and persistence until rupture into the peritoneal cavity.⁷⁶ Consistent host responses to the pathogen include the migration of immune response cells to segregate and combat the microorganisms by various mechanisms. (*e.g.*, phagocytosis, neutrophil extracellular traps (NETs), and an encompassing layer of fibrin and extracellular matrix).^{76, 83-85} New studies have shown the host-pathogen interface, once thought to be a stagnant environment consisting of necrosis and cell death, to be a highly dynamic cellular environment.^{84, 86-88}

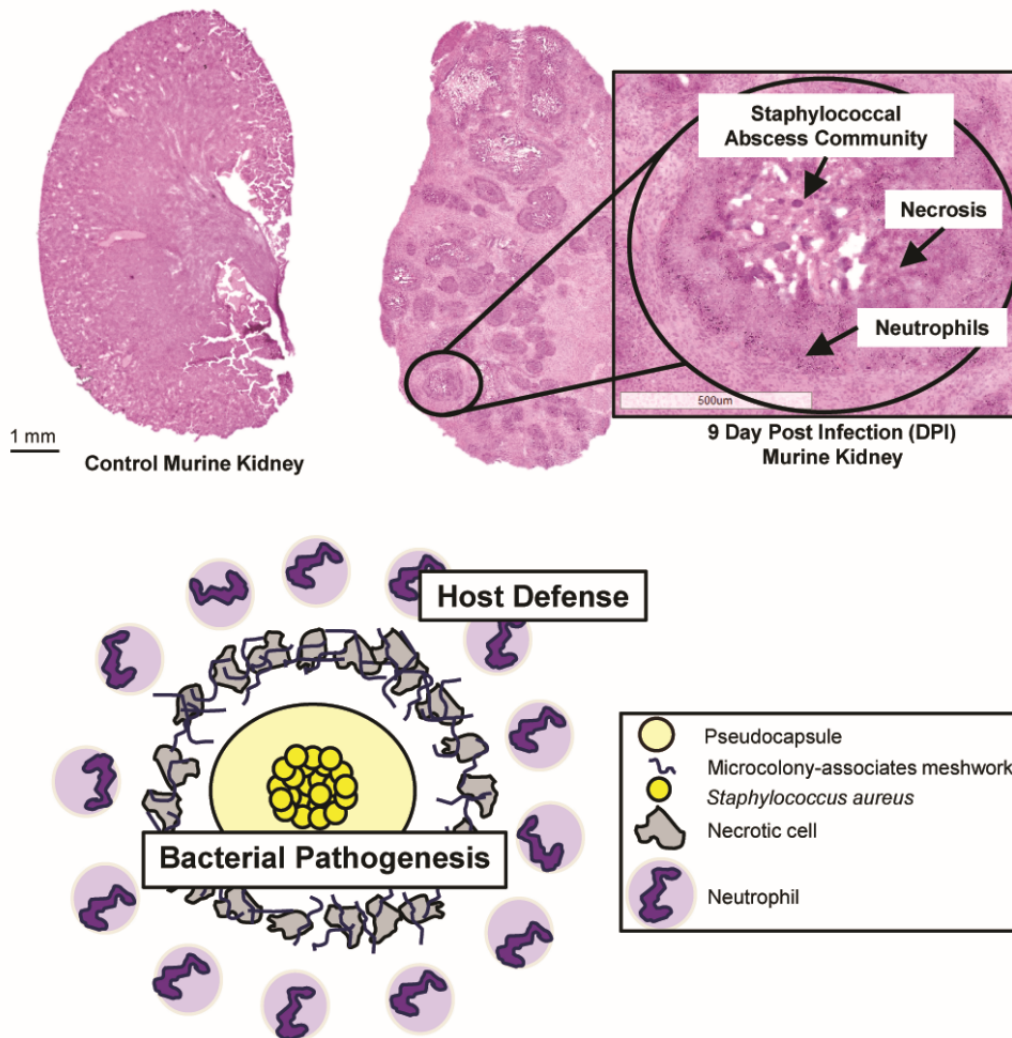


Figure 1.7: *Staphylococcus aureus* Tissue Abscess Morphology

An H&E tissue stain of a control and *S. aureus* infected mouse kidney highlight the presence of abscesses within the infected tissue. A zoom of this structure shows common components of abscesses. A graphic below shows a more specific structures of abscesses.

Due to the ability of IMS to molecularly probe complex tissue environments without the need for antigen-specific tags, this technology has been applied to a wide variety of biological and medical issues. One such area is the application to the field of infectious diseases. Characterization of the host-pathogen interface by spatially targeted molecular analysis technologies enable a

deeper understanding of bacterial pathogenesis and host defense mechanisms. IMS has been employed to investigate this interface, identifying both host and pathogen factors.^{13, 77, 87, 88}

Advances in IMS instrumentation using FT-ICR MS allow for the measurement of isotopically resolved protein species directly from tissue, Figure 1.8A and 1.8B.⁸⁷ Previous research of protein distributions at the infectious interface focused on the heterodimer calprotectin (CP) constructed by S100A8 and S100A9 subunits.^{87, 88} CP can bind manganese, zinc, calcium, and iron (Fe).⁸⁸⁻⁹⁰ By decreasing the availability of necessary metal species, metalloproteins inhibit proliferation of pathogens by processes of nutritional immunity.⁸¹ The resolving power provided by a 15 Tesla (T) FT-ICR MS resulted in the identification of post translational modifications to S100A8 and S100A9. Modified S100A8 and S100A9 species were observed to form a spatial gradient from singly to triply oxidized species as distributions approached bacterial foci, Figure 1.7D.⁸⁸ This observation can be explained by reactive oxygen species (ROS) used by a host to kill pathogens.

Application of IMS in tandem with multiple other imaging modalities such as LA-ICP IMS, BLI, magnetic resonance imaging (MRI), and blockface imaging provided 3D distributions of protein and metal abundances at 50 μm spatial resolution.¹³ Multimodal analysis revealed heterogeneous bacterial transcriptional responses and host inflammatory responses. Specifically, IMS allowed visualization of CP throughout a 3D volume of a *S. aureus* infected murine kidney, Figure 1.8F. Use of genetically modified bacteria that produce a bioluminescent response to Fe starvation allowed visualization of transcriptional response *in vivo*, Figure 1.8E. LA-ICP IMS provided elemental distributions translocated by processes of nutritional immunity, Figure 1.8F. MRI provided a scaffold for 3D reconstruction of image data file. Finally, blockface image analysis provided visual context to imaging data as well as verification of signal localizations

within tissue. A major discovery from this study is that abscesses within the same organ have heterogeneous molecular architectures despite having a homogeneous appearance by traditional microscopy. Consistent with this observation, bacterial pathogens exhibited heterogeneous responses both within and between tissue lesions. Collectively, IMS is a promising research tool for the label-free identification of tissue pathology characterized by altered protein or element abundance.

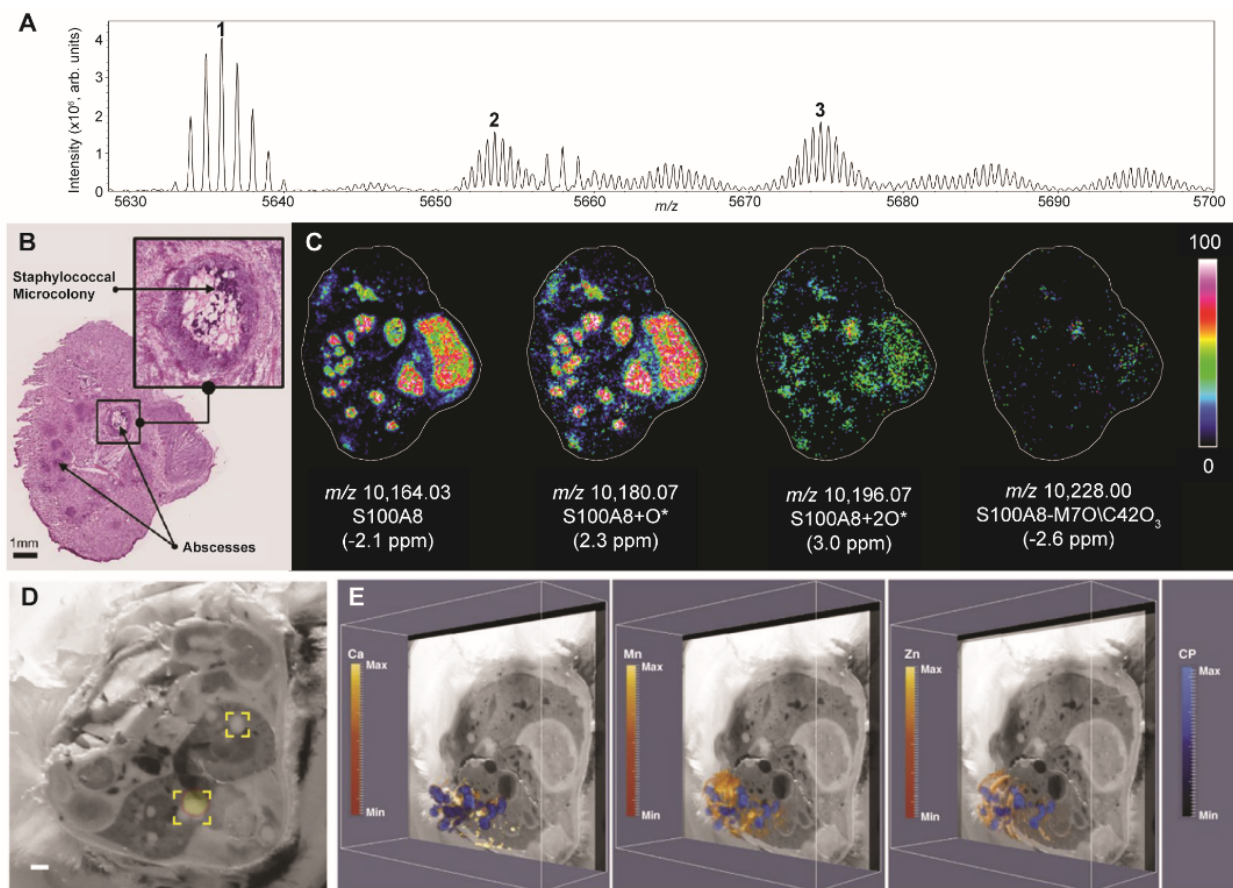


Figure 1.8: MALDI FT-ICR IMS Isotopic Resolution of Proteoforms and Elemental Context to the Host-Pathogen Interface

(A) MALDI FT-ICR IMS of intact proteins from rat brain tissue (resolving power of $\sim 40,000$ at m/z 5000) provide isotopic resolution and allow ions of different charge states and modifications to be distinguished. The ion labeled 1 is singly charged and ions labeled 2 and 3 are examples of doubly charged ions. (B) An H&E stained tissue section is annotated for *S. aureus* abscesses within a murine kidney tissue section. (C) Selected ion images of intact proteins from kidney tissue from a mouse infected with *S. aureus* collected using MALDI FT-ICR MS show advancing oxidation products localizing to the center of infectious foci. Ions were identified using mass accuracy to correlate imaging results with separate top-down proteomics experiments. (D) A blockface image of a *S. aureus* infected murine cross section overlaid with bioluminescent signal shows heterogeneous Fe starvation of bacteria. The bioluminescent signal is depicted as a yellow sphere outlined in orange. Yellow boxes on the blockface images correspond to specific abscesses. (E) The MALDI IMS imaging volume for calprotectin encompassing the infected right kidney was co-registered to the LA-ICP IMS volume for calcium, manganese, or zinc, displayed obliquely to delineate calprotectin and element distribution throughout the kidney. Heat maps depict minimum and maximum values in arbitrary units. Reprinted from *Proceedings of the NATO Advanced Study Institute in Detection, diagnosis, and health concerns of toxic chemical and biological agents*, 2019, “Matrix-assisted laser desorption/ionization imaging mass spectrometry: technology and applications” with permission from Springer Publishing Company.²

Use and Utility of Fluorescence and Autofluorescence Microscopy in Multimodal Imaging

Fluorescence microscopy relies on the principles of molecular absorption and emission of ultraviolet radiation. Occurring on nanosecond time scales, the emission wavelength of light is typically shorter than the absorption wavelength, termed the Stokes shift. Many excellent reviews exist that describe the physical principles of fluorescence in detail.^{91, 92} Various endogenous molecules within a biological sample can fluoresce after excitation, termed autofluorescence. By employing specific emission and excitation filters, high contrast morphological information can be obtained from tissue samples, termed autofluorescence microscopy (AF). Furthermore, the introduction of exogenous reporter or transgenic fluorophores can provide spatial information about specific cell types or responses *in vivo*.⁹³ Fluorescence and autofluorescence microscopy are nondestructive techniques that can be applied prior to any IMS experiment for downstream information about tissue structures and can be leveraged for accurate computational image registration and data mining approaches.^{93, 94}

Applications of Integrating Multiple 2-Dimensional Molecular Imaging Modalities

Multimodal imaging studies can incorporate a variety of acquisition technologies resulting in multiple data dimensionalities, image spatial resolutions, and data sizes. However, a common goal of image integration is to synergistically combine information derived from multiple technological sources to elucidate complex biological processes or interactions *in situ*. The key challenges in any multimodal study are image registration and data mining of the resultant datasets.

Verbeeck *et al.* recently advanced data mining strategies for multimodal data by integrating spatial molecular data with conventional models or scaffolds. In an automated approach, structural context provided by MRI and the publicly accessible Allen Mouse Brain Atlas was correlated to

IMS data.^{95, 96} Specifically, IMS-atlas integration was used in one example to perform automated anatomical interpretation to isolate differential ions in specific tissue sub-regions in normal rat brain and a Parkinson's disease rat model.⁹⁶ However, this strategy has yet to be applied to elemental imaging data.

Evaluable, accurate registration between modalities was recently accomplished by Patterson *et al.* By leveraging the nondestructive nature of (AF), tissue structures can be identified and ultimately allow for computational image registration. IMS and AF data were aligned to specific morphological information from an H&E stain within a single tissue section. IMS datasets of different spatial resolutions were correlated based on this AF workflow to isolate data from the same physical locations with a computational metric to determine pixel overlap.^{94, 97, 98} A consideration when using the AF registration workflow is the potential elemental, molecular, or morphological differences when analyzing and combining information from serial tissue sections.

In cases where common modalities and advanced image registration are not employed, effective multimodal imaging can be performed by acquiring multiple assay types from a single tissue section. Holzlechner *et al.* overcame potential differences in serial tissues sections by analyzing the molecular and elemental constituents of the same tissue section in subsequent imaging experiments. Specifically, this study achieved quantitative LA-ICP IMS measurements of platinum from individual tissue sections previously subjected to MALDI IMS. Statistical analyses isolated molecular species that correlated with platinum distributions.¹⁰ Analogous to multimodal studies of metal and chemical distributions, Svirikova *et al.* mapped elemental and lipid distributions within a single bone tissue section by utilizing the nondestructive capabilities of μ XRF imaging (μ XFI) in tandem with MALDI IMS to (Figure 1.9A).⁹⁹

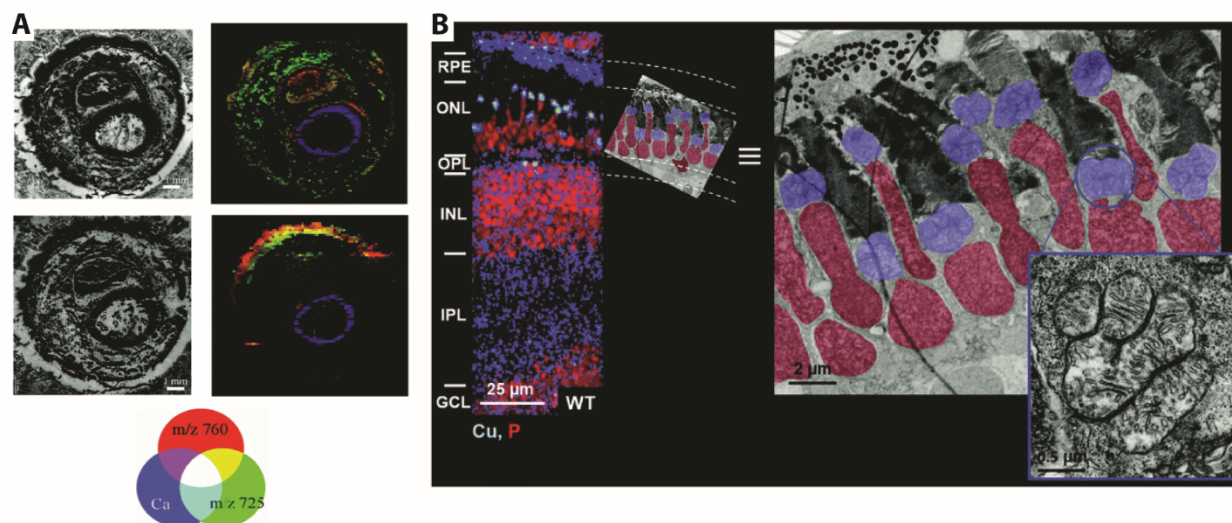


Figure 1.9: Overview of Recent Studies Employing Elemental Imaging in 2D

(A) Bright field microscopy images of sectioned bone (left) from two sample preparations (top and bottom). Images depicting the abundance of two lipids (m/z 760 in red, m/z 725 in green) as well as calcium distributions (blue) as detected by MALDI IMS and μ XFI respectively are shown on the right. Adapted from Svirkova *et al*⁹⁹ (B) NanoSIMS ion image overlay of copper (blue) and phosphorous (red) from zebrafish retina (left) and an electron micrograph of similar region (right) with false colored labels highlighting nuclei (red) and megamitochondria (blue). Inset, corresponds to one megamitochondrion and indicates co-localization of copper puncta and megamitochondria. Adapted from Ackerman *et al*¹⁰⁰ Reprinted from Current Opinion in Chemical Biology, 2020, 55, 127- 135, “Integrated molecular imaging technologies for investigation of metals in biological systems: a brief review” with permission from Elsevier.¹

Another active area of research often employing elemental imaging by XFI in combination with a variety of additional modalities is in the various sub-fields of neuroscience, as reviewed elsewhere.¹⁰¹ Within this area of neurological research, XFI has been applied to many multimodal imaging studies, often in combination with FTIR. Studies employing such experimental strategies span a variety of topics, including research into Alzheimer's disease, neurological effects of diabetes, intracerebral hemorrhage, and brain aging.¹⁰²⁻¹⁰⁵

While previously mentioned studies successfully resolved elemental distributions in tissues at or above cellular resolutions, Ackerman and colleagues combined LA-ICP IMS and nanoSIMS with confocal and electron microscopy to quantify subcellular copper accumulation in a Zebrafish

model of Menkes disease (Figure 1.9B).¹⁰⁰ This experimental setup highlights the power of combining metal imaging with other high-resolution modalities.

Beyond image registration, machine learning methods have been developed to computationally fuse image data from modalities with disparate spatial resolution and information content. This approach, termed data-driven image fusion, enables a number of predictive applications including increased effective spatial resolution, non-biological noise removal, and out-of-sample prediction.¹⁰⁶ Data-driven image fusion allows for correlation between data from high information volume imaging technologies such as IMS with more fine-textured, but lower information content imaging such as stained microscopy. As a proof-of-concept, Van de Plas *et al.* computationally combined stained microscopy with MALDI IMS to predictively increase the spatial resolution of MALDI IMS data beyond the capabilities of current instrumental platforms.¹⁰⁷ This approach is intriguing for the investigation of specific cell types in tissues and as a way to comprehensively mine molecular relationships as they relate to fine tissue structures. Building on these preliminary studies, our group has successfully employed fusion to combine high-performance MALDI FT-ICR IMS and H&E microscopy generated from renal tissue of mice systemically infected with *Staphylococcus aureus*. We show the predictive distributions of two intact protein distributions in and around individual bacterial abscesses at 15 μm spatial resolution (Figure 1.10). It is noted that to acquire the raw FT-ICR IMS data at 75 μm spatial resolution (10,000 total pixels) required \sim 9 hours. If the experiment was performed at the predicted spatial resolution of 15 μm it would have resulted in $>250,000$ pixels and would have required >9 days of continuous data acquisition. This is an example of the necessity for computational predictions where generation of the data exclusively through experimentation would be impractical or impossible. In addition to these examples from our research group, fusion has been applied in other

studies combining other modalities such as SIMS, FTIR, scanning electron microscopy, and Raman spectroscopy.¹⁰⁸⁻¹¹⁰ However, to our knowledge, fusion has yet to be applied to elemental imaging data.

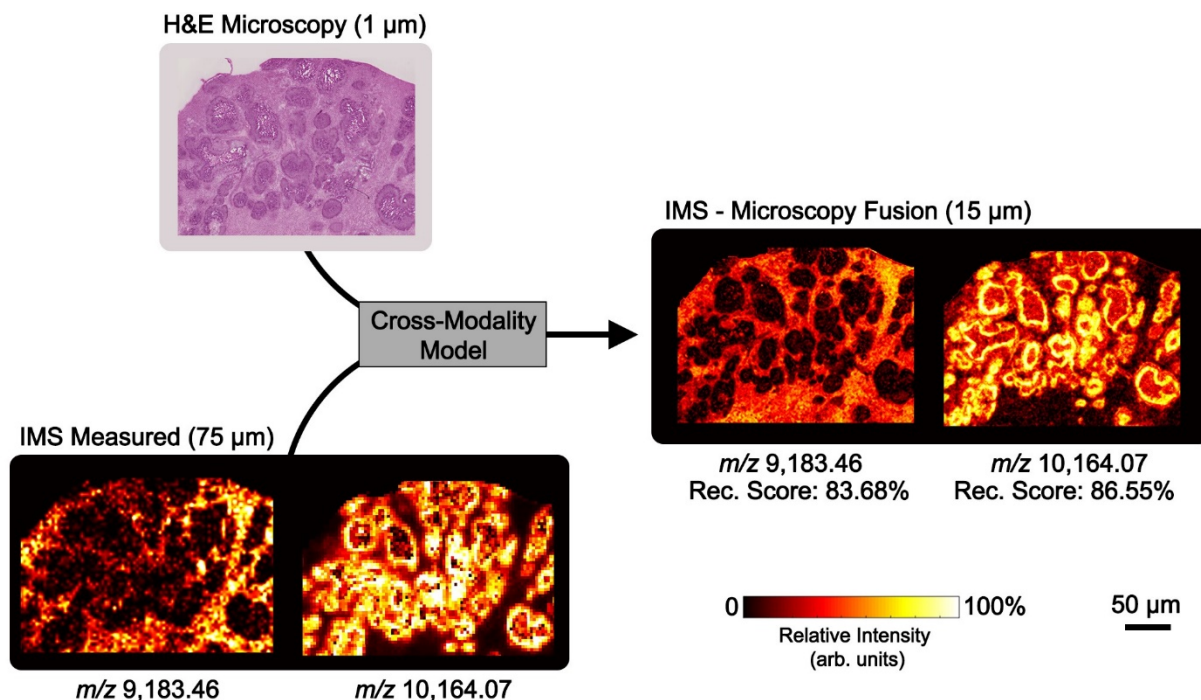


Figure 1.10: Data-Driven Image Fusion Applied to MALDI FT-ICR IMS of Intact Proteins from a *S. aureus* Infected Murine Renal Tissue Section

Multivariate linear regression is used to construct a cross modality model from H&E stained microscopy (1 μm spatial resolution) and MALDI FT-ICR IMS of intact proteins (75 μm spatial resolution, unknown protein at m/z 9,183.46, S100A8 at m/z 10,164.07) acquired from the same 7 day post *S. aureus* infected murine renal tissue section. The fused IMS-microscopy data set enables prediction of protein ion images to higher spatial resolution (15 μm spatial resolution). Statistical measures of confidence are provided for both predictions (Reconstruction Scores).¹⁰⁷ Reprinted from Current Opinion in Chemical Biology, 2020, 55, 127- 135, “Integrated molecular imaging technologies for investigation of metals in biological systems: a brief review” with permission from Elsevier.¹

Research Objectives and Summary

IMS workflows were developed, characterized, and implemented in combination with microscopy-based techniques to investigate *Staphylococcus aureus* pathogenic adaptations within infections. First, lipid observations from several MALDI matrices were compared to characterize how a specific sample preparation, including MALDI matrix, influences resultant ions. This knowledge relating MALDI matrix to lipid observations was then applied to molecularly interrogate *S. aureus* lipids within infections. Leveraging fluorescence microscopy of bacterial reporters and MALDI FT-ICR IMS, m/z values were isolated from fluorescent foci to ultimately identify and map *S. aureus* lysyl-PG lipids from a murine infection model. Next, these pathogenic lipids were visualized from a human endocarditis tissue sample. Finally, cationic antimicrobial peptides (CAMPs), hypothesized to influence *S. aureus* lysyl-PG production, were mapped across the human endocarditis tissue. Continuing this observation that a MALDI matrix will influence analyte observation, several surfaces coatings were compared to ultimately visualize *S. aureus* siderophores within tissue infections. This research was complemented by LA-ICP IMS to map elemental Fe from sites of infection and fluorescence microscopy to map *S. aureus* Fe starvation. The development and application of multimodal workflows to infectious diseases allow for critical insight to host-pathogen interactions, not accomplished by traditional molecular interrogation strategies.

CHAPTER II

UNCOVERING MATRIX EFFECTS ON LIPID ANALYSES IN MALDI IMAGING MASS SPECTROMETRY EXPERIMENTS

This chapter was adapted from the previous published Perry et al., *Journal of Mass Spectrometry*, Copyright 2019 by John Wiley & Sons, Inc.¹¹¹

Overview

The specific matrix used in MALDI IMS can influence the molecules ionized from a tissue sample. The sensitivity for distinct classes of biomolecules can vary when employing different MALDI matrices. Here, we compare the intensities of various lipid sub-classes measured by MALDI FT-ICR IMS of murine liver tissue when using 9AA, CMBT, DAN, DHA, and DHB matrices. Principal component analysis and receiver operating characteristic curve analysis revealed significant matrix effects on the relative signal intensities observed for different lipid sub-classes and adducts. Comparison of spectral profiles and quantitative assessment of the number and intensity of species from each lipid sub-class showed that each matrix produces unique lipid signals. In positive ion mode, matrix application methods played a role in the MALDI analysis for different cationic species. Comparisons of different methods for the application of DHA showed a significant increase in the intensity of sodiated and potassiated analytes when using an aerosol sprayer. In negative ion mode, lipid profiles generated using DAN were significantly different than all other matrices tested. This difference was found to be driven by modification of phosphatidylcholines during ionization that enables them to be detected in negative ion mode. These modified phosphatidylcholines are isomeric with common phosphatidylethanolamines confounding MALDI IMS analysis when using DAN. These results show an experimental basis

of MALDI analyses when analyzing lipids from tissue and allow for more informed selection of MALDI matrices when performing lipid IMS experiments.

Introduction

MALDI utilizes a small, organic chemical matrix that aids in analyte desorption and ionization.⁹ In MALDI IMS, ions are generated from discrete x,y locations (pixels) across a sample surface using laser irradiation, and a mass spectrum is recorded at each position. Ion images are visualized by plotting the relative abundance of any m/z value as a heat map over the measurement area.^{14, 112, 113} No current MALDI matrix preparation provides high sensitivity for all classes of biomolecules within a single IMS experiment. Thus, the MALDI matrix chosen for an IMS experiment will greatly influence the measured intensities of various analyte classes during analysis.⁹⁷

MALDI matrices are chosen based on their ability to provide sufficient ionization efficiency for a given analyte class (*e.g.* low molecular weight metabolites, lipids, proteins, polymers, or inorganic compounds) or sub-class.^{18, 40, 41, 114-118} Differences in observed analyte sensitivities can be attributed to the physical properties of a matrix such as molecular structure, pH, proton affinity, and peak wavelength absorbance.^{18, 40, 44-47, 119} DHB is the most widely employed and studied MALDI matrix offering sufficient sensitivities for many analyte classes in positive ion mode MS analysis.^{45, 49, 50, 120-122} 9AA is often used for the analysis of low molecular weight compounds in negative ion mode MS analysis and DAN ionizes many sub-classes of lipid species with high sensitivity in both polarities.^{18, 47} While both 9AA and DAN are considered sensitive matrices, energy transferred during the MALDI process can result in analyte modification or fragmentation complicating data interpretation.^{49, 51, 123} Volatility is also a consideration when

selecting a MALDI matrix because the matrix layer must remain stable for lengthy acquisition times (hours) to avoid signal loss during an imaging experiment. Matrix sublimation becomes a concern when using instruments with high vacuum source regions. DHA is an excellent matrix for MS analysis of multiple analyte classes, however, its high volatility limits acquisition times of MALDI TOF experiments.⁴⁰

Biological application or technological advancement of MALDI IMS for lipid analysis has been performed in numerous studies. Advancements include development of tissue washing protocols, new chemical matrices, and matrix application methods.^{30, 43, 53, 124-130} The most thorough studies to investigate MALDI matrices for IMS have focused on DAN, investigating analyte sensitivity and degradation patterns.^{18, 131} However, these studies concentrated on a single matrix or utilized instrumental platforms with limited molecular coverage, restricting the number of observed lipids.

Herein, the relative sensitivity and molecular coverage of commonly employed MALDI matrices is compared for IMS of lipids. This systematic assessment leverages high resolving power FT-ICR IMS to evaluate lipid profiles with exceptional molecular coverage and specificity. Comparisons of IMS datasets collected using various MALDI matrices elucidate trends in observed lipid sub-class and adduct formation. We note the propensity of DAN to modify phosphatidylcholine lipids during negative ion mode IMS analysis as well as differences in adduct formation in positive ion mode IMS analysis. Evaluation of the effective sensitivity and molecular coverage of lipid sub-classes will enable more informed experimental design for IMS experiments.

Results

Matrix Effects on Positive Ion Mode Lipid Analysis

Visual comparison of IMS averaged spectra show differences in spectral profiles for each matrix tested (Figure 2.1a). In the lower m/z range (m/z 300 – 550), higher intensity signals resulting from matrix clusters can be observed in the DAN averaged spectrum relative to other matrices. CMBT, uniquely, produced matrix-lipid adducts that can be observed from m/z 1,000-1,100 (fragmentation data not shown). Signals from m/z 1,500 – 1,650, observed in all cases, were determined to be lipid dimer species based on mass accuracy measurements. Although dimer signals visually appear less intense with CMBT matrix, this is an effect of scaling due to high intensity signals from m/z 1,000 – 1,100. Lipid sub-classes, compared as a percent composition of the total number of lipids for protonated, sodiated, and potassiated ion types, generally show similar profiles for the matrices tested. (Figure 2.1b – 1d). However, several trends were elucidated for each of the common cation adducts. For $[M+H]^+$ ion types (Figure 2.1b), the highest percentage of phosphatidylglycerols (purple) was detected using DHA. Additionally, DAN resulted in a higher relative percentage of glycopospholipids (light green), whereas the highest percentage of phosphatidylserines was detected using 9AA (dark purple). The highest percentage of sodiated sulfatides (dark orange) was detected using DAN, and the highest percentage of sodiated phosphatidylethanolamines (dark blue) was detected using DHA (Figure 2.1c). Finally, the relative percentage of potassiated cardiolipins (yellow) and potassiated glycerophospholipids (green) were higher for all matrices compared to protonated and sodiated ion types (Figure 2.1d). To compare sensitivity and propensity for adduct formation, the total number of lipids was compared for each ion type (Figure 2.1e). While the largest number of lipids were detected with DHA, many were

$[M+Na]^+$ ion types. Although DAN is highly sensitive it does not provide the molecular coverage of 9AA, CMBT, and DHA. These comparisons show broad differences in observed intensities when employing various matrices for IMS of lipids. However, specific trends in positive ion mode data can be further isolated using statistical tools such as principle component analysis (PCA) and receiver operating characteristic curve (ROC) analysis.

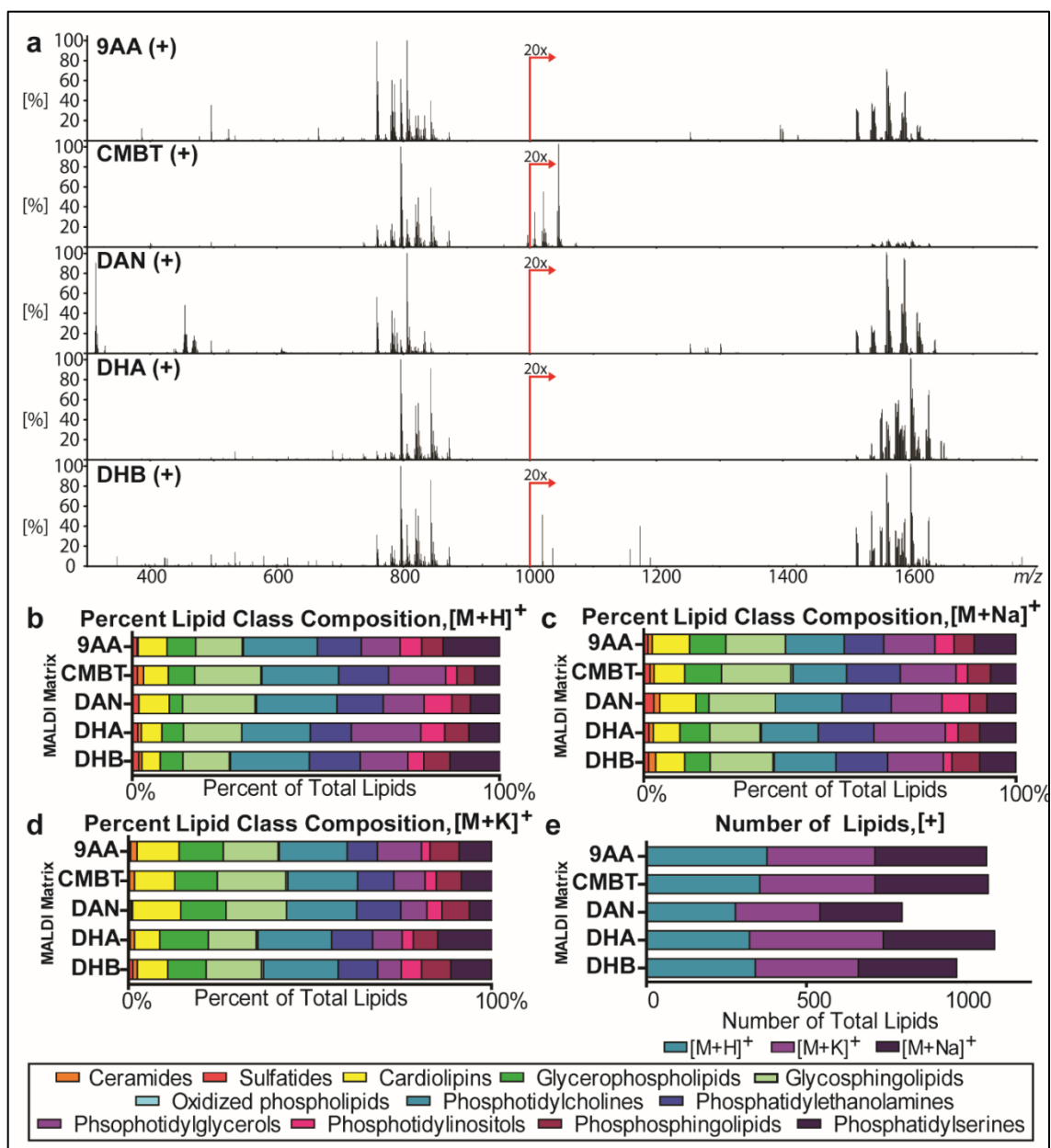


Figure 2.1: Comparisons of Positive Ion Mode Lipid Analyses Using Several MALDI Matrices

Comparisons of positive ion mode lipid analyses using several MALDI matrices reveal differences in global spectral profiles, the relative abundances of lipid sub-classes, and the lipid ion types. (a) The average spectra from the IMS analysis for 9AA, CMBT, DAN, DHA, and DHB matrices show differences in global spectral profiles. (b-d) Lipids were aggregated into the appropriate lipid sub-classes and displayed as a percentage of the total number of lipids for the $[M+H]^+$, $[M+Na]^+$, and $[M+K]^+$ ion types. (e) The total number of lipids was tabulated for each matrix and ion type to compare molecular coverage. The potential of a single lipid species forming multiple ion types was not accounted for. Reprinted from Journal of Mass Spectrometry, 2019, e4491, “Uncovering matrix effects on lipid analyses in MALDI imaging mass spectrometry experiments” with permission from John Wiley & Sons, Inc.¹¹¹

PCA of positive ion mode IMS data differentiated each of the five MALDI matrices tested (Figure 2.2). The scores plot from component 1 and component 2 account for 83.0% of the total variance of the dataset. Qualitatively, most of the differentiation between the spectral profiles of the MALDI matrices is captured in the first principal component. CMBT, DHA, and DHB positive ion mode data have the most similar spectral profiles, while data acquired using 9AA and DAN have overlapping profiles that are clearly distinguishable from the other matrices (Figure 2.2a). The loadings plot from these data highlights ions that are primary contributors of variation across datasets and can be used to further probe specific molecular differences. Figure 2.2b shows many data points corresponding to specific ions, distant from the central data cluster. Ions located outside of the 95% confidence interval were identified as predominately phosphatidylcholines. Most phosphatidylcholines to the left of the central cluster are cationized by potassium, while most phosphatidylcholines right of the central data cluster are protonated. This insight suggests that there is a large difference in the adducts formed during ionization for each MALDI matrix.

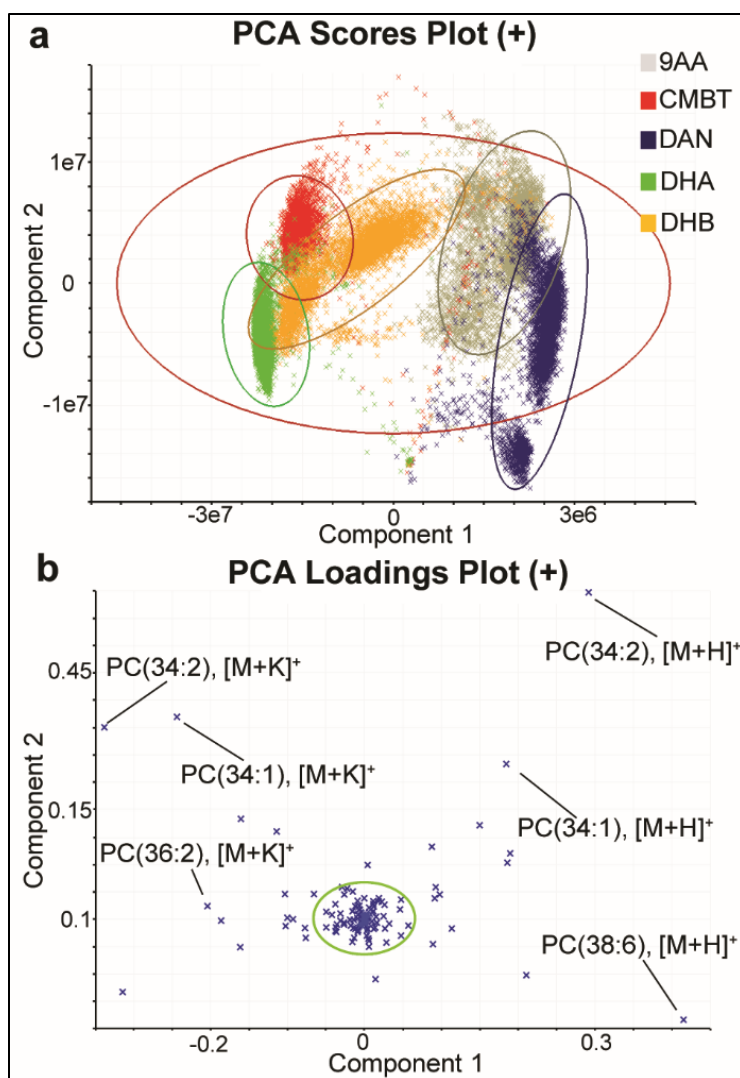


Figure 2.2: PCA of Positive Ion Mode Data for Several MALDI Matrices

PCA elucidates qualitative differences among positive ion mode data. (a) A positive ion mode PCA scores plot with a 95% confidence ellipse reveals the variance of the data. (b) A positive ion mode loadings plot with a 95% confidence ellipse highlights lipids that are separated from the central cluster, identified as protonated or potassiated phosphatidylcholines lipid species. Reprinted from Journal of Mass Spectrometry, 2019, e4491, “Uncovering matrix effects on lipid analyses in MALDI imaging mass spectrometry experiments” with permission from John Wiley & Sons, Inc.¹¹¹

Heat maps allow visualization of data from binary, supervised ROC analyses based on intensity and frequency for specific lipid sub-classes and allow for interpretation of sensitivity differences within these complex datasets (Figure 2.3). ROC analyses were structured to isolate differences in annotated lipid intensities and frequencies unique to a single MALDI matrix when

compared to other matrices. Data acquired using 9AA have higher sensitivity for protonated and sodiated phosphatidylserines relative to other matrices. CMBT, DHA and DHB show similar relative lipid sub-class sensitivities for protonated species including higher sensitivity for phosphatidylglycerols and sulfatides. CMBT, DHA and DHB matrices also displayed lower sensitivity for protonated phosphatidylserines and phosphatidylcholines, and higher sensitivity for sodiated phosphatidylcholines. Data acquired using 9AA and DAN have a higher sensitivity for protonated phosphatidylcholines. Finally, DHA resulted in higher sensitivity for potassiated signals of all lipid classes when compared to other matrices.

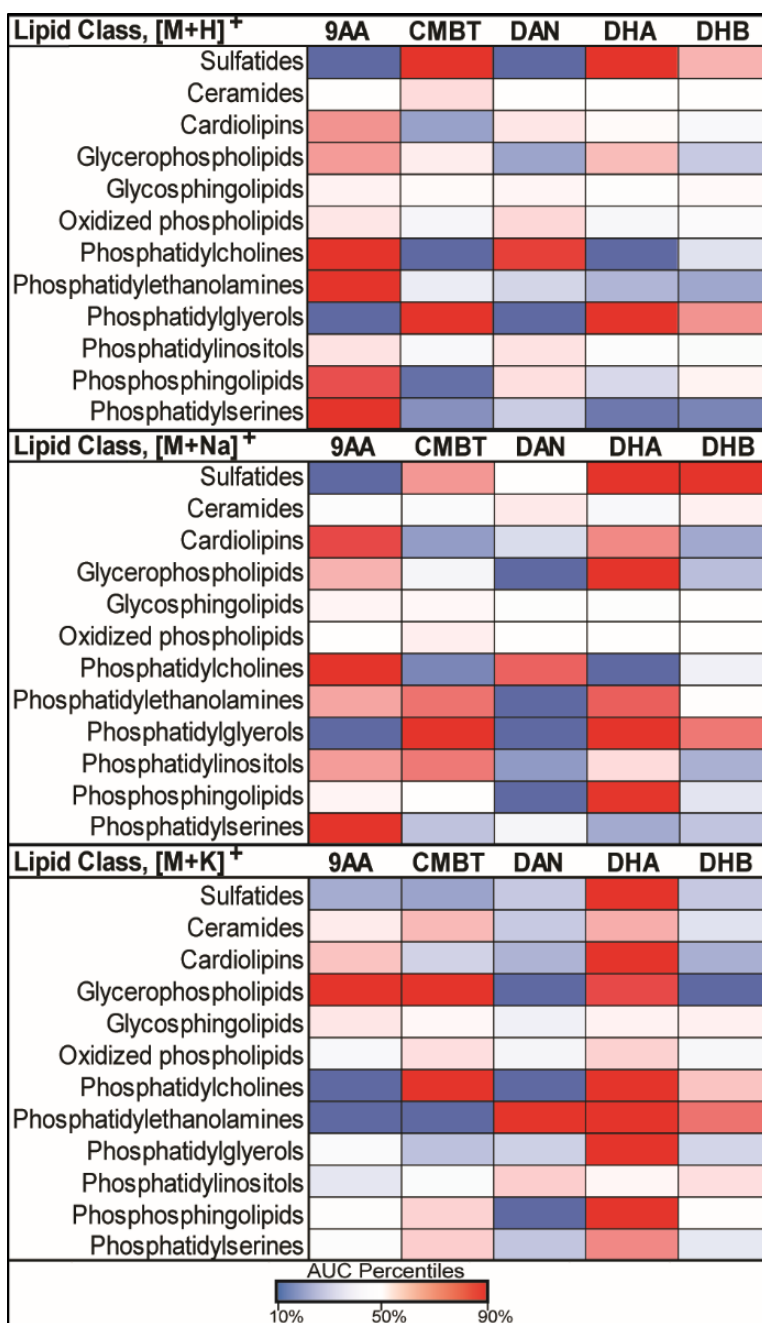


Figure 2.3: Positive Ion Mode Heat Maps to Compare Lipid Abundances

Positive ion mode heat maps for each lipid subclass allow for visualization of differences in sensitivity and are shown as a function of the ion type [M+H]⁺, [M+Na]⁺, and [M+K]⁺. Blue represents low abundance of a lipid sub-class and red represents a high abundance. Reprinted from Journal of Mass Spectrometry, 2019, e4491, “Uncovering matrix effects on lipid analyses in MALDI imaging mass spectrometry experiments” with permission from John Wiley & Sons, Inc.¹¹¹

To determine the effect of sample preparation on the ion type observed in IMS, matrix spray coating was compared to sublimation with and without a washing protocol to remove endogenous salts from the tissue. Heat maps for protonated, sodiated, and potassiated lipid annotations are shown for robotically sprayed and sublimated matrix application methods (with and without washing with 1 mM ammonium formate, Figure 2.4).^{30, 40} DHA shows a higher propensity to form potassiated and sodiated ion types when applied using a robotic aerosol sprayer, presumably due to salts being introduced during the spraying process. When matrix is applied by sublimation, potassiated and sodiated adducts are reduced. When tissues are washed with an ammonium formate buffer followed by sublimation of the matrix, protonated lipid ion types dominate the spectra. This is consistent with previous work showing matrix application and tissue washing methods influencing adduct formation due to the presence of nonvolatile salts, either endogenous to tissue or introduced by robotic aerosol sprayer matrix application.^{30, 132}

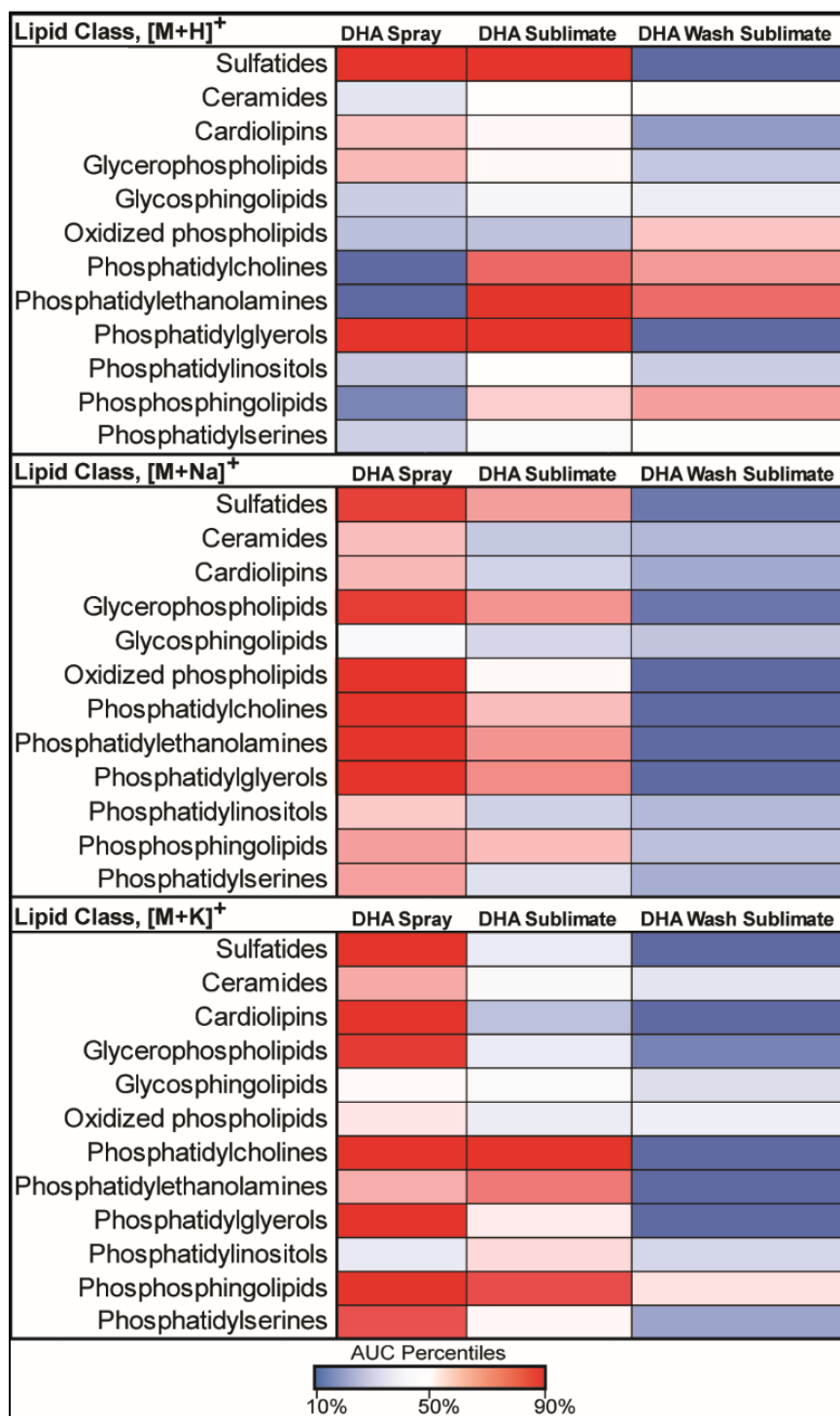


Figure 2.4: DHA Positive Ion Mode Heat Maps to Compare Matrix Application Methods
 Heat maps for each lipid subclass allow for visualization of differences in sensitivity across $[M+H]^+$, $[M+Na]^+$, and $[M+K]^+$ ion types based on the DHA matrix application method. Blue represents low abundance of a lipid sub-class and red is a high abundance. Reprinted from Journal of Mass Spectrometry, 2019, e4491, “Uncovering matrix effects on lipid analyses in MALDI imaging mass spectrometry experiments” with permission from John Wiley & Sons, Inc.¹¹¹

Lipid images of liver tissues collected as part of the statistical analyses highlighted above are depicted in Figure 2.5. Liver tissue was selected for IMS analysis due to its homogenous morphology. Three protonated phosphatidylcholines for each matrix are shown in Figure 2.5a. These ion images display higher abundances in the 9AA and DAN datasets. Three phosphatidylcholines with potassium adducts are shown in Figure 2.5b. These ion images display higher intensities in the CMBT, DHA, and DHB datasets. The images visually confirm findings from the positive ion mode area under the ROC curve (AUC) heat maps, showing differential formation of protonated, sodiated, or potassiated adducts based on the selected MALDI matrix.

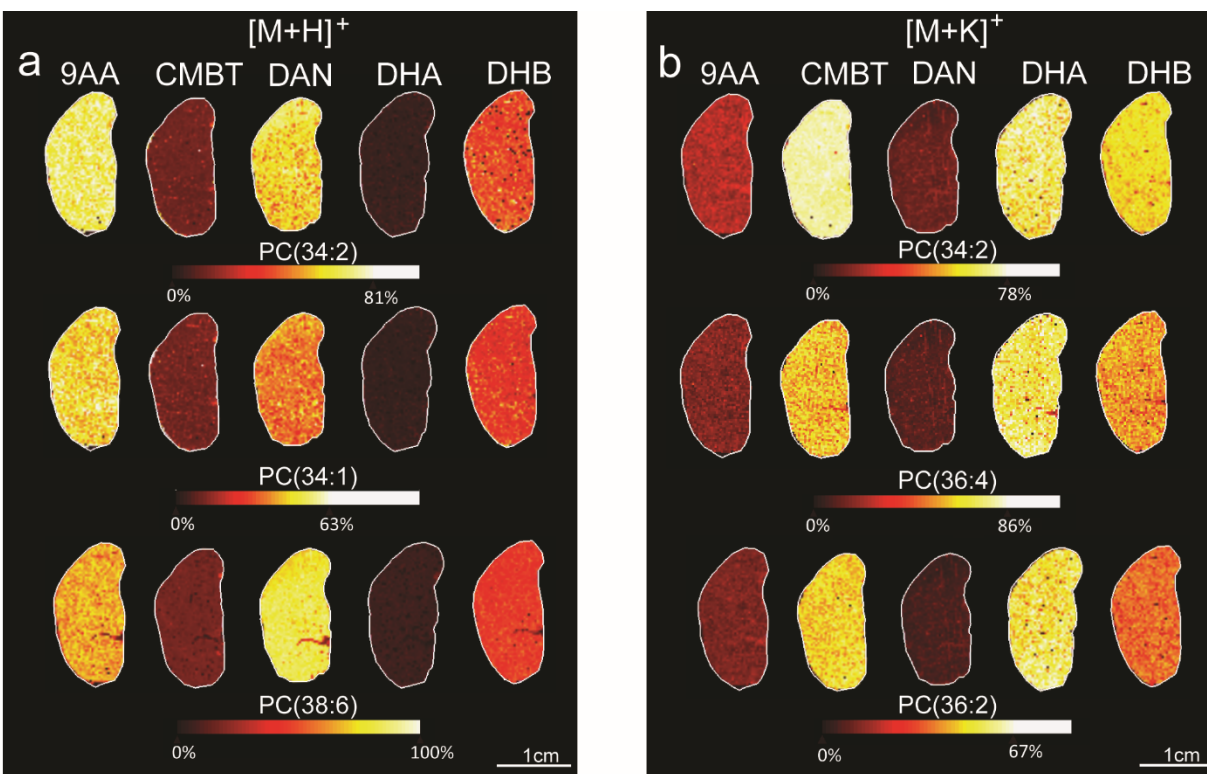


Figure 2.5: Positive Ion Mode Ion Images to Visually Compare Lipid Presence and Abundance

Individual lipid images generated from positive ion mode data. (a) Protonated phosphatidylcholine ion types were found to be more abundant within 9AA and DAN datasets compared to other matrices. (b) Potassium cationization was found to be more prevalent with CMBT, DHA, and DHB compared to 9AA and DAN. Reprinted from *Journal of Mass Spectrometry*, 2019, e4491, “Uncovering matrix effects on lipid analyses in MALDI imaging mass spectrometry experiments” with permission from John Wiley & Sons, Inc.¹¹¹

Matrix Effects on Negative Ion Mode Lipid Analysis

Negative ion mode IMS lipid analysis predominately results in deprotonated ion types.¹³³ Similar analytical strategies as those used for positive ion mode analysis were used to assess negative ion mode lipid IMS data. Visual comparison of averaged IMS spectra (Figure 2.6a) show significant differences in spectral profiles. A grouping of high intensity signals can be observed from m/z 700-800 when using DAN. Annotation of these lipids based on accurate mass measurements alone suggests that phosphatidylethanolamines are detected with greater sensitivity using DAN relative to other MALDI matrices. Additionally, the propensity of each matrix to

produce chemical noise (*i.e.* matrix clusters) in the low m/z range (m/z values < 500) varies dramatically. For example, matrix-related peaks are far more intense than lipid signals when using DHB in negative ion mode. The number of lipid annotations from each sub-class was compared as a percentage of the total number of annotated lipid species for deprotonated ion types (Figure 2.6b). DHB produced the fewest number of total annotated lipids (Figure 2.6c) predominately comprised of cardiolipins (yellow), glycosphingolipids (green), phosphatidylinositols (pink), and phosphatidylserines (dark purple). Similar species were observed for all other matrices tested. However, DAN showed a significant increase in the number of annotated phosphatidylethanolamines relative to the other lipid sub-classes. Overall, DAN and 9AA produced the largest number of deprotonated lipid ions detected in negative ion mode. This increased efficiency in negative ion mode by 9AA and DAN is attributed to the gas phase basicity or proton affinity inherent to the matrices. To further dissect trends within negative ion mode data, PCA and ROC analysis were employed.

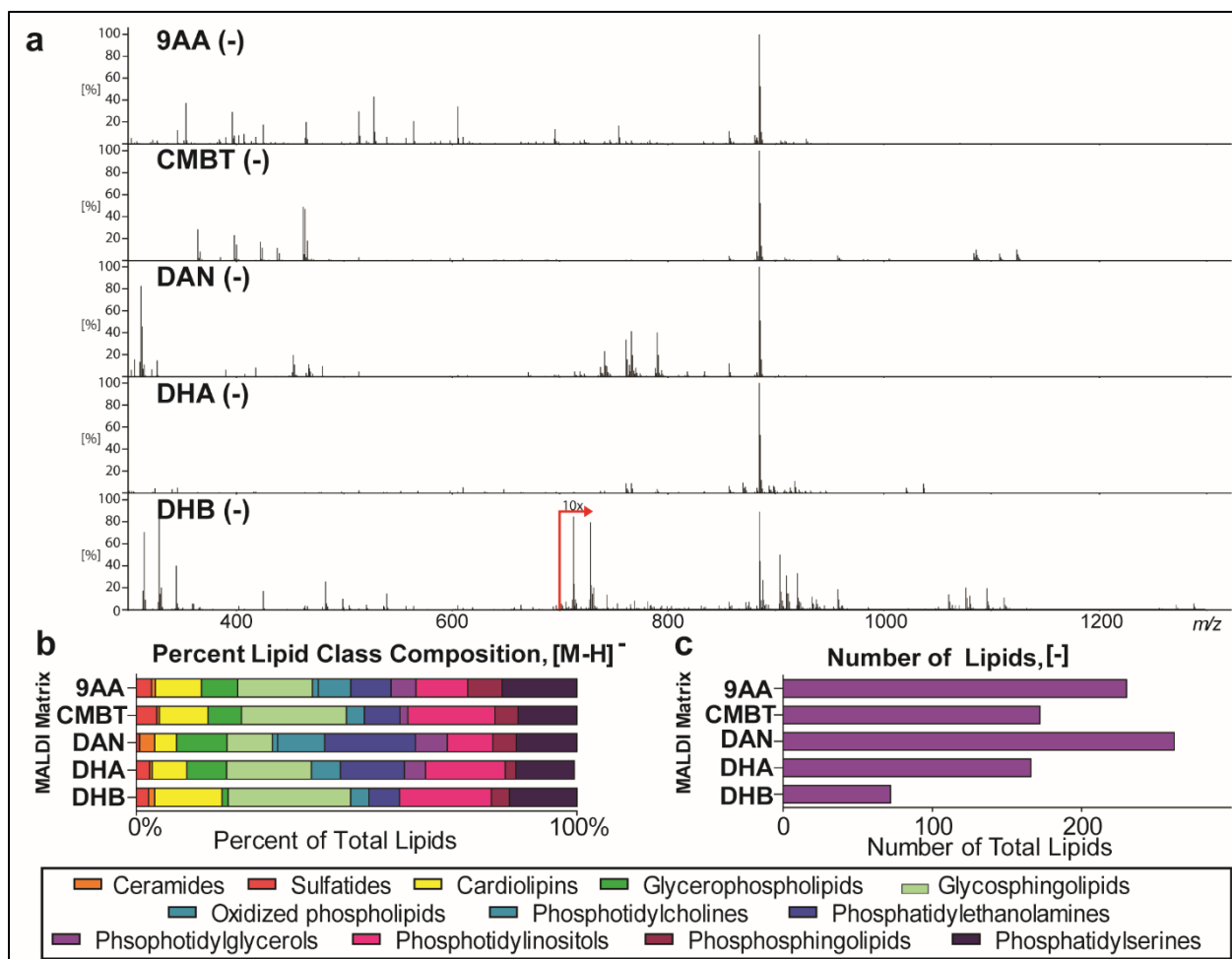


Figure 2.6: Comparisons of Negative Ion Mode Lipid Analyses Using Several MALDI Matrices

Comparisons of negative ion mode lipid analyses using several MALDI matrices reveal differences in global spectral profiles and the relative abundances of lipid sub-classes. (a) Averaged spectra from the IMS analyses for 9AA, CMBT, DAN, DHA, and DHB matrices show differences global spectral profiles. (b) Lipids were aggregated into the appropriate sub-classes and displayed as a percentage of the total number of identified lipids. (c) The total number of lipids was tabulated for each matrix to compare molecular coverage. Reprinted from Journal of Mass Spectrometry, 2019, e4491, “Uncovering matrix effects on lipid analyses in MALDI imaging mass spectrometry experiments” with permission from John Wiley & Sons, Inc.¹¹¹

PCA of the negative ion mode data provides a global view of the molecular variance between the MALDI matrices. The scores plot for principal components 1 and 2, accounting for 65.2% of the total variance of the dataset, shows that DHB and DAN datasets lie partially outside of the 95% confidence interval and distant from data acquired using 9AA, CMBT, and DHA

(Figure 2.7a). The negative ion mode loadings plot (Figure 2.7b) separates the ions into three areas outside of the 95% confidence interval ellipse. In addition to matrix clusters, there are many annotated phosphatidylethanolamines distant from the 95% confidence interval ellipse suggesting these ions play a large role in the observed variance between the examined matrices. This observation was confirmed when analyzing the heat maps for specific lipid sub-classes (Figure 2.8). A high AUC value can be observed for phosphatidylethanolamines within the DAN matrix dataset compared to other negative ion mode data acquired using other matrices.

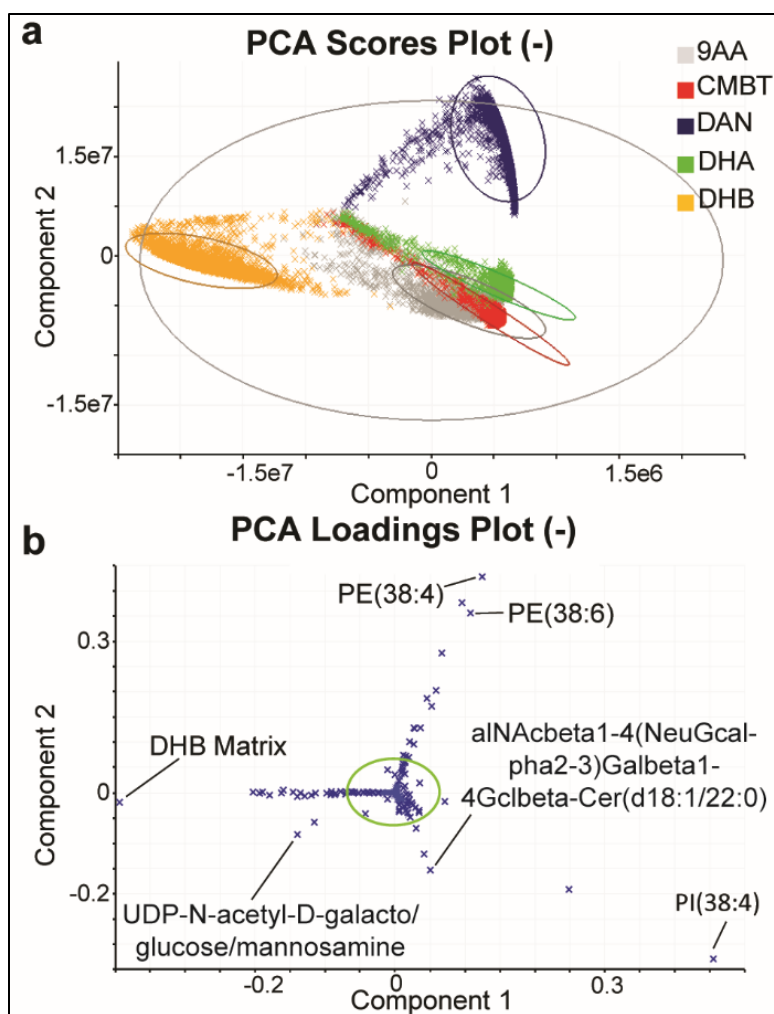


Figure 2.7: PCA of Negative Ion Mode Data for Several MALDI Matrices

PCA elucidate differences among negative ion mode data. (a) A negative ion mode PCA scores plot with a 95th confidence ellipse reveals the variance of the data. (b) A negative ion mode loadings plot with a 95th confidence ellipse highlights lipids that are separated from the central data cluster. Reprinted from Journal of Mass Spectrometry, 2019, e4491, “Uncovering matrix effects on lipid analyses in MALDI imaging mass spectrometry experiments” with permission from John Wiley & Sons, Inc.¹¹¹

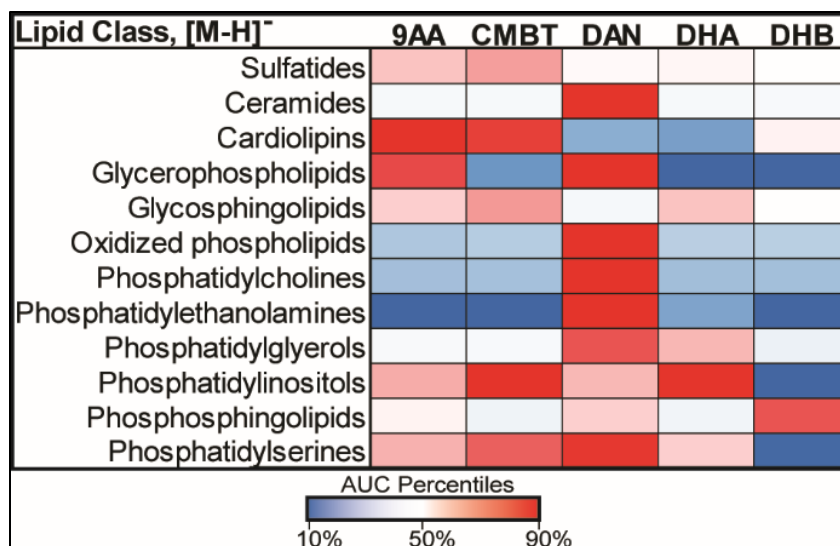


Figure 2.8: Negative Ion Mode Heat Maps to Compare Lipid Abundances

Negative ion mode heat maps for each lipid subclass allow for visualization of differences in sensitivity. Blue represents low abundance of a lipid sub-class and red represents a high abundance. Reprinted from Journal of Mass Spectrometry, 2019, e4491, “Uncovering matrix effects on lipid analyses in MALDI imaging mass spectrometry experiments” with permission from John Wiley & Sons, Inc.¹¹¹

A significant driver of this apparent sensitivity for phosphatidylethanolamines is due to lipid modifications induced by DAN during the desorption/ionization process.⁴⁹ Typically, phosphatidylcholines are not observed in negative mode analysis due to the fixed positive charge on the choline head group. However, when performing negative ion mode MALDI MS analysis of lipids using DAN, a methyl group is lost from the head group of phosphatidylcholines. This loss enables efficient ionization in negative ion mode, Figure 2.9. It is hypothesized that an amide group from the DAN matrix molecule interacts with a choline head group during the MALDI process, resulting in the creation of a 2-methyl amino head group (2MeN). The *m/z* values corresponding to phosphatidylcholines modified in this way are isomeric with phosphatidylethanolamines comprised of two additional carbons in the fatty acyl chains. These modified lipids are often misidentified and introduce experimental bias when employing DAN as a MALDI matrix to analyze complex lipid mixtures in negative ion mode.

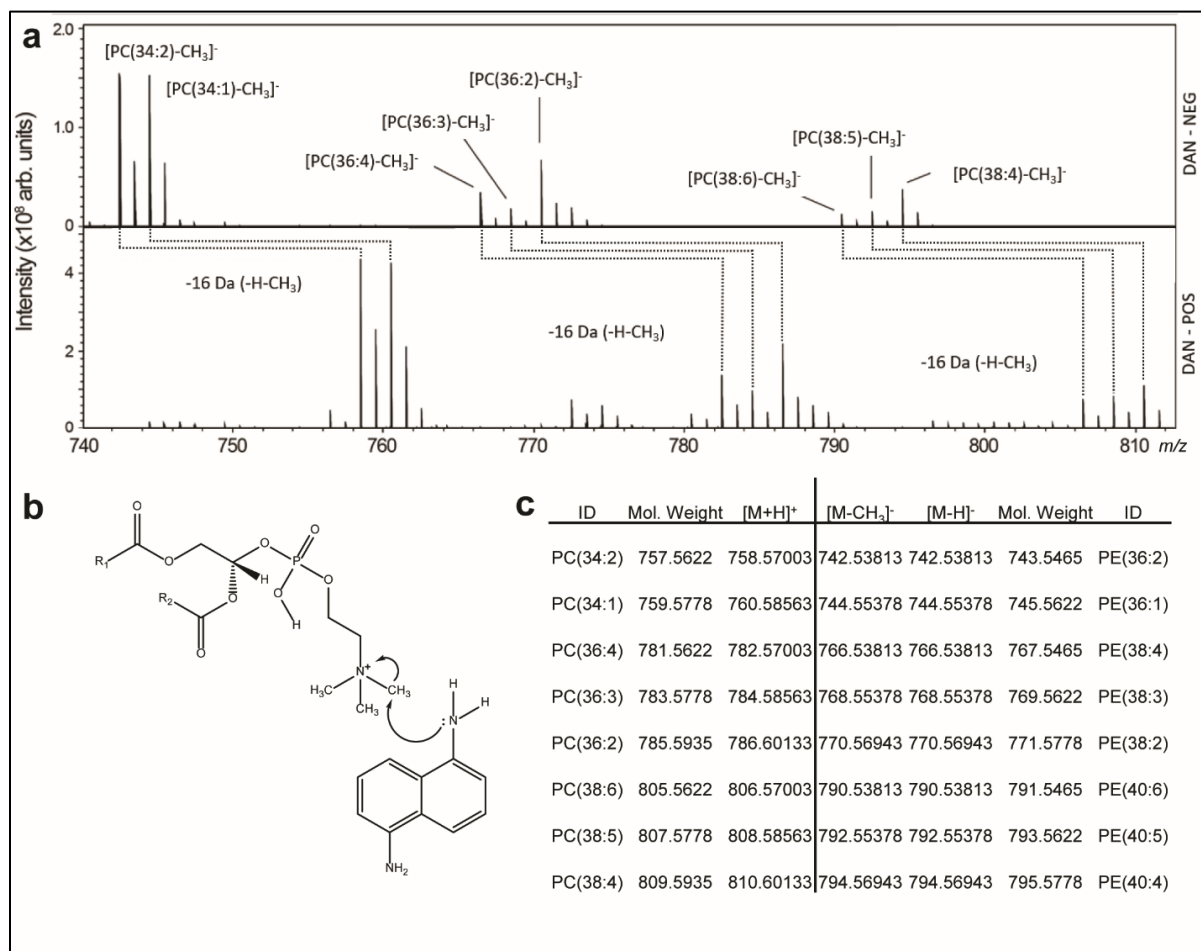


Figure 2.9: DAN Matrix Results in Modifications to Phosphatidylcholine Lipids during Negative Ion Mode Analysis

Phosphatidylcholine lipid standards were analyzed in both positive and negative ionization mode using hand spotted DAN MALDI matrix. **a)** Observation of a 16 Dalton shift between analysis of phosphatidylcholines in positive and negative ionization modes. **b)** A proposed mechanism shows the loss of a methyl from the choline head group of the phosphatidylcholine lipid species induced by DAN matrix. **(c)** m/z values from the DAN matrix effect share an accurate mass assignment with phosphatidylethanolamine lipid species. Reprinted from Journal of Mass Spectrometry, 2019, e4491, “Uncovering matrix effects on lipid analyses in MALDI imaging mass spectrometry experiments” with permission from John Wiley & Sons, Inc.¹¹¹

Ion images generated from signals highlighted by negative ion mode statistical analyses are shown in Figure 2.10. Ion images shown in Figure 2.10a correspond to molecular species less abundant in DAN data matrix. Alternatively, Figure 2.10b shows ion images for a

phosphatidylinositol, PI(38:4), detected using all matrices and two examples of phosphatidylcholines that have been modified during MALDI with DAN (2MeN-PE(36:4) and 2MeN-PE(36:6)).

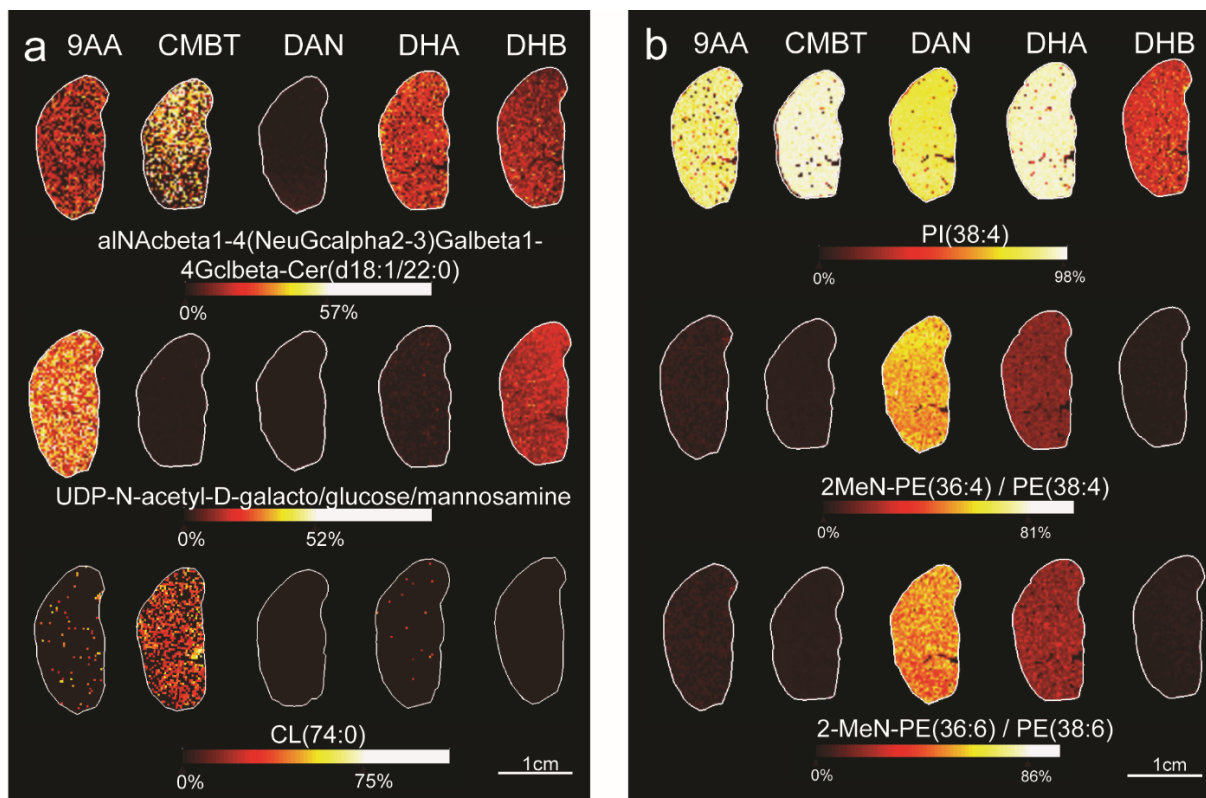


Figure 2.10: Negative Ion Mode Ion Images to Visually Compare Lipid Presence and Abundance

Individual lipid images generated from negative mode data provide visual context to trends. (a) Many lipid sub-classes were found to be less abundant with DAN compared to the other four matrices. (b) However, multiple phosphatidylethanolamine and phosphatidylinositol lipids were found to be more abundant with DAN compared to the other four matrices. Reprinted from Journal of Mass Spectrometry, 2019, e4491, “Uncovering matrix effects on lipid analyses in MALDI imaging mass spectrometry experiments” with permission from John Wiley & Sons, Inc.¹¹¹

Discussion

The sensitivity of commonly employed MALDI matrices for the analysis of lipids was compared using IMS. A global view of similarities and differences was achieved through both qualitative and quantitative approaches. Visual comparison of spectral data offered insight into the most abundant ions for each matrix (lipids, matrix clusters, or matrix-lipid adducts). The total number of lipids detected and differences between the relative number of species associated with each lipid sub-class were compared. PCA and ROC analyses enabled examination of intensity-related trends within the data. These analyses uncovered dissimilarity in the relative sensitivity for lipid sub-classes and propensity to generate sodiated and potassiated lipid cations. In negative ion mode, DAN produced lipid profiles that were significantly different than the other matrices tested. This was found to result from modification of the head group of phosphatidylcholines during desorption/ionization. An assessment of common lipid matrices uncovered chemical phenomena attributed to the method of sample preparation, adduct formation, or analyte modification that should be considered when performing MALDI IMS of lipids. The depth of analysis provided by this study allowed for insight into data trends that can indicate potential experimental biases. Furthermore, the data analysis workflow highlighted here can serve as a general strategy for efficiently processing any IMS experiment where it is helpful to identify trends in global lipid measurements.

Methods

Materials and Sample Preparations

2,5-dihydroxyacetophenone (DHA, 97%), 1,5-diaminonaphthalene (DAN, 97%), 5-chloro-2-mercaptobenzothiazole (CMBT, 90%), 2,5-dihydroxybenzoic acid (DHB, 98%), ammonium formate, hematoxylin, and eosin were purchased from Sigma Aldrich (St. Louis, MO, USA). Matrices were purified by recrystallization. 9-aminoacridine free base (9AA) was purchased from Santa Cruz Biochem (Dallas, TX, USA). Indium tin oxide (ITO) coated slides were purchased from Delta Technologies, Limited (Loveland, CO). All solvents (methanol, ethanol, acetonitrile, trifluoroacetic acid, xylenes, and acetone) and optimal cutting temperature compound were purchased from Fisher Scientific (Kalamazoo, MI, USA).

Fresh frozen mouse liver tissue (n=1 animal) was serially sectioned at 12 μm thickness using a Leica CM3050s cryostat (Leica Biosystems, Buffalo Grove, IL, USA) and thaw mounted on ITO coated glass slides (Delta Technologies, Loveland, CO, USA). Sections were stored at -80°C until thawed under vacuum. MALDI matrix was primarily applied by a robotic aerosol sprayer (TM Sprayer, HTX Technologies, Chapel Hill, NC, USA) using optimized conditions: 9AA in 90% methanol: 10% ddH₂O at 85°C, CMBT in 90% acetone: 10% ddH₂O at 30°C, DAN in 90% acetonitrile: 10% ddH₂O at 85°C, DHA in 90% acetonitrile: 9.9% ddH₂O: 0.1% trifluoroacetic acid at 85°C, and DHB in 70% methanol: 30% ddH₂O at 85°C. Surface densities of sprayed matrices are as follows: 9AA at 3.1 $\mu\text{g}/\text{mm}^2$, CMBT at 18.0 $\mu\text{g}/\text{mm}^2$, DAN at 3.6 $\mu\text{g}/\text{mm}^2$, DHA at 3.1 $\mu\text{g}/\text{mm}^2$, and DHB at 1.3 $\mu\text{g}/\text{mm}^2$. More information on matrix application by robotic aerosol sprayer can be found in Table 2.1. For matrix application comparisons, matrix was sublimed onto tissue sections using a custom-built sublimation apparatus [36]. Sublimation was performed using approximately 300 mg of DAN at 130°C and 25 mTorr vacuum for a final coating density of 2.0

$\mu\text{g}/\text{mm}^2$ and approximately 300 mg of DHA at 110°C and 25 mTorr vacuum for a final coating density of 2.0 $\mu\text{g}/\text{mm}^2$. Surface density of sublimated matrix was calculated by weight differential. Post-imaging, sections underwent a methanol wash to remove matrix followed by hematoxylin and eosin (Fisher Scientific, Kalamazoo, MI, USA) staining. Stained sections were scanned for visualization using a Leica SCN 400 optical slide scanner (Leica Microsystems GmbH, Wetzlar, Germany) at 20X magnification.

Matrix	Solvent Composition	Temperature (°C)	Passes	Concentration (mg/mL)	Solvent Flow Rate (mL/min)	Nozzle Velocity (mm/min)	Track Spacing (mm)	Surface Density* ($\mu\text{g}/\text{mm}^2$)
9AA	90% methanol: 10% ddH ₂ O	85	8	5	0.11	700	2	3.1
CMBT	90% acetone: 10% ddH ₂ O	30	4	15	0.10	1100	1.5	18.0
DAN	90% acetonitrile: 10% ddH ₂ O	85	4	10	0.15	1200	1.5	3.6
DHA	90% acetonitrile: 9.9% ddH ₂ O: 0.1% TFA	85	4	15	0.1	1100	2	3.1
DHB	70% methanol: 30% ddH ₂ O	85	12	40	0.9	1200	2	1.3

Table 2.1: MALDI Matrix Spray Application Parameters

Surface densities are based on theoretical calculations from the following formula:

$$W_{\text{surface}} = \frac{\text{NP} \times \text{Cm} \times \text{FRm}}{\text{V} \times \text{TS}}$$

W_{surface} is the weight of the matrix applied to the surface in mg/mm^2 , NP is the number of passes, Cm is the concentration of the matrix, FRm is the matrix solution flow rate, V is the velocity of the nozzle, and TS is the track spacing of the nozzle. Reprinted from Journal of Mass Spectrometry, 2019, e4491, “Uncovering matrix effects on lipid analyses in MALDI imaging mass spectrometry experiments” with permission from John Wiley & Sons, Inc.¹¹¹

Imaging Mass Spectrometry

All experiments were performed using a 15T FT-ICR mass spectrometer (MS) (solarix, Bruker Daltonics, Billerica, MA, USA) equipped with an Apollo II dual MALDI/ESI source and an infinity cell (Bruker Daltonics, Billerica, MA, USA). The MALDI source employs a smartbeam II 2 kHz, frequency tripled Nd:YAG (355 nm) laser. Molecular images were acquired with a pitch of 300 μm in both the x and y directions using a $\sim 50 \mu\text{m}$ laser beam size (250 to 1500 laser shots).

Laser fluence was adjusted for each sample to achieve optimal analyte signals. IMS data were acquired in both polarities from m/z 300 - 2000 with a resolving power ($m/\Delta m$) of $\sim 330,000$ at m/z 400. An x,y pitch offset of 150 μm allowed IMS data acquisition of both polarities from each prepared tissue sample. The time domain file size was set to 2M (free induction decay: 1.15 s). The ion optics were tuned to maximize transmission at the defined m/z range including the funnel radio frequency amplitude (220 peak-to-peak voltage (V_{pp})), source octopole (5 MHz, 310-360 V_{pp}), collision cell (collision cell voltage: +/- 2-3 V, cell: 2 MHz, 800-1000 V_{pp}), time-of-flight delay (0.7- 0.8 ms), transfer optics (4 MHz, 380 V_{pp}), and quadrupole (Q1 mass: m/z 550-700) for each matrix used. In-source collision-induced dissociation was introduced when necessary to reduce matrix clusters. The source DC optics were also tuned to maximize signal (capillary exit +/- 260 V, deflector plate: +/- 200 V, plate offset: +/- 80 V, funnel 1: +/- 110-180 V, skimmer 1: +/- 15-35 V) as well as the ICR cell parameters (transfer exit lens: +/- 15 V, analyzer entrance: +/- 1.5 V, side kick: 0 V, side kick offset: +/- 6-9 V, and front and back trap plates: +/- 1.0-1.5 V). Ion detection was performed using a sweep excitation power of 18%. Data were calibrated externally using red phosphorous clusters prior to analysis and calibrated internally post-acquisition in FTMS Processing software (Bruker Daltonics, Billerica, MA, USA) using known lipid species as lock mass assignments. Data were acquired in triplicate for each MALDI matrix. H&E stained bright field images of the tissue sections were overlaid with IMS data and imported into SCiLS Lab software (version 2016b, SCiLS GmbH, Bruker Daltonics) for visualization and analysis.

Data Analysis

Data from lipid measurements were analyzed using SCiLS Lab 2016b (Bruker Daltonics, Billerica, MA, USA) (Figure 2.11). Unsupervised analyses consisted of spatial segmentations and PCA. Bisecting k-means spatial segmentation was applied to all acquired data to identify off-tissue spectra containing only matrix signal in order to remove them from consideration for analysis. Following segmentation, positive and negative ion mode datasets were separately subjected to PCA with three components for multivariate comparison. For supervised analyses, peak filter lists were created from m/z values corresponding to lipid species derived from LIPID MAPS database (The LIPID MAPS Lipidomics Gateway, <http://www.lipidmaps.org/>) and imported into SCiLS Lab software. Peak interval windows were created from values $\pm 0.009\%$ (~ 18 ppm) of each m/z value for $[M+H]^+$, $[M+Na]^+$, $[M+K]^+$, and $[M-H]^-$ potential ion types. Percentage-based intervals appropriately scale increasing m/z values with decreasing instrumental mass resolution. Peak filter lists allowed rapid molecular annotation of any intensity value (filtered to signal-to-noise ratio > 3) present within an interval. Although the wider mass interval windows can provide false positives for chemical annotation, the high resolving power ($> 300,000$ at m/z 750) and recalibrated mass accuracy (< 3 ppm) of the FT-ICR MS data limit these occurrences. However, it is noted that this approach does not account for isomeric species. All molecular identifications are tentative and based on accurate mass measurements. ROC analyses of the annotated intensities from the LIPIDMAPS interval list were performed by comparing data replicates ($n=3$ analyses per MALDI matrix) from one matrix in a single class to replicates from all other experimental groups. Structuring the ROC analyses in this manner isolated differences in lipid intensities and frequencies unique to a single MALDI matrix when compared to other matrices. AUC values for each interval were exported for the generation of heat maps using the open source *R* environment

or Microsoft Excel. AUC values measure the discrimination quality of a single signal between two distributions (sets of matrix associated IMS pixels in this instance). A value of 1.0 or 0 would indicate perfect discrimination between two classes. Color gradients were applied to AUC values within each heat map. These AUC color gradients allow visualization of the corresponding frequency and abundance of a variety of lipid species from any experimental condition. In heat maps displaying only lipid sub-class rather than specific lipid species, AUC values were averaged for all lipid species in a class and color gradients were assigned based on percentiles. Ion images were generated for specific m/z values highlighted by statistical analyses to visually confirm findings. Ion images provided visual context of the trends identified by the analyses.

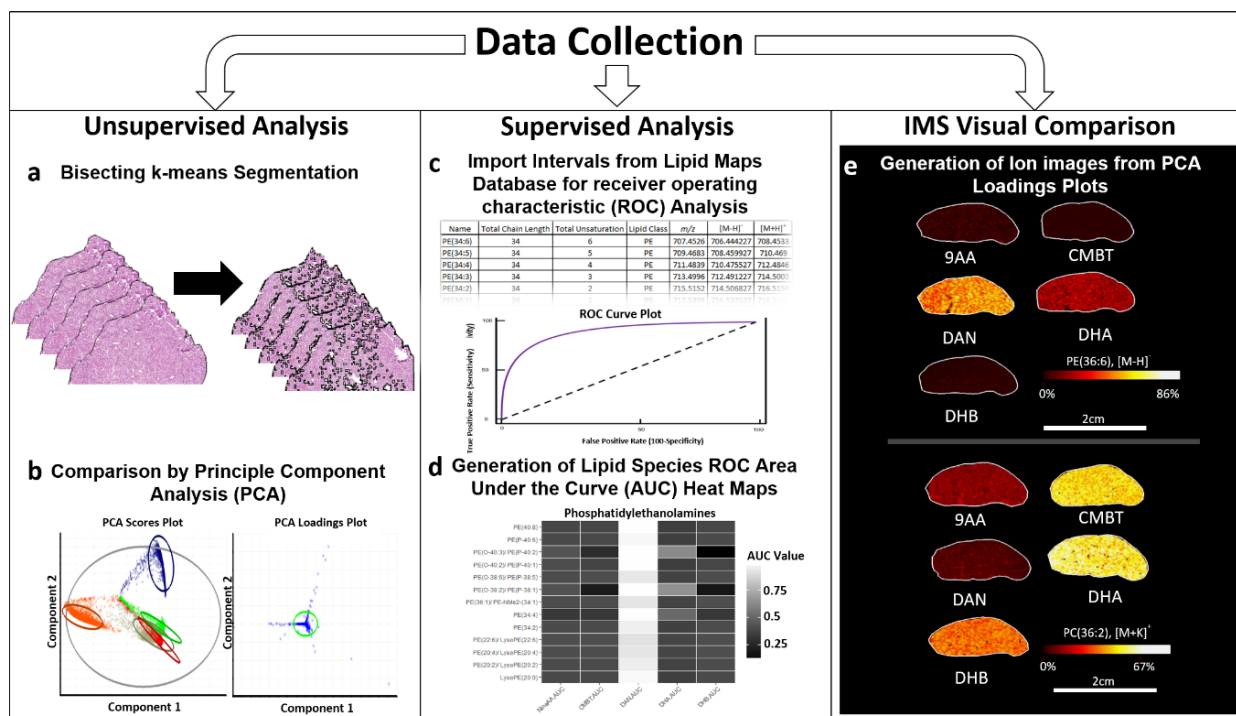


Figure 2.11: Bioinformatics Workflow to Compare the Lipid Sensitivity and Specificity of Several MALDI Matrices

Several bioinformatics strategies were used to globally visualize the lipid sensitivity and specificity of common MALDI lipid matrices post data collection. (a) For unsupervised analyses, IMS datasets were segmented using bisecting k-means to remove background matrix noise and ensure comparison of similar areas of tissue. (b) Comparisons of variance among experimental conditions were conducted by PCAs. (c) For supervised analyses, ROC analyses were conducted using peak intervals generated from LIPID MAPS database. (d) The AUC from the analysis of each ion was used as a metric to judge discrimination to an experimental group. Intervals corresponding to lipid species were visualized by AUC value heat maps sorted by lipid class, acyl chain lengths and unsaturation (e) Ion images from the m/z values stated to change in both the supervised and unsupervised analyses were consulted to visualize the changes in signal intensity across experimental sample conditions. Reprinted from Journal of Mass Spectrometry, 2019, e4491, “Uncovering matrix effects on lipid analyses in MALDI imaging mass spectrometry experiments” with permission from John Wiley & Sons, Inc.¹¹¹

CHAPTER III

VISUALIZATION OF *STAPHYLOCOCCUS AUREUS* PATHOGENIC MEMBRANE MODIFICATION WITHIN THE INFECTION ENVIRONMENT BY A MULTIMODAL IMAGING MASS SPECTROMETRY APPROACH

This chapter was adapted from an article planned for submission in 2020

Overview

Bacterial pathogens have evolved virulence factors to colonize, replicate, and disseminate within the vertebrate host. Multimodal imaging approaches allow for the visualization of host-pathogen interactions at the molecular level. Here we image modifications to the *Staphylococcus aureus* envelope within infected murine and human tissue. Data mining strategies leveraging multimodal data-driven fusion of fluorescent bacterial reporters and MALDI FT-ICR IMS isolated *S. aureus* lysyl-phosphatidylglycerol lipids, localizing to select bacterial communities within infected tissue. Lysyl-phosphatidylglycerol lipids are associated with increased pathogenicity during vertebrate colonization and provide protection to *S. aureus* against the innate immune system. The presence of distinct lysyl-phosphatidylglycerol lipid distributions within both murine and human infections suggests a heterogeneous microbial response to host defenses.

Introduction

The increased incidence of antimicrobial-resistance among bacterial pathogens has emphasized the need to discover critical pathogenic adaptations that can be targeted to develop alternative therapeutics.¹³⁴ *Staphylococcus aureus* is an increasingly antibiotic resistant human pathogen, capable of causing a variety of life-threatening illnesses that range from soft tissue

infections to serious systemic conditions.⁷⁵ Antimicrobials to combat bacterial infections commonly function by disrupting critical microbial processes such as envelope biogenesis and stability.¹³⁵ Frequently used to combat gram-positive bacterial infections, cationic compounds such as daptomycin, a last resort antibiotic, and host generated CAMPs bind or insert into bacterial membranes to compromise structural integrity.¹³⁶ Aminoacylation of anionic phosphatidylglycerol membrane lipids is a common strategy employed by bacterial pathogens to reduce electrostatic interactions and evade cationic compounds.¹³⁷ *S. aureus* is known to modify PG membrane lipids with lysine residues (lysyl-PG) through multiple peptide resistance factor (MprF), providing resistance to cationic compounds.⁸⁰

Lesions within soft tissue known as abscesses are a hallmark of *S. aureus* infection. Abscess morphology consists of SACs segregated from normal host tissue by layers of necrotic and healthy PMN innate immune cells.⁷⁶ Recruited PMNs phagocytose bacteria and release numerous antimicrobial compounds including reactive oxygen and nitrogen species, antimicrobial peptides, and digestive enzymes.⁸⁴ Staphylococcal dissemination within a vertebrate host relies on a diverse array of virulence factors.¹³⁸ Many of these virulence factors are involved in evasion or resistance against immune mediated killing. One such example is the production of lysyl-PGs by MprF and subsequent incorporation within the staphylococcal envelope. Comprised of synthase and flippase domains, MprF facilitates transfer of lysine from lysyl-transfer RNA to phosphatidylglycerol lipids to then be translocated to the outer membrane leaflet.¹³⁹ The decreased net negative charge of the altered membrane decreases electrostatic attraction from positively charged antimicrobials providing resistance against these compounds.¹⁴⁰ Absence of lysyl-PG production results in increased killing by human PMNs and attenuated virulence in a murine model of systemic infection.⁸⁰ Genetic modifications to MprF have been identified that result in increased

lysyl-PG abundance, attributed to increased activity by the synthase or flippase domains. Increased lysyl-PG production results in decreased susceptibility or resistance to daptomycin.¹⁴⁰⁻¹⁴² Emerging literature suggests that the staphylococcal abscess is a molecularly heterogeneous environment and therefore SACs elaborate differential gene expression across distinct abscesses and even within a single abscess.^{13, 143} This questions the abundance and distribution of lysyl-PGs produced by staphylococcal communities within infected tissue. However, the spatial structure and unique interplay of host and bacterial factors that comprise abscesses make *in vivo* studies of this interface challenging, and most technologies do not allow for the selection or enrichment of bacteria-specific metabolic factors from the complex chemical matrix of tissue.

Traditional discovery approaches to molecularly investigate tissue samples require solubilization, eliminating spatial information and diluting low abundance analytes of interest. MALDI IMS has proven its utility as an *ex vivo* technology to study host-pathogen chemical interactions at sites of infection.^{11-14, 77, 87, 88, 143-145} The distribution and abundance of any mass-to-charge ratio can be mapped across the measurement area as an ion image.¹⁴ Recent advancements in IMS instrumentation allow for unprecedented molecular specificity and spatial fidelity, in some instances approaching sub-cellular resolution.¹⁴⁶⁻¹⁴⁸ Despite advances in imaging technologies, there is no universal technique or modality that can capture all molecular and morphological information in a single experiment. Thus, the incorporation of multiple co-registered or computationally fused imaging modalities can provide new information about a tissue's surface.^{94, 107} Application of various endogenous fluorescent markers, such as transgenic host fluorophores or bacterial fluorescent reporters, can drive IMS data mining strategies and interpretation.⁹³ In this type of workflow, fluorescence microscopy data can be obtained prior to IMS without effects on the molecular signatures detected by mass spectrometry. Furthermore, both datasets can be

acquired from a single tissue section, eliminating any issues with registration between serial sections. Herein, we leverage high performance MALDI FT-ICR IMS informed by fluorescence micrographs of transcriptional bacterial reporters to investigate the presence and distributions of *S. aureus* lysyl-PG lipids within soft tissue infections.

Results

Differential Distributions of S. aureus Lysyl-PGs are observed within Murine Abscesses

To investigate molecular species co-localizing with SACs, *S. aureus* infected tissues were analyzed using a multimodal approach integrating fluorescence microscopy, MALDI IMS of lipids, and H&E staining (Figure 1). A systemic model of staphylococcal infection was completed by intravenously inoculating mice with *S. aureus* *P_{mntA}Rfp*, where red fluorescent protein (RFP) expression is driven by the *mntA* promoter, a gene whose expression increases upon manganese starvation.¹³ Seven DPI, tissues were harvested, frozen on dry ice, and thinly sectioned for analyses. Visual comparison of the H&E stain and the fluorescence micrograph show co-localization of the RFP fluorophores to the SACs (Figure 1A & 1B). All SACs present within the abscess express the RFP reporter. Fluorescence microscopy of the RFP reporter is a chemically non-destructive approach to distinguish bacterial foci prior to IMS. An ion image overlay (Figure 1C) of various murine and bacterial molecular species highlights the power of IMS to molecularly interrogate complex tissue environments without the use of tags or labels.

To isolate and explore relationships of ions that localize to bacterial foci, data-driven image fusion was employed. This computational method of data analysis connects the spatial and informational content of two imaging modalities by constructing a mathematical cross-modality model using multivariate linear regression.¹⁰⁷ Data-driven image fusion has previously been

applied to various studies for sample prediction such as spatial sharpening and out-of-sample predictions.^{107, 108, 149} However, this discovery application of data-driven image fusion only executes the first model-building phase of the fusion framework. The prediction portion of data-driven fusion is not necessary for this approach, avoiding uncertainties inherent to predictions. IMS images are tied to a fluorescence micrograph using multivariate linear models, isolating correlative relationships between the two modalities. Specifically, we searched for relationships between IMS data and the RFP bacterial reporter, isolating ions of bacterial origin.

Fusion of the IMS and fluorescence microscopy datasets isolated many ions with high correlations to the RFP fluorescent reporter (Table 3.1). Database searching using The LIPID MAPS Lipidomics Gateway (<http://www.lipidmaps.org/>) resulted in tentative identification of many, but not all, ions of interest. MALDI MS/MS experiments to profile fluorescent bacterial foci resulted in the molecular identification of lysyl-PGs (Figure 3.2). Lysyl-PGs in Figure 1D are not present at all locations of bacterial fluorophores. This suggests differential production of lysyl-PG across distinct SACs within the same abscess. An extracted MALDI MS spectrum (Figure 1E) from a single pixel co-localizing with a SAC is annotated for three lysyl-PGs. Notably, tissue abscesses were not observed within infection models of *S. aureus* Δ_{mprF} (Figure 3.3). By leveraging multiple imaging modalities, heterogenous distributions of lysyl-PGs were mapped to staphylococcal communities within a murine infection model.

<i>m/z</i>	Lipid Identification	Database Matches	Ppm Error	Image Fusion Relative Slope (TRITC)
687.5438	PE-Cer(d36:1)	1	1.3	1143.5
735.5178	PG(33:0)	3	0.6	544.1
797.6531	PE-Cer(d44:2)	1	1.4	354.2
616.4720	CerP(d34:1)	2	1.3	346.9
707.4871	PG(31:0)	3	0.3	343.9
835.5811	Lysyl-PG(31:0)	2*	0.9	336.4
863.6132	Lysyl-PG(33:0)	3*	0.1	305.8
747.5162	PG(34:1)	4	2.7	262.7
699.4974	PA(36:2)	4	0.5	174.7
721.5044	PG(32:0)	4	2.7	140.7
849.5987	Lysyl-PG(32:0)	1*	1.5	102.2

Table 3.1: Image Fusion Data Mining Results

Table 3.1 shows selected ions isolated by image fusion of IMS data and fluorescence microscopy of the red fluorescent protein bacterial reporter. Lipid identifications are based on accurate measurements. Asterisks indicate that the final identification was not present within the database. Part per million (ppm) errors are calculated using theoretical *m/z* values. Error values were calculated by comparison to a single extracted spectrum that was calibrated internally using known lipid species. The image fusion relative slope is for the TRITC channel, corresponding to the bacterial RFP reporter. All ions and relative slopes for all fluorescence channels are present in the supplemental materials.

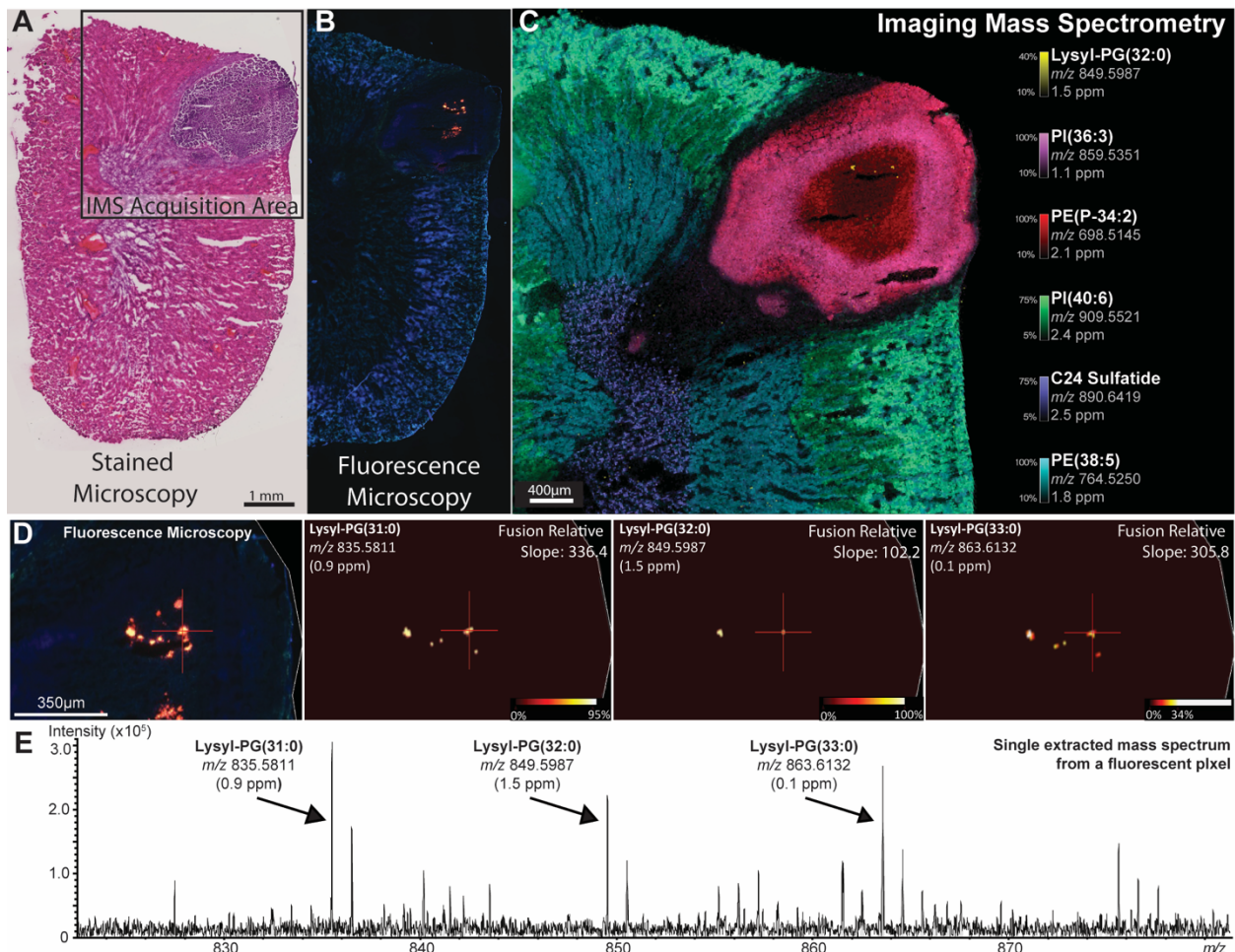


Figure 3.1: MALDI IMS Informed by Bacterial Fluorescent Reporters Isolates *S. aureus* Lipids

MALDI IMS spatially informed by fluorescence microscopy of *S. aureus*, *P_{mntArfp}* maps chemical information from staphylococcal colonies. (A) An H&E stain of a 10 DPI murine renal tissue section shows an abscess. (B) A fluorescence micrograph the same tissue section as A and C prior to MALDI IMS highlights the location of SACs (RFP). (C) An ion overlay image highlights the various molecular constituents of the abscess and chemical complexity of the tissue section. (D) Ion images were generated from signals co-localizing with RFP fluorophores (red crosshairs). Lysyl-phosphatidylglycerol lipid species were isolated based on spatial localizations and identified by subsequent MALDI MS/MS experiments. (E) A zoom of single extracted mass spectrum shows signals corresponding to lysyl-PGs.

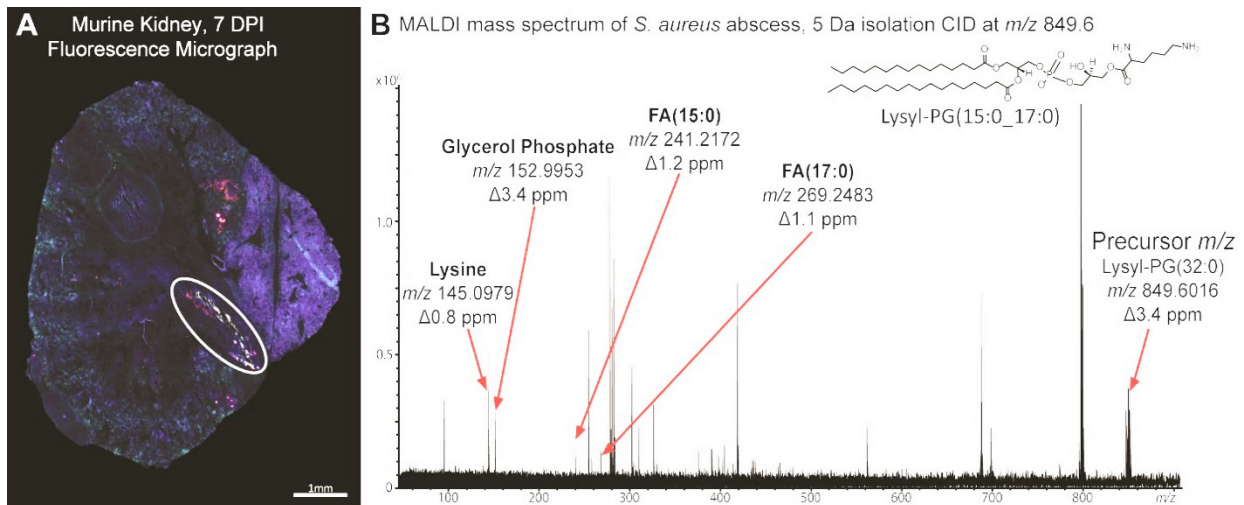


Figure 3.2: MALDI MS/MS Profiling of Lysyl-Phosphatidylglycerol Lipids at Sites of Infection

Identification of *S. aureus* lysyl-PG lipid species from the infection environment using on-tissue MALDI MS/MS. (a) A Non-destructive fluorescence microscopy image of the RFP bacterial transcriptional reporter allowed for spatial targeting using MALDI MS/MS. Using many laser shots directed at the indicated area (circle), a 5 Da isolation window was centered on m/z 849.6 to perform collision induced dissociation (CID). (b) The resulting MALDI MS/MS spectrum identified the ion at m/z 849.6 as lysyl-PG(15:0_17:0) based on the resulting fragments. Other ions were observed in the spectrum due to the large isolation window needed to generate enough ions for analysis. A predicted molecular structure is present within the spectrum, depicting the location of the lysine modified to the glycerol head group of the phospholipid chemical species.



Figure 3.3: Tissue Stains from an Infection Model Using a *S. aureus* Genetic Mutant Inactivated for Lysyl-Phosphatidylglycerol Production

Systemic infection model of *S. aureus*, Δ_{mprF} do not present with kidney tissue abscesses at 7 DPI. A) A murine kidney tissue section infected with *S. aureus* wildtype show typical abscess formation expanding the tissue section (white arrows). Bacterial presence can also be observed from the ureter of the tissue (yellow arrows). B) Murine kidney tissue sections infected with *S. aureus*, Δ_{mprF} in biological triplicate do show abscess formation. Bacteria can be observed in the ureter of two of the tissue sections (yellow arrows).

S. aureus Lysyl-PGs and Host Cationic Antimicrobial Peptides are Present in Human

Endocarditis Infections

Infective endocarditis is an infection of the endocardium, or the inner tissue lining of cardiac chambers and valves. These infections, commonly termed vegetations, are associated with both high morbidity and mortality among human patients. *S. aureus* is the most common causative pathogen for this disease.¹⁵⁰⁻¹⁵² To investigate the presence of lysyl-PGs within these infections, human tissue from patients with community acquired- methicillin sensitive *S. aureus* (CA-MSSA) infective endocarditis was subjected to MALDI IMS of lipids. Figure 3.4A shows a graphic of an infected aortic valve within a human heart. This highlights the location of the excised tissue shown in an H&E stain. An H&E stain is annotated for diseased and normal tissue regions. Like soft tissue abscesses, endocarditis vegetations are composed of recruited innate immune cells and SACs. Ion images from MALDI IMS of lipids performed on a serial tissue section (Figure 3.4B) show localizations of both *S. aureus* PGs and lysyl-PGs. Single extracted spectra annotated for the

lipids are present in Figure 3.5. Similar to previous observations from ion images of infected murine tissue (Figure 3.1C – 3.1E), distributions of the two lipid classes are not overlapping. Furthermore, lysyl-PGs localize closer to normal valve tissue in the analyzed human tissue sample.

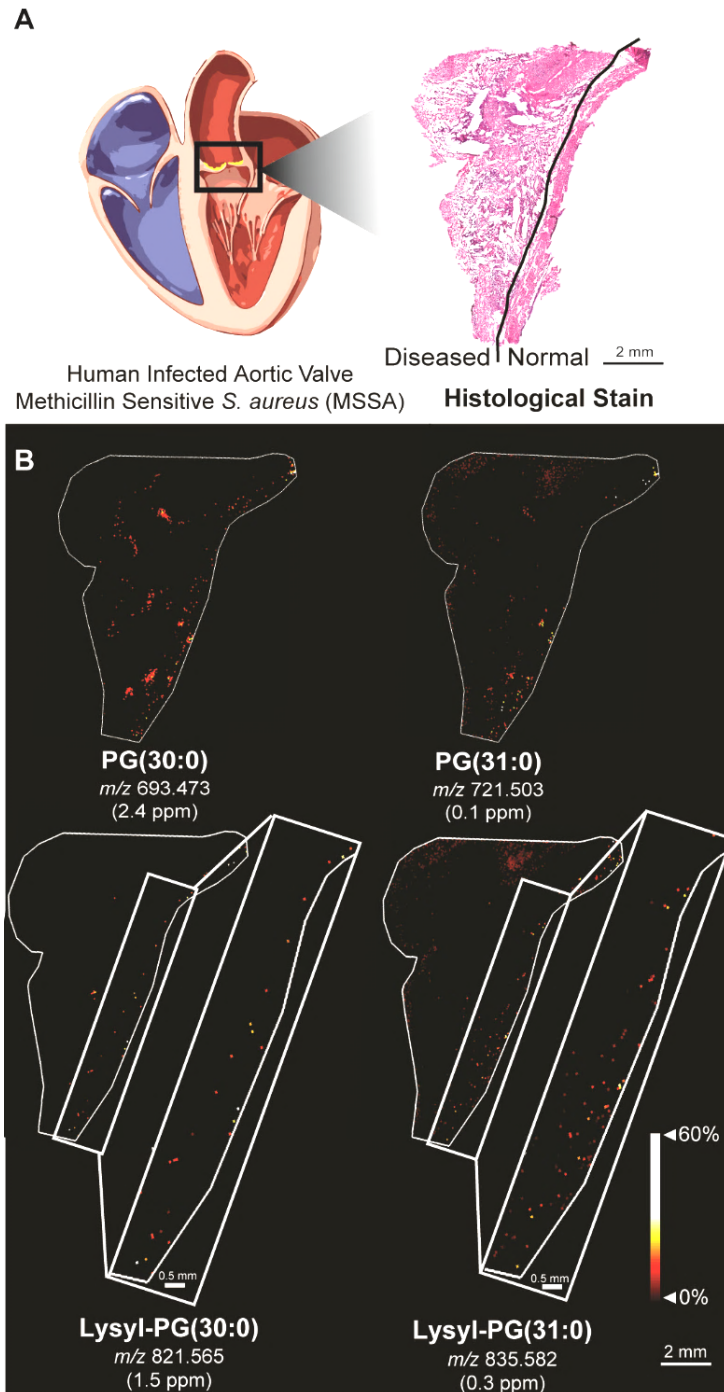


Figure 3.4: *S. aureus* Lysyl-Phosphatidylglycerol Lipids from Human Infective Endocarditis Tissue

MALDI IMS of lipids from infective endocarditis tissue reveals *S. aureus* PGs and lysyl-PGs. (A) A graphic depicts infected human heart tissue lesions. A tissue stain of an infected heart lesion is annotated for normal and diseased tissue. (B) Ion images of *S. aureus* PGs show distributions across the diseased tissue. Increased presence of lysyl-PGs can be observed near normal tissue (zoom).

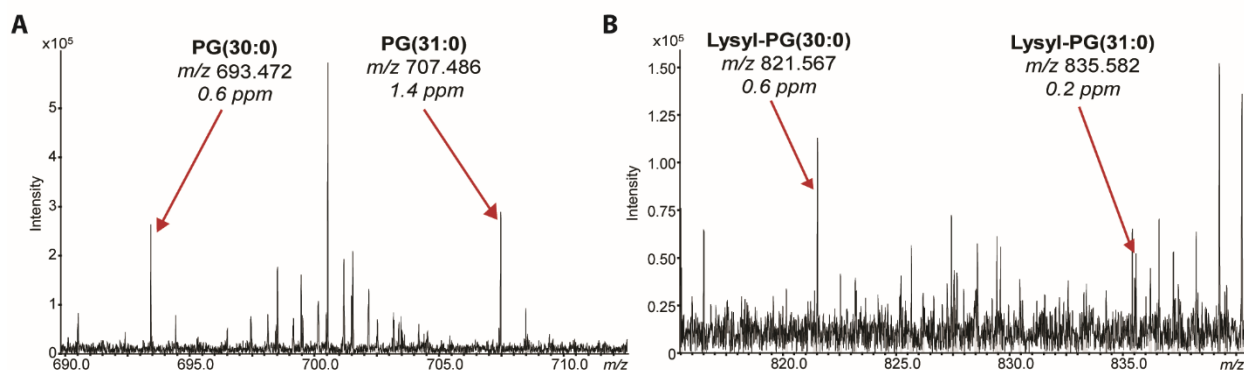


Figure 3.5: Single Extracted Spectra from MALDI IMS of Human Infective Endocarditis Tissue

Single extracted spectra from MALDI IMS of lipids from infective endocarditis tissue are annotated for lipid species of bacterial origin. (A) Two PG lipids are annotated with low ppm errors. (B) Two lysyl-PG lipids are annotated with low ppm errors.

Furthering this investigation of CA-MSSA endocarditis, MALDI IMS of intact proteins was acquired from a serial tissue section. Spectral examination of the averaged IMS spectrum (Figure 3.6) revealed the presence of 2 high intensity protein distributions at approximately m/z 3371 and m/z 3442. Ion images of the two species revealed distributions that span the entirety of the diseased regions of the tissue (Figure 3.6). Subsequent bottom-up LC-MS/MS workflows identified these analytes as α -Defensin 2 and α -Defensin 1 CAMPs, Figure 3.7b. Accurate mass measurements from FT-ICR IMS identify the distributions with low ppm mass errors. Notably, the CAMPs are absent from the normal valve tissue. It is hypothesized that the presence of CAMPs provokes lysyl-PG production, potentially influencing the location of lysyl-PGs in the MALDI IMS of lipids from the serial tissue section. Expanding on the observations from a murine model of infection, heterogeneous distributions of lysyl-PGs as well as host CAMPs were mapped to human infected tissue.

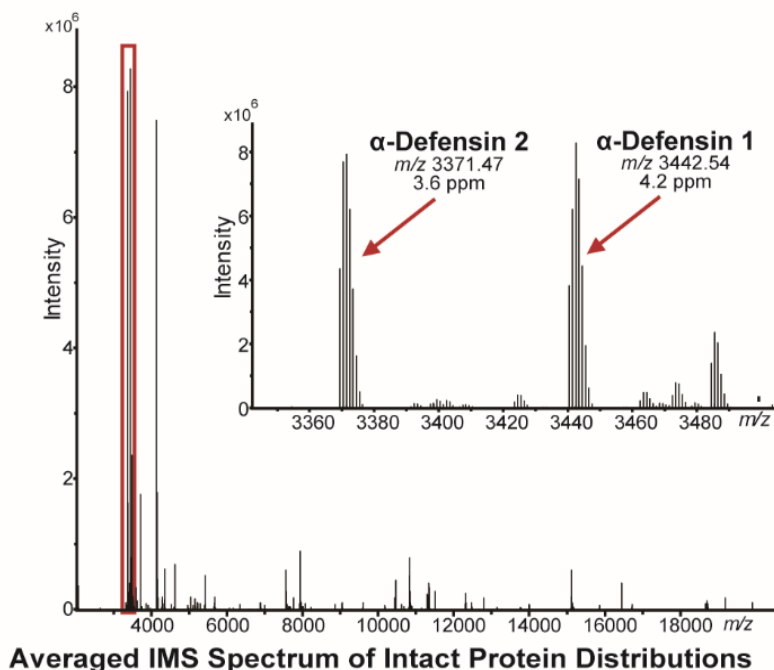


Figure 3.6: Averaged IMS Spectrum of Intact Protein Distributions from Human Infective Endocarditis Tissue

An averaged IMS spectrum of intact proteins show high intensity signals from m/z 3000- 4000. A zoom of this region shows the isotopic resolution of the signals. The signals were identified as α -Defensin 2 and α -Defensin 1, respectively, by accurate mass measurements when compared to LC-MS/MS measurements. The m/z values listed as well as the ppm errors refer to the most intense isotope within the distributions for each.

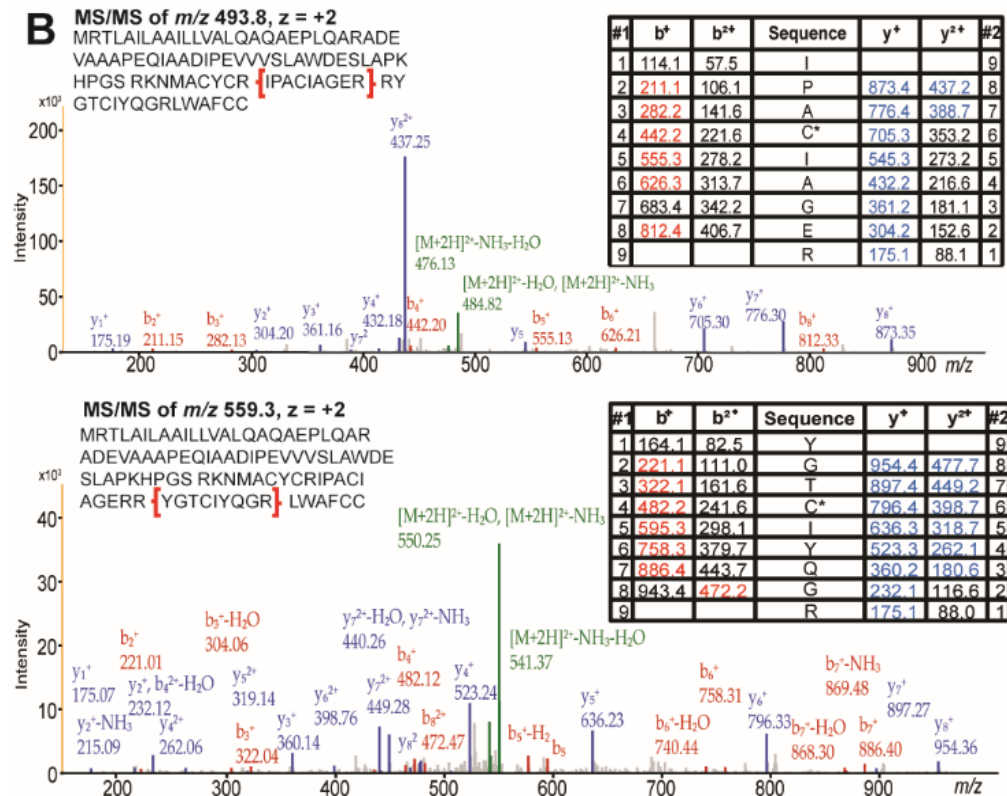
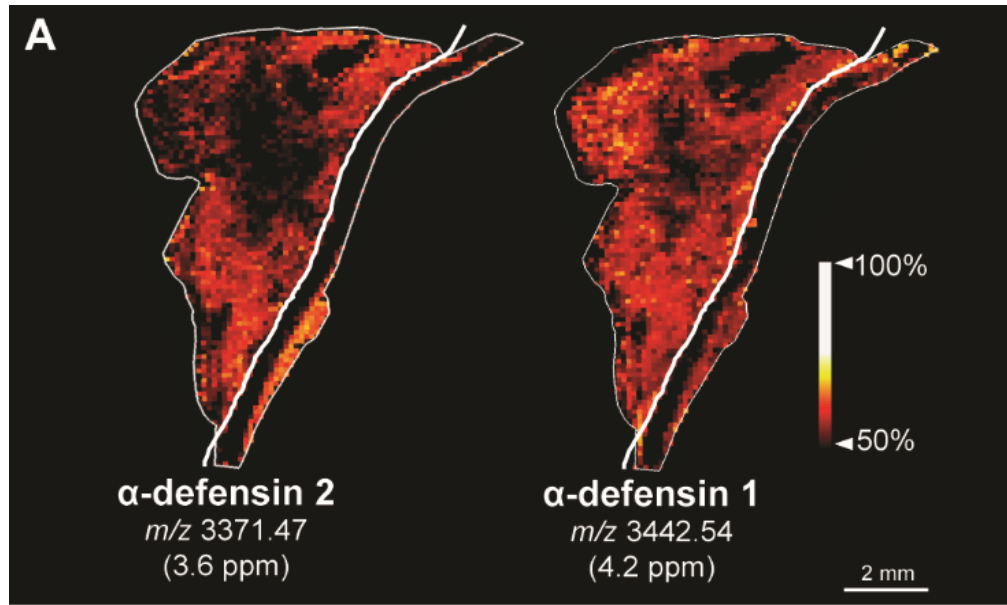


Figure 3.7: MALDI IMS of Intact Proteins and Subsequent LC-MS/MS Analysis from Human Infective Endocarditis Tissue

MALDI IMS of intact proteins from infective endocarditis tissue reveals CAMPs colocalizing with diseased tissue (A) Ion images of host CAMPs, α -Defensin 2 and α -Defensin 1 show high abundances within diseased tissue. (B) LC-MS/MS spectra from bottom up proteomics workflows show peptides from α -Defensin 2 and α -Defensin 1.

Discussion

In this work, we mapped host and staphylococcal molecular responses within infection environments. A multimodal imaging approach combining fluorescence microscopy and MALDI IMS was mined using a computational strategy to isolate ions with correlative spatial relationships to a bacterial fluorescent reporter. A subsequent experiment identified many of the highly correlated ions to be lysyl-PG lipids. Lysyl-PGs and CAMPs were subsequently mapped to endocarditis infection within human tissue. Heterogeneous distributions of lysyl-PGs were observed from both experiments, highlighting the potential for niche specific responses during infection.

These results provide insight into mechanisms of host innate immunity and bacterial pathogenesis at the site of infection. While the production of lysyl-PGs by *S. aureus* is attributed to virulence and antimicrobial resistance, this evasive response had yet to be observed in vivo.¹⁴⁰⁻¹⁴² Lysyl-PGs are not present at all SACS within a murine infection model. This suggests differential molecular responses to host stresses or mechanisms of innate immunity. Lysyl-PG distributions from a human endocarditis tissue sample show the heterogeneous presence of lysyl-PGs with *S. aureus* PGs and suggests variation in molecular responses, potentially relating to fitness. Distributions of α -Defensin 1 and α -Defensin 2 CAMPs localize to diseased tissue and are absent from normal valve tissue. However, increased presence of lysyl-PGs localizes near the normal valve tissue. Presence of the lipids at that location as well as the lack of CAMPs could be due to bacterial evasion of the innate immune system. Defensins were not observed from systemic infection models due to the lack of production by mice.

Many studies have highlighted the molecular heterogeneity present in *S. aureus* tissue infections.^{13, 143, 153} While the in vitro roles of lysyl-PGs and other various pathogenic adaptations

are known, it is not clear when and where these adaptations are most important during infection.^{80, 139, 141, 142, 154} Molecular heterogeneity across infectious foci could be explained by differential responses or mechanisms of host-pathogen interactions, highlighting the potential for niche-specific *S. aureus* pathogenic strategies. Organ-specific responses to infection may also exist. Increased understanding of when and where these pathogenic adaptations are required for bacterial proliferation can drive the search for alternative, novel therapeutics.

Spatial molecular technologies such as MALDI IMS will assist in relating molecular heterogeneity to conditions, environments, or other, previously uncharacterized, molecular distributions to further elucidate host-pathogen interactions. Due to the lack of tags or labels, IMS allows for untargeted chemical information from a tissue surface, not achievable by other technologies. Furthermore, untargeted molecular analysis of staphylococcal infections, as provided by MALDI IMS, can drive the search for uniformly expressed bacterial factors, as these factors can serve as candidates for vaccine targets. Incorporation of other imaging modalities to MALDI IMS, as exhibited here, allows for increased information about a tissue surface, expanding testable hypotheses. Application of automated data mining strategies, such as data-driven image fusion, can isolate relationships between datasets. Leveraging this spatial information, chemical mechanisms of bacterial pathogenicity and antibiotic resistance as well as host innate immunity were mapped across infections in murine and human tissue.

Methods

Materials

Ammonium formate, hematoxylin, and eosin were purchased from Sigma Aldrich (St. Louis, MO, USA). 1,5-diaminonaphthaline (DAN) and 2,5-dihydroxyacetophenone (DHA) were also purchased from Sigma Aldrich (St. Louis, MO, USA) then purified by recrystallization. Indium tin oxide (ITO) coated slides were purchased from Delta Technologies, Limited (Loveland, CO, USA). All solvents (methanol, ethanol, acetonitrile, acetic acid, chloroform, and xylenes) and optimal cutting temperature compound were purchased from Fisher Scientific (Kalamazoo, MI, USA).

Bacterial Strains and Growth Conditions

Bacterial strains, primers, and plasmids used in this study are listed in Table 3.2. Bacteria were routinely cultured at 37°C in Difco Tryptic Soy Broth (TSB) or on Tryptic Soy Agar (TSA) with 10 µg/mL erythromycin or 10 µg/mL chloramphenicol antibiotics supplemented as needed. All growth in liquid medium occurred in an Innova 44 incubator shaking at 180 rpm, unless otherwise noted. Fifteen-milliliter round-bottom polypropylene tubes with aeration lids at a 45° angle were used for all standard cultures of 5 ml. The *S. aureus* clinical osteomyelitis isolate strain Newman served as the genetic background for all experiments.¹⁵⁵ The construction of *S. aureus* strain Newman p.P_{mntA}rfp has previously been described.¹³ The strain inactivated for lysyl-PG production (*mprF::erm*) has also been previously described.⁸⁰

Strain	Genotype	Description	Reference
Newman	WT	Wild-type, methicillin-sensitive clinical isolate	¹⁵⁶
Newman	<i>mprF::erm</i>	In frame deletion of <i>mprF</i> gene marked with erythromycin resistance cassette	⁸⁰
Plasmid		Description	
pOS1 P _{<i>mntA</i>} <i>rfp</i>		<i>mntA</i> promoter driving expression of a red fluorescent protein, responds to manganese starvation.	¹³

Table 3.2: *S. aureus* Strains, Plasmids, and Primers Used

Murine Model Procedures

All animal experimental protocols were reviewed and approved by the Vanderbilt University Institutional Animal Care and Use Committee (IACUC) and are in compliance with institutional policies, NIH guidelines, the Animal Welfare Act, and American Veterinary Medical Association guidelines on euthanasia. *S. aureus* strains were streaked from freezer stocks onto TSA with antibiotics, as required, and grown for 24 h at 37°C. Isolated colonies were used to prepare overnight cultures in 5 mL TSB. For all experiments, 6-8 week old female BALB/cJ mice (Jackson Laboratory) were retro-orbitally infected with 1 x 10⁷ CFU in 100 µl of sterile phosphate-buffered saline as previously described.¹⁵⁶ Following infection, mice were humanely euthanized on day 4, 7, or 10. The kidney, hearts and livers were removed and immediately frozen on a bed of dry ice. Tissues were stored at -80°C until needed for further processing.

Patients and Endocarditis Vegetations

Vegetations were collected prospectively during open-heart surgery for infective endocarditis under an approved Cleveland Clinic Institutional Review Board protocol with verbal patient consent (Protocol #16-1521). Visible blood clots on vegetations were removed with forceps and residual blood was reduced by extensive rinsing in phosphate buffered saline. Vegetations analyzed using LC-MS/MS were snap-frozen in liquid nitrogen and stored at -80 °C.

Sample Preparation

Fresh frozen tissues were serially sectioned at 10 μm using a Leica CM3050s cryostat (Leica Biosystems, Buffalo Grove, IL, USA) and thaw mounted on glass microscope slides (Fisher Scientific, Kalamazoo, MI, USA) or indium tin oxide (ITO) coated glass slides (Delta Technologies, Loveland, CO, USA). Sections were stored at $-80\text{ }^{\circ}\text{C}$ until thawed for analysis under vacuum for approximately 15 minutes. MALDI matrix for lipid analysis was applied by a robotic aerosol sprayer (TM Sprayer, HTX Technologies, Chapel Hill, NC, USA). Samples for the analysis of lipids were washed using ammonium formate buffer as reported previously then homogeneously coated with DAN using optimized conditions at a surface density of $3.6\text{ }\mu\text{g}/\text{mm}^2$.³⁰ Samples for the analysis of intact proteins were washed of lipids and salts as previously reported then homogeneously coated with DHA using optimized conditions at a surface density of $3.1\text{ }\mu\text{g}/\text{mm}^2$.⁴⁰ Samples for protein analysis were then recrystallized as previously reported.¹⁹ Post-MALDI IMS, tissue sections were washed of matrix using methanol and stained with hematoxylin and eosin (Fisher Scientific, Kalamazoo, MI, USA). Bright field images of stained sections were acquired using a Leica SCN-400 optical slide scanner (Leica Biosystems, Buffalo Grove, IL, USA) at 20X magnification.

Fluorescence Microscopy Image Acquisition

Fluorescence microscopy images were acquired from tissue sections on ITO coated slides before tissue washing or matrix application using a fluorescence microscope (Nikon Eclipse 90i, Nikon Instruments Inc., Melville, NY, USA) equipped with a motorized stage and a 10X objective. Resulting pixel resolutions were $0.92\text{ }\mu\text{m}/\text{pixel}$. A TRITC (excitation = 528–553, emission = 590–

650) specific epifluorescence filter was used to visualize the RFP reporter at an exposure time of 40 ms. DAPI (excitation = 340–380, emission = 435–485) and FITC (excitation = 465–495, emission = 515–555) specific epifluorescence filters were used to allow visualization of tissue morphology by autofluorescence at exposure times of 100 ms and 150 ms, respectively.

Molecular Image Acquisition and Visualization

MALDI IMS of lipids was performed using a modified 9.4T FT-ICR MS (SolariX, Bruker Daltonics, Billerica, MA, USA) equipped with an Apollo II dual MALDI/ESI source and a dynamically harmonized ParaCell. The source region of this instrument is modified with a secondary Gaussian laser, resulting in incident spots sizes $< \sim 10 \mu\text{m}$. Molecular images of lipids were acquired at pixel spacings of $15 \mu\text{m}$ for murine tissue ($\sim 10 \mu\text{m}$ laser beam size, 500 laser shots) and $40 \mu\text{m}$ for human tissue ($\sim 30 \mu\text{m}$ laser beam size, 500 laser shots) in both the x and y directions. Data were collected from m/z 200 to 2,000 in negative ionization mode with a resolving power ($m/\Delta m$) of $\sim 50,000$ at m/z 500. The time domain file size was set to 512k (free induction decay: 0.28 s). The ion optics were tuned to maximize transmission at the defined m/z range including the funnel RF amplitude (250 V_{pp}), source octopole (5 MHz, 400 V_{pp}), collision cell (collision cell voltage: 2.0 V, cell: 2 MHz, 1200 V_{pp}), time-of-flight delay (0.9 ms), transfer optics (4 MHz, 325 V_{pp}), and quadrupole (Q1 mass: m/z 350). The source DC optics were tuned to maximize ion transmission and observed intensities (capillary exit -190 V, deflector plate: -200 V, plate offset: -100 V, funnel 1: -100 V, skimmer 1: -20 V) as well as the ICR cell parameters (transfer exit lens: 10 V, analyzer entrance: 10 V, side kick: 0 V, side kick offset: 6.0 V, front trap plate: -1.200 V, and back trap plate: -1.205 V). Ion detection was performed using a sweep excitation power of 22%.

MALDI IMS of intact proteins was performed using a 15T FT-ICR MS (SolariX, Bruker Daltonics, Billerica, MA, USA) equipped with an Apollo II dual MALDI/ESI source and a dynamically harmonized ParaCell. The MALDI source employs a Smartbeam II 2 kHz, frequency tripled Nd:YAG (355 nm) laser. Molecular images of intact proteins were acquired at pixel spacings of 100 μm for murine tissue with a ~ 50 μm laser beam size (750 laser shots) in both the x and y directions. Data were collected from m/z 2,000 to 30,000 in positive ionization mode with a resolving power ($m/\Delta m$) of $\sim 60,000$ at m/z 10,000. The time domain file size was set to 1M (free induction decay: 4.61 s). The ion optics were tuned to maximize transmission at the defined m/z range including the funnel RF amplitude (285 V_{pp}), source octopole (2 MHz, 525 V_{pp}), collision cell (collision cell voltage: -8.0 V, cell: 1.4 MHz, 1850 V_{pp}), time-of-flight delay (3.00 ms), transfer optics (1 MHz, 410 V_{pp}), and quadrupole (Q1 mass: m/z 1,000). The source DC optics were tuned to maximize ion transmission and observed intensities (capillary exit 250 V, deflector plate: 200 V, plate offset: 100 V, funnel 1: 150 V, skimmer 1: 60 V) as well as the ICR cell parameters (transfer exit lens: -20 V, analyzer entrance: -10 V, side kick: 0 V, side kick offset: -1.5 V, shimming DC bias: 1.5 V, and gated injection DC bias: 1.5 V, back trap plate quench: -30 V). The gated trapping and detection function of the ICR cell was enabled (front and back plates for trapping: 2.5 V, front and back plates for detection: 1.1 V, ramp time: 0.01 s). Ion detection was performed using a sweep excitation power of 45%. FlexImaging 5.0 (Bruker Daltonics, Billerica, MA, USA) and SCiLS Lab (version 2016b, Bruker Daltonics, Billerica, MA, USA) were used to normalize intensities (root mean squared) and visualize ion images.

Data-driven Image Fusion

For image fusion analysis with IMS data sets, the mass spectrometry data were treated as a data cube in which the x and y coordinates are pixel dimensions and the z coordinate is m/z. Analogously, the microscopy data map pixel dimensions are x and y, but the z coordinate was the color channels. Image fusion algorithms were used to create a cross-modality model. The model was then used to perform partial least squares regression correlation, comparing image pairs of IMS and fluorescence micrograph data. In the present work, relationships were mined to identify ions of interest that related to a specific color channel, or red to correlate IMS with the bacterial RFP fluorophore reporter. Further information on this algorithm can be found in previous work.¹⁰⁷

Protein Extraction for LC-MS/MS

150-200 mg of each vegetation was homogenized in 1 ml of extraction buffer (T-Per, ThermoFisher Scientific, Waltham, MA, USA) supplemented with protease inhibitor (cOmplete tablets, Roche, Millipore Sigma, Burlington, MA, USA) using a homogenizer (T10 ultra Turrax, IKA, Staufen, Germany), boiled at 95°C for 5 minutes and cooled to room temperature before adding 1 µl of benzonase (Millipore Sigma, Burlington, MA, USA). The homogenates were probe tip sonicated (Q-500 sonicator, Qsonica, Newtown, CT, USA) at 20% amperage with 3 sec on/off intervals a total of 6 times, centrifuged at 15,000 g for 10 minutes, and the supernatant was retained for analysis as the soluble fraction (T-Per fraction). The pellet was washed twice with cold PBS and resuspended in a chaotropic buffer (5 M GuHCL, 1% CHAPS, 25 mM NAC₂H₃O₂, 50 mM aminocaproic acid, 5 mM NA₂EDTA) supplemented with protease inhibitor (cOmplete tablets, Roche, Millipore Sigma, Burlington, MA, USA) at 4°C with rotation for 72 h, centrifuged at 17,000 g for 10 minutes and the supernatant was retained for analysis as the matrix fraction.

Fractions were analyzed separately, and data was combined by sample post database search analysis.

LC-MS/MS Data Acquisition and Analysis

Peptide samples were analyzed using a ThermoFisher Scientific Fusion Lumos tribrid mass spectrometer system interfaced with a Thermo Ultimate 3000 UHPLC. The HPLC column was a Dionex 15 cm x 75 μm inner diameter Acclaim Pepmap C18, 2 μm , 100 \AA reversed phase capillary chromatography column. 5 μL volumes of the trypsin-digested extract were injected, peptides were eluted from the column by an acetonitrile/ 0.1% formic acid gradient at a flow rate of 0.3 $\mu\text{L}/\text{min}$ and introduced in-line into the mass spectrometer over a 120-minute gradient. The nanospray ion source was operated at 1.9 kV. The digest was analyzed using a data-dependent method with 35% collision-induced dissociation fragmentation of the most abundant peptides every 3s and an isolation window of 0.7 m/z . Scans were conducted at a maximum resolution of 120,000 for full MS and 60,000 for MS/MS. Individual LC-MS/MS raw files were searched against a human database (Uniprot.org) using Proteome Discoverer 2.2 (Thermo Fisher Scientific, Waltham, MA, USA). Peptides were identified using a precursor mass tolerance of 10 ppm, and fragment mass tolerance of 0.6 Da. The only static modification was carbamidomethyl, whereas dynamic modifications included the light (28.03 Da) dimethyl formaldehyde (N-terminal), oxidation, deamidation, acetylation (N-terminal), and Gln to pyro-Glu N-terminal cyclization. Peptides were validated using a false discovery rate (FDR) of 0.01% against a decoy database.

CHAPTER IV

***STAPHYLOCOCCUS AUREUS* EXHIBITS HETEROGENEOUS SIDEROPHORE PRODUCTION WITHIN THE VERTEBRATE HOST**

This chapter was adapted from the previous published Perry et al., *Proceedings of the National Academy of Sciences*, Copyright 2019 by National Academy of Sciences.¹⁴³

Overview

Siderophores, iron scavenging small molecules, are fundamental to bacterial nutrient metal acquisition and enable pathogens to overcome challenges imposed by nutritional immunity. Multimodal imaging mass spectrometry allows visualization of host-pathogen iron competition by mapping siderophores within infected tissue. We have observed heterogeneous distributions of *Staphylococcus aureus* siderophores across infectious foci, challenging the paradigm that the vertebrate host is a uniformly iron deplete environment to invading microbes.

Introduction

Metals are required by living organisms to carry out fundamental metabolic processes since they are cofactors of approximately 50% of all enzymes.⁵⁵ During infection, host metalloproteins such as transferrin and lactoferrin (Fe dissociation constant (K_d) $\sim 10^{-22}$ M) act to sequester nutrient metals to prevent microbial colonization, a process termed nutritional immunity.^{81, 157} In turn, bacteria have evolved multiple mechanisms to compete with nutritional immunity, including the use of small molecule chelators termed siderophores.^{79, 158} Siderophores are low molecular weight metabolites (< 1 kDa) that are produced by many organisms, and are characterized by a high

binding affinity for Fe ($K_d > 10^{-30}$ M).^{79, 159} Due to their ability to efficiently scavenge for nutrient metals, the use of siderophores is a critical nutrient acquisition strategy of organisms within soil, healthy vertebrate microbiomes, and pathogenic bacteria.¹⁶⁰⁻¹⁶⁴ Chemical insight into siderophore synthesis and function from bacterial species within a host environment will increase understanding of microbe-microbe nutrient competition and mechanisms of pathogenesis.¹⁶⁴ *Staphylococcus aureus* is an opportunistic bacterial pathogen known to utilize multiple siderophores for Fe acquisition, and the production of these molecules is required for maximum virulence in a vertebrate host.^{79, 165}

S. aureus causes a broad range of life-threatening illnesses, ranging from soft tissue infections that present with abscess formation to systemic conditions such as sepsis.⁷⁵ Abscess architecture consists of staphylococcal communities segregated from normal host tissue by layers of necrotic and healthy PMNs, (Figure 2.1).⁷⁶ *S. aureus* experiences different degrees of Fe limitation across host abscess environments within the same tissue, calling into question when and where siderophores are important.¹³ Furthermore, functional redundancy of multiple siderophores secreted by *S. aureus* obfuscates the importance of each individual molecular species.⁷⁹ In Fe-limiting environments, transcriptional repression of the *S. aureus* ferric uptake regulator (Fur) regulon is ceased, and expression of molecular machinery required for Fe acquisition is increased.⁷⁹ Known mechanisms of staphylococcal Fe acquisition regulated by Fur include heme uptake and degradation, inorganic Fe transport, and the secretion of polycarboxylate-type siderophores staphyloferrin A and staphyloferrin B.^{166, 167} Emerging literature suggests that infectious lesions such as abscesses exhibit molecular heterogeneity, and therefore *S. aureus* exhibits differential gene expression depending on its location within tissue.¹³ Based on this emerging model, the traditional view that siderophores are uniformly expressed throughout an

animal may be incorrect.^{13, 79, 81, 164} Despite differential gene expression observed from abscesses, *S. aureus* siderophores have not previously been observed within a host environment.

MALDI IMS, a technology that allows in situ determination of the spatial distribution of thousands of analytes from a tissue surface without the need for chemical tags or probes, has demonstrated its utility in studying bacterial pathogenesis and host immune response *ex vivo*.^{14, 77} Analysis by MALDI IMS has driven the identification of molecular factors constructing this abscess morphology within murine models.^{11-13, 77, 87, 88} Many of these molecular features, of both host and pathogen origin, have been differentially observed from one abscess to another with respect to location and time post inoculation.¹³ Recent work using IMS has shown that a chosen MALDI matrix influences the observed analytes.¹¹¹ Here, novel MALDI IMS sample preparation techniques and high-performance FT-ICR MS enable visualization of heterogeneous distributions of *S. aureus* siderophores staphyloferrin A and staphyloferrin B across multiple infectious niches of a murine model of systemic infection.

Results

Comparison of Surface Coatings to Visualize Siderophores within Infected Tissue

The preparation of a tissue sample for IMS has a direct effect on the analytes observed.^{22, 30, 111, 168, 169} To observe siderophores from infected tissues, multiple surface coatings and sample preparations were completed in positive and/or negative ionization modes including robotic aerosol application of DAN, a 1:1 ratio of carbonate buffer (pH 10.3) and 250 mM sodium acetate then a layer of gold, a novel matrix mixture of TMGN and DABP, and a layer of silver, Figure 4.1. IMS averaged spectra from all acquisitions are present in Figure 4.1A and B. Spectra show the

presence of different signals, specifically in the $\sim m/z$ 600-1000 mass ranges. All IMS data were acquired from serial sections of *S. aureus* infected murine kidney. An H&E stain is present in Figure 4.1C. Spectra analysis resulted in the presence of a signal corresponding to a deprotonated staphyloferrin A ion using the TMGN / DABP matrix mixture in negative ionization mode, Figure 4.1D. An ion image generated from the IMS dataset shows localization of the ion to abscesses.

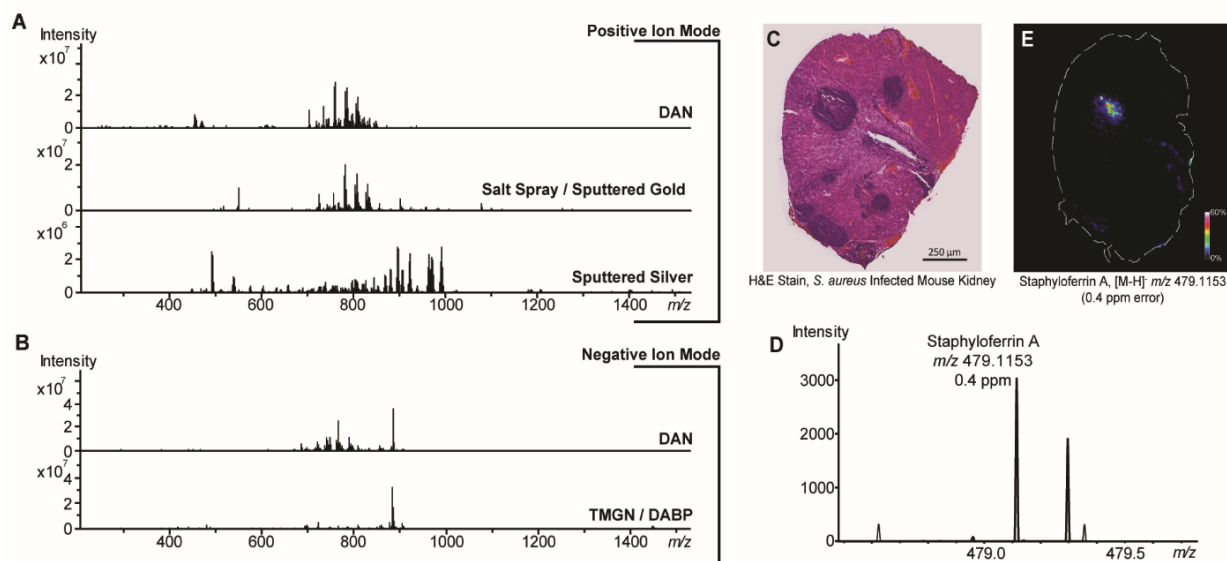


Figure 4.1: IMS Surface Coatings Comparison for Visualization of Staphyloferrin A Siderophore

Multiple surface coatings were compared when analyzed by MALDI IMS in positive (A) and negative ion modes (B). An H&E stain shows presence of abscesses (C) to be compared with distributions of an ion at m/z 479.1153, corresponding to staphyloferrin A (D – E).

Multimodal Imaging Mass Spectrometry to Visualize Nutritional Heterogeneity

To further interrogate molecular features present at the host-microbe interface, mice were infected with wildtype *S. aureus*.¹⁵⁶ Mice exhibited hallmark symptoms of sepsis including weight loss, piloerection, and lethargy.¹⁷⁰ Animals were euthanized 7 days post infection (DPI), and tissues were harvested and frozen on dry ice. Tissues were sectioned serially for H&E staining,

molecular analysis using MALDI IMS, and elemental Fe analysis using LA-ICP IMS (Figure 4.2a – 4.2d). Samples for MALDI IMS were prepared by applying a homogenous coating of DABP and TMGN to the surface of a tissue section. Low abundance ions were enriched by mass-to-charge selection and accumulation prior to mass analysis, enabling detection of ions corresponding to two *S. aureus* siderophores from the surface of the tissue (staphyloferrin A [M-H]⁻ at m/z 479.1155 (mass accuracy: 0.01 ppm error) & staphyloferrin B [M-H]⁻ at m/z 447.1369 (mass accuracy: 0.09 ppm error)) (Figure 4.2b & 4.2c). Tentative molecular identifications are based on accurate mass measurements. The staphyloferrin A molecular assignment was validated by MALDI IMS of mice infected with a *S. aureus* mutant genetically inactivated for staphyloferrin A production (Δsfa).¹⁷¹ Ion images and spectral data acquired from the *S. aureus* Δsfa infected tissue section showed an absence of the molecular signal of interest ([M-H]⁻ at m/z 479.1155), verifying our observation of staphyloferrin A in wildtype infected tissues (Figure 4.3).

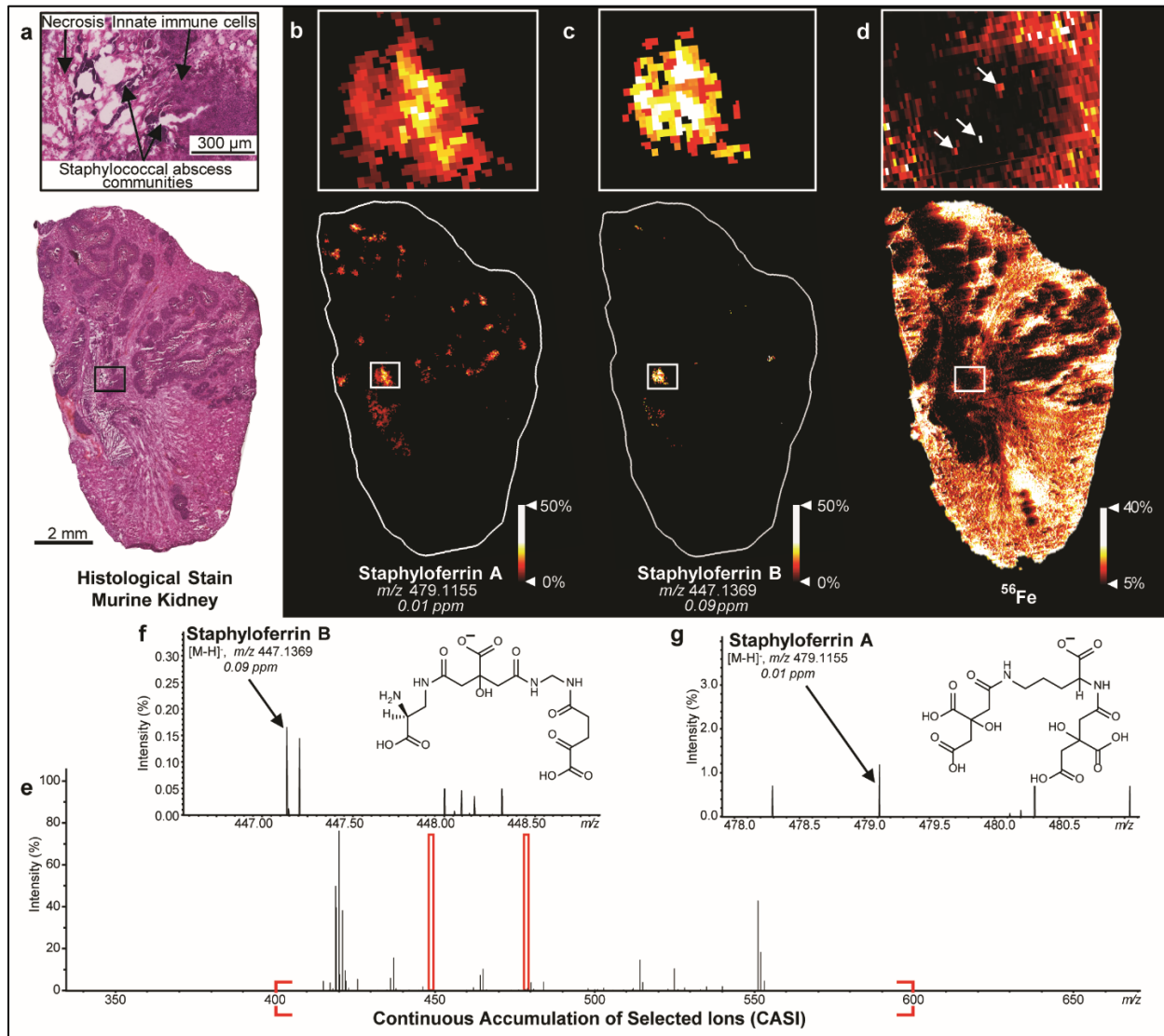


Figure 4.2: IMS of *S. aureus* Siderophores and Fe to Investigate Nutritional Immunity
 MALDI IMS reveals the presence of siderophores staphyloferrin A and staphyloferrin B within the infectious environment. (a) An H&E stain shows staphylococcal lesions. A zoom shows abscess morphology (arrows). (b) MALDI FT-ICR IMS at 35 μm spatial resolution shows staphyloferrin A co-localizing with sites of infection. (c) Staphyloferrin B co-localizes with sites of infection. This ion is more closely localized to the bacterial colonies than staphyloferrin A. (d) Fe distributions at 35 μm spatial resolution show Fe co-localizing with select colonies within the abscess zoom (arrows). However, most abscesses are void of Fe. (e) A MALDI IMS averaged spectrum highlights the number of signals observed. (f) A zoom from the spectrum shows a signal corresponding to staphyloferrin A at m/z 479.1155, 0.01 ppm mass error and the chemical structure of staphyloferrin A, $[\text{M}-\text{H}]^-$. (g) A zoom on the spectrum shows a signal corresponding to staphyloferrin B at m/z 447.1369, 0.09 ppm mass error and the chemical structure of staphyloferrin B, $[\text{M}-\text{H}]^-$. Adapted from Proceedings of the National Academy of Sciences, 2019, 201913991, “*Staphylococcus aureus* exhibits heterogeneous siderophore production within the vertebrate host” with permission from the National Academy of Sciences.¹⁴³

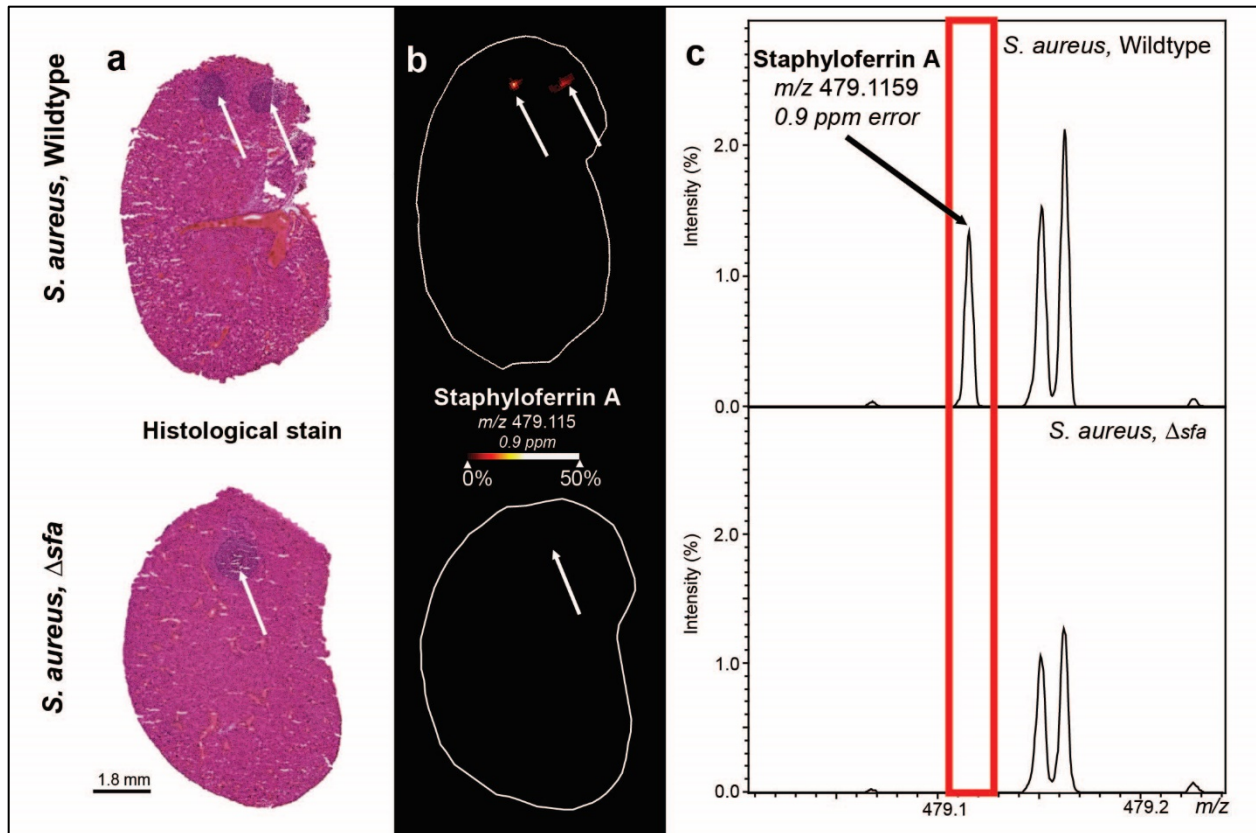


Figure 4.3: Confirmation of Staphyloferrin A Using a *S. aureus* Genetic Mutant

Analysis of a *S. aureus* genetic variant inactivated for staphyloferrin A production infection model confirms identity of the molecular signal *in vivo*. (a) Visual comparison of H&E stains from an infection of *S. aureus* wildtype and Δsfa shows lesions similar in morphology present in both infection models. (b) Generated ion images at 60 μm spatial resolution corresponding to staphyloferrin A show the absence of the molecular signal at the site of infection within the *S. aureus*, Δsfa infection model. (c) Averaged IMS spectra show the absence of the signal corresponding to staphyloferrin A. Reprinted from Proceedings of the National Academy of Sciences, 2019, 201913991, “*Staphylococcus aureus* exhibits heterogeneous siderophore production within the vertebrate host” with permission from the National Academy of Sciences.¹⁴³

Ion images of the siderophore signals within 7 DPI renal lesions localize to sites of infection and expand into necrotic regions of abscesses, distant from the staphylococcal communities (Figure 4.2a – 4.2c). The expansive distributions and diffusion of these siderophores highlight not only the amplitude of biosynthesis, but also the metabolic effort of abscess communities to acquire Fe. Large differences in siderophore production can be observed from one abscess to another. Comparing the distributions of the two siderophores, staphyloferrin A has an

increased prevalence at most sites of infection. However, some foci show higher relative abundances of staphyloferrin B, suggesting that these organisms are experiencing differential metal starvation across these infectious foci.

Host metalloproteins involved in nutritional immunity such as transferrin and lactoferrin aim to sequester Fe from the proliferating abscess communities to limit pathogenesis. To visualize this phenomenon, LA-ICP IMS was used to investigate the distribution of Fe (as ^{56}Fe) present in a serial section of the 7 DPI renal tissue (Figure 4.2d). Fe is largely excluded from sites of infection, but some pixels within the elemental Fe image show co-localization of the metal to staphylococcal abscess communities (Figure 4.1d arrows), presumably highlighting the success of these organisms at capturing Fe within infected tissue.

Comparing Siderophore Distributions across Lesions within Multiple Tissue Types

To further investigate how the Fe-specific nutritional immune response influences the distribution of staphylococcal siderophores at sites of infection, lesions in heart, liver, and kidney tissues were compared using a multimodal approach integrating IMS, histological staining, and fluorescence microscopy. Mice were systemically infected with a strain of *S. aureus* (*P_{isdA}gfp*), where green fluorescent protein (GFP) expression is driven from the Fur-regulated *isdA* promoter, a gene whose expression increases upon Fe starvation.¹³ After 10 DPI, H&E staining clearly showed formation of tissue abscesses (Figure 4.4). Fluorescence microscopy images of the GFP fluorophore in the in vivo labeled tissue sections allow a non-destructive, MALDI IMS compatible technique to visualize the response of abscess communities to host Fe sequestration (Figure 4.4). Autofluorescence microscopy of endogenous molecular components from the tissue sections allow for visualization of tissue structures. Generated ion images from the same tissue sections as the

fluorescence microscopy show siderophore distributions at sites of bacterial Fe starvation (Figure 4.4). Specifically, in Figure 4.4a – 4.4c the expanded images show siderophore distributions co-localizing with bacterial GFP expression. Comparing the H&E stain to the Fe elemental distributions, some communities co-localize with Fe while others do not. This observation supports nutritional heterogeneity of select staphylococcal communities within a single abscess, suggesting differential molecular responses.

Comparing abscesses across tissue types, lesions in liver tissue are larger than those found in kidney tissue. However, the majority of the kidney tissue section is diseased (Figure 4.4c). The heart contains the smallest lesions in size (Figure 4.4b). Molecular distributions show utilization of the siderophores by *S. aureus* to acquire Fe from the host across all tissues examined. Notably, siderophores all localize to the necrotic region of the abscess. However, a visual comparison of the abscess margins in H&E stained images and staphyloferrin A ion images of the heart abscess and a single kidney abscess show staphyloferrin A distributed outside of the abscess confinements, highlighting the range of siderophore distribution during infection (Figure 4.4b). Siderophore distributions localize closer to areas of GFP fluorescence signal signifying Fe starvation within the fluorescence microscopy image. The Fe distributions within the liver and kidney lesions (Figure 4.4a & 4.4c) localize to areas without GFP signal and lessened siderophore signals. It is important to note that little to no siderophore can be detected within some abscesses. These data highlight the differential production of siderophores across abscesses comprising liver, heart, and kidney tissues.

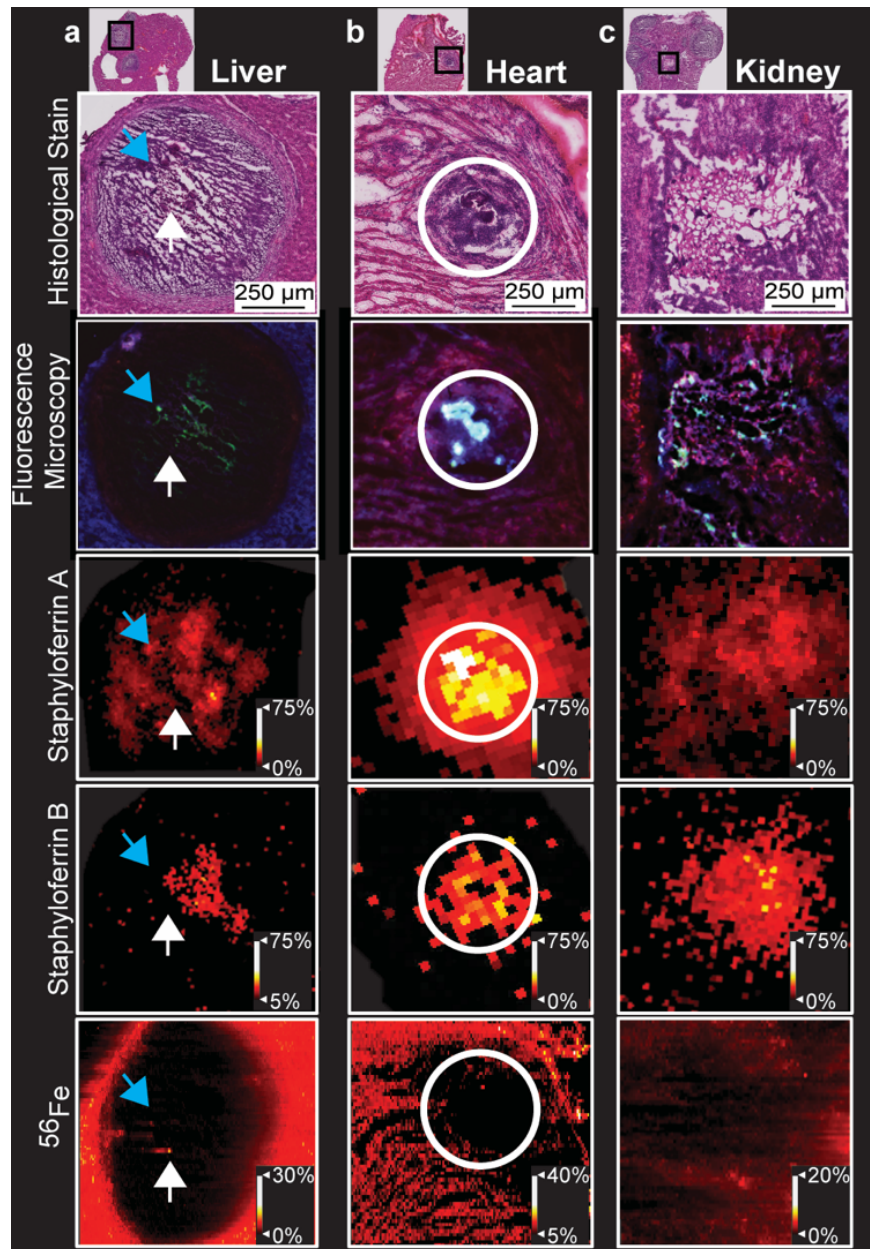


Figure 4.4: Multimodal IMS to Visualize Nutritional Immunity Across Tissue Lesions

Multimodal imaging of 10 DPI *S. aureus* $P_{isdA}Gfp$ infection characterizes utilization of staphyloferrin A and staphyloferrin B across tissue types. (a) Siderophore distributions localize to regions of staphylococcal Fe starvation (blue arrows). Fe distributions co-localize to areas without GFP signal (white arrows). (b) Siderophore distributions in the heart expand outside of the abscess. (c) Zooms of a single kidney abscess show heterogeneity in siderophore and Fe distributions as well as Fe starvation, similar to distributions within the liver. Reprinted from Proceedings of the National Academy of Sciences, 2019, 201913991, “*Staphylococcus aureus* exhibits heterogeneous siderophore production within the vertebrate host” with permission from the National Academy of Sciences.¹⁴³

Discussion

Our results provide insight into mechanisms of staphylococcal metal acquisition within the infection environment and emphasize the capabilities of IMS to investigate host-microbe interactions. While it is well accepted that siderophores play a role in pathogenesis, the functionality of the molecular structures appears redundant. Furthermore, specific infectious niches in which siderophores are employed have yet to be discovered. Previous *in vitro* research has determined factors that regulate biosynthesis of staphyloferrin A and staphyloferrin B independently.^{165, 172} Glucose represses production of staphyloferrin A, and heme acts as a regulator of staphyloferrin B production.^{172, 173} Indeed, staphyloferrin A and B differentially impact the outcome of infection in various murine models, but the contribution of each siderophore within specific infectious niches is unknown.^{79, 165, 171, 172} It is possible that each siderophore evolved for a specific purpose, prompting redundancy in Fe acquisition mechanisms specific for various niches. Heterogeneity in the spatial distributions of staphylococcal siderophores could therefore be explained by variations in the molecular contents of an abscess. Use of spatial molecular technologies such as MALDI IMS will assist in the understanding of conditions or environments under which siderophores are expressed to elucidate their purposes. Furthermore, these spatial molecular techniques allow multi-modality integration to visualize distributions of host and bacterial factors as well as metals. Because tags or probes are not necessary, these data can guide future studies to elucidate molecular host-pathogen interactions. Visualization and chemical insight into the production of siderophores from any bacterial species within a host environment will help to understand mechanisms of metal acquisition and ultimately pathogenesis. We envision application of siderophore spatial analysis to other bacterial pathogens as well as microbe-microbe interactions under nutrient stress, specifically in complex environments such as

the gut microbiome or polymicrobial infections, as well as transitional applications towards infection diagnostics.

Methods

Bacterial Strains and Growth Conditions

The *S. aureus* clinical osteomyelitis isolate strain Newman served as the genetic background for all experiments.¹⁵⁵ The construction of *S. aureus* strain Newman *P_{isd}Agfp* has previously been described.¹³ The strain inactivated for staphyloferrin A production (Δ *sfa*) has previously been described.¹⁷¹ Bacteria were routinely cultured at 37°C in Difco TSB or on TSA. When required to select for mutants or maintain plasmids, antibiotics were added at the following concentrations: kanamycin 30 µg/mL or chloramphenicol 10 µg/mL.

Animal Procedures

In preparation for murine infections, bacteria were streaked from freezer culture on TSA with antibiotics, as required. Isolated colonies were used to prepare overnight cultures in 5 mL TSB. After overnight growth, bacteria were sub-cultured 1:100 in fresh TSB and grown until mid-to-late log phase (2-3 h; OD_{600nm} ~2-2.5). Cells were pelleted by centrifugation at 7,000 rpm for 6 min and washed thrice with phosphate buffered saline (PBS). After the final wash, cells were resuspended to an OD_{600nm} of approximately 0.4 in PBS (~1-2 x 10⁸ colony forming units (CFU)/mL). The inoculum was determined by serial dilution in PBS and plating to TSA.

Prior to infection, female 6-8 week old BALB/c mice, purchased from The Jackson Laboratory, were anesthetized by intraperitoneal injection with 125–250 mg/kg of 2,2,2-

tribromoethanol. Mice were infected retro-orbitally with 100 μL of the prepared staphylococcal cells ($\sim 1\text{-}2 \times 10^7$ CFU). At 4, 7, or 10 days post infection mice were humanely euthanized by carbon dioxide inhalation. The kidney, hearts and livers were harvested and immediately frozen on a bed of dry ice. Tissues were stored at -80°C until needed. Animals were used and handled in accordance with protocols approved by the Vanderbilt University Institutional Animal Care and Use Committee and are in compliance with National Institute of Health guidelines, the Animal Welfare Act, and US Federal law.

Materials and Sample Preparations

1,8-bis(tetramethylguanidino)naphthalene (TMGN), hematoxylin, and eosin were purchased from Sigma Aldrich (St. Louis, MO, USA). 3,4-diaminobenzophenone (DABP), and 1,5-diaminonaphthalene (DAN, 97%) were also purchased from Sigma Aldrich (St. Louis, MO, USA) then purified by recrystallization. The gold sputtering target was purchased from Ted Pella Inc. (Redding, CA, USA). ITO coated slides were purchased from Delta Technologies, Limited (Loveland, CO, USA). Vinyl slides were purchased from Electron Microscopy Sciences (Hatfield, PA, USA). Carbonate buffer, sodium salts, all solvents (methanol, ethanol, acetonitrile, and xylenes), glass microscope slides, and optimal cutting temperature compound were purchased from Fisher Scientific (Kalamazoo, MI, USA).

Fresh frozen tissues were serially sectioned at 10 μm using a Leica CM3050s cryostat (Leica Biosystems, Buffalo Grove, IL, USA) and thaw mounted on glass microscope slides (Fisher Scientific, Kalamazoo, MI, USA), ITO coated glass slides (Delta Technologies, Loveland, CO, USA), and vinyl slides (Electron Microscopy Sciences, Hatfield, PA, USA). Sections on ITO coated slides and vinyl slides were stored at -80°C until analysis where they were thawed under

vacuum at room temperature for approximately 15 minutes. MALDI matrix was applied using a robotic aerosol sprayer (TM Sprayer, HTX Technologies, Chapel Hill, NC, USA) with optimized conditions (75/25 DABP/TMGN in a solution of 70% acetonitrile sprayed at a surface density of 1.91 $\mu\text{g}/\text{mm}^2$ at 40°C; DAN in a solution of 90% acetonitrile sprayed at a surface density of 3.6 $\mu\text{g}/\text{mm}^2$ at 85°C; 1:1 ratio of carbonate buffer (pH 10.3) and 250 mM sodium acetate in a solution of 30% methanol sprayed at a surface density of 6.8 $\mu\text{g}/\text{mm}^2$ at 85°C). Samples coated with layers of metal were created using a Cressington 208HR sputter coater from de Ted Pella Inc. (Redding, CA, USA) at an Ar partial pressure of 0.02 mbar and a current of 40 mA. The depositions were time controlled. Samples sprayed with a salt solution were covered a 26 nm layer of gold. Other samples were covered in a 10 nm layer of silver. Serial sections on glass slides were stained with hematoxylin and eosin (Fisher Scientific, Kalamazoo, MI, USA). Bright field images of stained sections were acquired using a Leica SCN-400 optical slide scanner (Leica Biosystems, Buffalo Grove, IL, USA) at 20X magnification (0.5 $\mu\text{m}/\text{pixel}$).

Fluorescence Microscopy Image Acquisition and Data Analysis

Fluorescence microscopy images were acquired from tissue sections 10 DPI on ITO coated slides before matrix application using a fluorescence microscope (Nikon Eclipse 90i, Nikon Instruments Inc., Melville, NY, USA) equipped with a motorized stage and a 10X objective. Resulting pixel resolutions were 0.92 $\mu\text{m}/\text{pixel}$. A FITC (excitation = 465–495, emission = 515–555) specific epifluorescence filter was used to visualize the GFP reporter at an exposure time of 40 ms. DAPI (excitation = 340–380, emission = 435–485) and TRITC (excitation = 528–553, emission = 590–650) specific epifluorescence filters were used to allow visualization of tissue morphology by autofluorescence at exposure times of 100 ms and 150 ms, respectively.

Molecular Image Acquisition and Data Analysis

All experiments were performed using a 15T FT-ICR MS (SolariX, Bruker Daltonics, Billerica, MA, USA) equipped with an Apollo II dual MALDI/ESI source and a dynamically harmonized ParaCell (Bruker Daltonics, Billerica, MA, USA). The MALDI source employs a Smartbeam II 2 kHz, frequency tripled Nd:YAG (355 nm) laser. Molecular images were acquired at pixel spacings of 60 or 35 μm in both the x and y directions using a $\sim 50\text{-}\mu\text{m}$ laser beam size (750 laser shots). Data were collected from m/z 300 to 600 in negative ionization mode with a resolving power ($m/\Delta m$) of $\sim 175,000$ at m/z 500. The time domain file size was set to 512k (free induction decay: 0.46 s). The ion optics were tuned to maximize transmission at the defined m/z range including the funnel radio frequency amplitude (185 Vpp), source octopole (5 MHz, 350 Vpp), collision cell (collision cell voltage: 1.5 V, cell: 2 MHz, 1200 Vpp), time-of-flight delay (0.65 ms), transfer optics (4 MHz, 380 Vpp), and quadrupole using the continuous accumulation selected ions feature (Q1 mass: m/z 470, isolation window: m/z 125). The source DC optics were kept constant for all experiments (capillary exit -220 V, deflector plate: -200 V, plate offset: -100 V, funnel 1: -150 V, skimmer 1: -15 V) as well as the ICR cell parameters (transfer exit lens: 20 V, analyzer exit: 10 V, side kick: 8 V, front and back trap plates: -1.5 V, back trap plate quench: 30 V, shimming DC bias: -1.5 V, and gated injection DC bias: -1.5 V). Ion detection was performed using a sweep excitation power of 18%. FlexImaging 5.0 (Bruker Daltonics, Billerica, MA, USA) and SCiLS Lab (version 2016b, Bruker Daltonics, Billerica, MA, USA) were used to visualize ion images.

Elemental Image Acquisition and Data Analysis

Elemental Fe imaging was performed as previously described.¹³ Briefly, samples were ablated using a laser ablation system (LSX-213, Teledyne CETAC, Omaha, NE, USA) and analyzed using a high-resolution sector field ICP-MS (Element 2, Thermo Fisher Scientific, Bremen, Germany). Samples were placed into a sealed chamber and ablated in continuous raster mode using a quintupled Nd:YAG (213 nm) laser at a frequency of 5 Hz for all acquired data. Resulting data contained Y-axis pixel sizes of 35 or 60 μm . X-axis pixel sizes were determined by the stage velocity and the instrumental scan rate. Helium gas was used at a flow rate of 1 liter/min to transport ablated sample particles from the ablation chamber to the ICP source. The ICP torch position and Ar flow rate were tuned for each sample to obtain optimum signal with an SRM 612 standard from the National Institute of Standards and Technology. The mass spectrometer was operated in medium-resolution mode providing a reported resolving power of ~ 4300 at m/z 56. Elemental data were converted into the imzML format using Cardinal in the open source R environment and imported into SCiLS (version 2019b, Bruker Daltonics, Billerica, MA, USA) for image generation and visualization.¹⁷⁴

CHAPTER V

CONSPECTUS

Overview

Molecular imaging approaches in tandem with anatomical, morphological, or elemental imaging modalities allow for increased information from a tissue sample, furthering insight to complex biological systems. Workflows were developed, characterized, and implemented in combination with microscopy-based techniques to advance IMS investigations of *Staphylococcus aureus* pathogenic adaptations within infections. First, lipid observations from several MALDI matrices were compared in Chapter II to characterize how a specific sample preparation, including the chosen MALDI matrix, influences resultant ions. Research in Chapter III isolated m/z values co-localizing with fluorescent bacterial foci to ultimately identify and map *S. aureus* lysyl-PG lipids from a murine infection model. CAMPs, known to influence *S. aureus* lysyl-PG production, and lysyl-PGs were then mapped across human endocarditis tissue. Several surfaces coatings were compared in Chapter IV to ultimately visualize *S. aureus* siderophores within tissue infections. This research was complemented by LA-ICP IMS to map elemental Fe from sites of infection and fluorescence microscopy to map *S. aureus* Fe starvation. In this conspectus, current applications of MALDI IMS as it related to sample preparations and infectious disease will be discussed.

MALDI Matrix Influence on Analyte Observation

Utilizing a matrix, MALDI facilitates the desorption and ionization of analytes. Currently, a universal MALDI matrix does not exist. The method of sample preparation including the MALDI matrix choice influences the specific analytes observed. The number of chemicals reported to serve as MALDI matrices for a singular class of analytes (*i.e.* metabolites or lipids) is ever increasing.^{118,}
¹⁷⁵ However, little research characterizes or differentiates MALDI matrices reported to serve for the same analyte class.^{122, 132, 175, 176} Due to the complex makeup of tissue, it can be expected that many analytes go undetected when analyzed by MALDI MS. This is furthered by research determining that MALDI using conventional, organic matrices results in ionization efficiencies, reported as ion-to-neutral ratios, ranging from 10^{-3} to 10^{-8} , dependent on the analyte of interest.^{177,}
¹⁷⁸ Furthermore, ionization efficiencies for the same analyte vary when different MALDI matrices are employed.¹⁷⁹ Thus, it is likely that a very small percentage of analytes within a tissue section are ionized and detected, potentially biased due a chosen MALDI matrix. To move the field forward, implicit biases associated with MALDI matrices must be determined.

In Chapter II, work was done to characterize observed lipids signals as a result of a MALDI matrix. A series of MALDI matrices (DHA, DAN, CMBT, DHB, and 9AA) were employed to compare the observed lipid species when analyzed by MALDI IMS. Trends were determined from differentially abundant lipid signals in IMS datasets. Assessment by ROC analyses of commonly used MALDI matrices showed distinctive differences in the frequency and abundance of many lipid classes. Differences observed in positive ionization mode data related to ion types. Further work determined that MALDI matrix application via a robotic aerosol sprayer resulted in higher numbers of cationized species during positive ionization mode analysis when compared to matrix application by sublimation or tissue washing followed by sublimation for DHA matrix. For

negative ionization mode data, DAN matrix resulted in an observed higher sensitivity for many lipid species including phosphatidylethanolamines. This observed higher phosphatidylethanolamine sensitivity was, attributed to the loss of a methyl group from the choline head groups of phosphatidylcholine lipids, resulting in accurate mass assignments isobaric to phosphatidylethanolamine lipids. While this assessment of common lipid matrices identified many sensitivity trends for lipid sub-classes, a plethora of chemicals are being employed as MALDI matrices. As such, it can be expected that no universal MALDI matrix will be identified. Rather, analytes from tissues will show differential abundances based on a matrix, and an experimental goal should be defined before choosing a MALDI matrix.

Multimodal Imaging Approaches to Investigate Bacterial Pathogenesis

MALDI MS has made a positive impact on the field of infectious disease, offering microbial identification after isolation, culture, and spectral comparison to a database.¹⁸⁰ While this approach assists in diagnosis, it does not allow for study of microbes in an infection environment or host-pathogen interactions. Techniques like IHC can map bacterial proteins of interest within a tissue section; however, it does not accommodate metabolites and requires *a priori* knowledge for labels or tags. All molecules critical for bacterial proliferation or host defense *in vivo* are not known. Thus, application of untargeted, molecular approaches like MALDI IMS can expand our knowledge of host defense mechanisms and bacterial pathogenesis. The few studies that have employed this technology to investigate the infectious interface have identified an abundance of molecular constituents, of both host and pathogen origin, that construct as well as interact within these foci.^{13, 87, 88, 143, 145, 181-183} It is inevitable that as MALDI IMS further improves, this technology will drive more biological studies and provide increased information about host-

pathogen interactions. One example is the implementation of high-performance instrumentation such as FT-ICR MS. These instruments can allow for the highest levels of sensitivity from a single ion generation event.^{87, 184} Chapter II highlights the differential observation of chemical species resulting from a specific MALDI matrix. Combining these concepts, FT-ICR IMS and a specific MALDI matrix or surface coating can allow for increased study of bacteria-specific molecules from sites of infection.

Despite advances in imaging technologies, there is no universal technique to capture molecular and morphological information in a single experiment. Multiple co-registered or computationally fused imaging modalities can provide new information about a tissue's surface. We leveraged data mining image fusion of high-performance MALDI FT-ICR IMS and fluorescence micrographs of transcriptional bacterial reporters in Chapter III to investigate the presence and distribution of *S. aureus* lysyl-PG lipids within soft tissue infections. Image fusion of the modalities isolated molecular species co-localized with SACs. Distributions of lysyl-PGs from a murine infection model were not present at all SACs, and lysyl-PG distributions from a human endocarditis tissue sample showed the heterogeneous presence with *S. aureus* phosphatidylglycerols. These observations suggest differential staphylococcal molecular responses to host stressors or mechanisms of innate immunity, potentially relating to overall pathogenicity. Distributions of α -Defensin 1 and α -Defensin 2 CAMPs, a host mechanism used to combat gram-positive infections, localize to diseased tissue and are absent from normal valve tissue. However, increased presence of lysyl-PGs localizes near the normal valve tissue. Presence of the lipids at that location as well as the lack of CAMPs could be due to bacterial evasion of the innate immune system.

Bacteria have evolved multiple mechanisms to allow proliferation within a vertebrate host, including the use of small molecule chelators termed siderophores. *S. aureus* utilizes multiple siderophores for Fe acquisition, and the production of these molecules is required for maximum virulence in a vertebrate host. However, these molecules have not been observed in previous IMS experiments by our laboratories. Multiple surface coatings were employed in Chapter IV to ultimately observe staphyloferrin A and staphyloferrin B siderophores from sites of *S. aureus* infection using TMGN and DABP as MALDI matrices. Continuing this investigation of siderophores, infected tissues were sectioned serially for H&E staining, molecular analysis using MALDI IMS, and elemental Fe analysis using LA-ICP IMS. Large differences in siderophore production were observed from one abscess to another. Fe was largely excluded from sites of infection, but some pixels within an elemental Fe image showed co-localization of the metal to SACs, presumably highlighting the success of these organisms at capturing Fe within infected tissue. Heterogeneity in the spatial distributions of the siderophores could be explained by variations in the molecular contents of an abscess. This is the first observation of siderophores from host tissues. Many investigations could use these methods to map these metal scavenging metabolites from infections by other pathogens or healthy commensal microbes.

Molecular Heterogeneity of *Staphylococcus aureus* Infections

Our laboratories have pioneered the use of IMS to investigate infections by *S. aureus*.^{11-13, 77, 87, 88, 143, 185, 186} As IMS technology advances, more complex hypotheses can be answered. A common theme of the research within Chapters III and IV is the observed molecular heterogeneity within and across soft tissue abscesses, highlighting the potential for niche-specific *S. aureus* pathogenic strategies. While the *in vitro* roles of siderophores, lysyl-PGs, and other various

pathogenic adaptations are known, it is not clear when and where these adaptations are most important during infection. Molecular heterogeneity across infectious foci may be explained by differential responses or mechanisms of host-pathogen interactions. Organ-specific responses to infection may also exist. Increased understanding of when and where these pathogenic adaptations are required for bacterial proliferation can drive the search for alternative, novel therapeutics. For example, a new commercial therapeutic to combat multi-drug resistant gram-negative pathogens utilizes a siderophore-antibiotic conjugate. Spatial molecular technologies such as MALDI IMS will assist in relating molecular heterogeneity to conditions, environments, or other, previously uncharacterized, molecular distributions to further elucidate host-pathogen interactions.

Future Directions: Applications of Integrating Multiple 3-Dimensional Molecular Imaging

Modalities

Biological systems inherently occupy 3D spaces. Therefore, the fields of molecular and elemental imaging have witnessed a trend towards investigations attempting to axially resolve analyte distributions. Because many elemental and molecular imaging experiments are inherently 2D, most approaches require sectioning and analysis of many serial tissue sections to generate 3D data. This strategy presents several challenges, including sequential image registration from tissue that can be damaged during sectioning, large data files from combining many multimodal 2D imaging experiments into a single 3D volume, and finally, computational demands required for 3D data volume reconstruction and mining.¹⁸⁷ Nevertheless, several studies have overcome these challenges to build 3D multimodal molecular images.

To entirely circumvent the need for tissue sectioning, Ghosal *et al.* used ablation depths generated by nanoSIMS to acquire 3D volumes of spores.¹⁸⁸ However, calculating the depth from

SIMS ablation is challenging due to sample density variations. To address this challenge, Moreno *et al.* implemented depth probing and monitoring by atomic force microscopy to allow for more accurate 3D analysis.¹⁸⁹ While this strategy is successful for smaller objects, visualization of analytes within large structures typically requires data to be collected from multiple tissue planes.

In an early example of 3D metal imaging, Hare *et al.* performed LA-ICP IMS on 46 tissue slices of murine brains. Subsequently, 3D modeling was performed based on alignment of common morphological features. Although not strictly multimodal, this approach was an important step towards evaluating metal distribution throughout complex tissues.¹⁹⁰

To investigate multi-organism systems in 3D, Cassat *et al.* used iterative blockface imaging in combination with MRI, 3D BLI, and IMS to create a 3D model of *S. aureus* infected murine tissues (Figure 5.1A). As previously discussed, *in vivo* MRI and BLI measurements allowed the creation of 3D volumes that depict anatomical, elemental, and molecular changes resulting from staphylococcal infection and host nutritional immunity.¹³

Modern imaging technologies allow for small animals to be visualized in their entirety. Using computational tomography guided slice registration, Van Malderen and colleagues combined absorption microcomputed tomography (μ CT), 3D confocal μ XFI, and LA-ICP IMS to create 3D volumes of the metal distribution throughout the entire *Ceriodaphnia dubia* (water flea) body (Figure 5.1B).¹⁹¹

Most current 3D approaches rely on the sectioning of biological material. While various microtome technologies are commercially available, the sectioning of hard or brittle material remains challenging. To analyze the metal content of wheat and rye seeds, specimens were epoxy-embedded, stepwise polished to achieve lateral increments of 350 μ M, and analyzed via LA-ICP IMS and complementary XFI. 3D volumes were generated by feature-based registration and

compared to μ CT renderings (Figure 5.1C).¹⁹² The studies above exemplify multimodal investigations of molecular and elemental analytes while preserving spatial fidelity. Three-dimensionality is achieved by creative application of various sectioning and depth-probing methods as well as registration strategies in order to reflect the true spatial properties of biological samples.

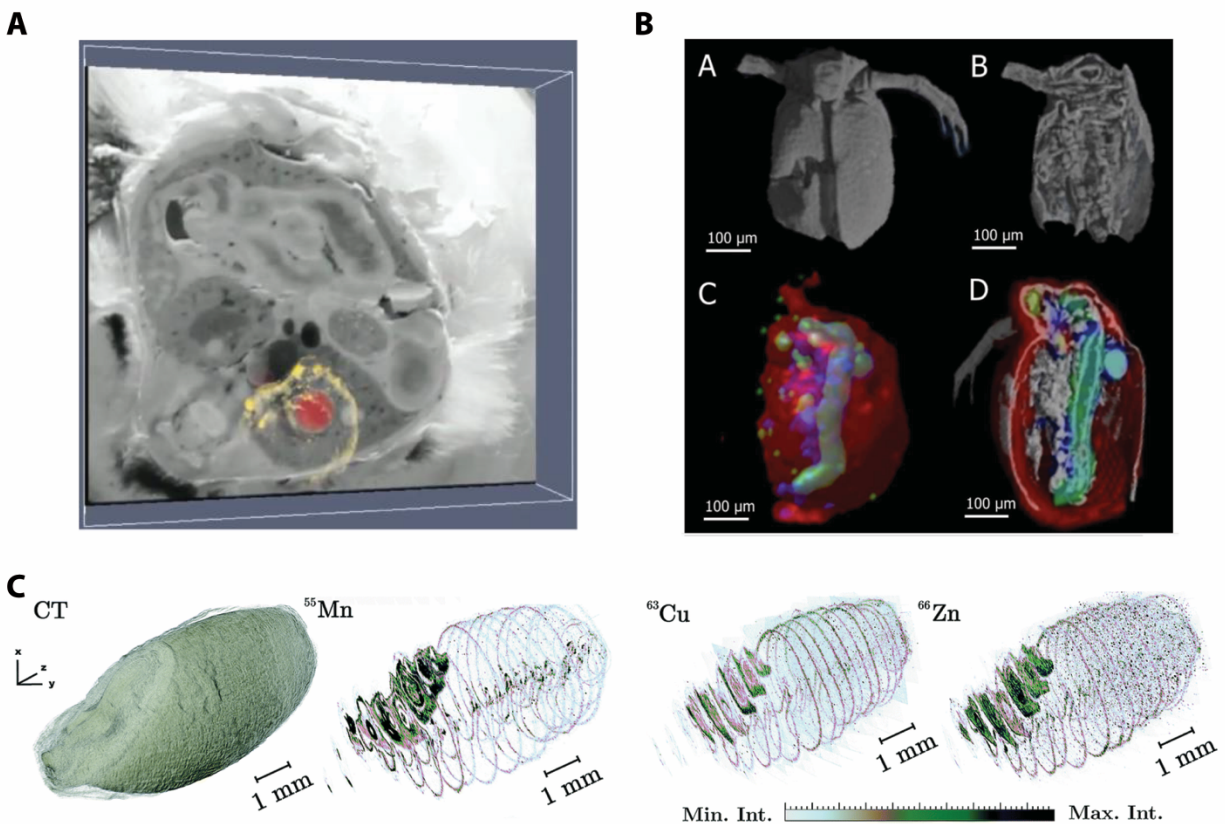


Figure 5.1: Overview of Recent Studies Employing Elemental Imaging in 3D

(A) Multimodal imaging of a murine kidney infected with *S. aureus*. Fe distribution (yellow, determined by LA-ICP IMS) and bacterial Fe-starvation dependent reporter activity (red sphere, assessed by BLI) are co-registered to blockface images. This image depicts one representative view of an entire 3D volume. Adapted from Cassat *et al.*¹³ (B) μCT 3D renderings of *C. dubia* (a-b) and distribution of selected elements (calcium: red, manganese: green, zinc: blue) as determined by μXRF (c-d). (C) μCT 3D image of *Triticum aestivum*. L. grain and elemental distribution throughout the sample as determined by LA-ICP MS. Adapted from Van Malderen *et al.*¹⁹² Reprinted from Current Opinion in Chemical Biology, 2020, 55, 127- 135, “Integrated molecular imaging technologies for investigation of metals in biological systems: a brief review” with permission from Elsevier.¹

Concluding Remarks

Since the conception of MALDI IMS, instrumentation that allows for this technology is constantly improving. Commercially available, next generation IMS platforms now allow for pixel sizes approaching cellular resolution ($\sim 10\ \mu\text{m}$), with limited decreases in instrumental sensitivities.¹⁹³ While many limitations still exist within IMS, such as protein identification strategies and MALDI matrix interferences, use of high-performance mass analyzers and gas-

phase separation techniques will increase instrumental capabilities.^{87, 146, 148, 184, 194} Because of increased IMS platform availability, an increasing number of complex disease states will be molecularly characterized. Capitalizing on the molecular information that IMS can provide, many multimodal studies now combine biomedical imaging modalities such as MRI and CT with IMS.^{1, 13, 191} As utilization of multimodal information becomes necessary to answer ever evolving, complex hypotheses, it is inevitable that computational tools will be further developed and implemented to address the new challenges provided by the instrumental capabilities.^{95, 96, 107}

REFERENCES

1. Perry, W. J.; Weiss, A.; Van de Plas, R.; Spraggins, J. M.; Caprioli, R. M.; Skaar, E. P., Integrated molecular imaging technologies for investigation of metals in biological systems: A brief review. *Current Opinion in Chemical Biology* **2020**, *55*, 127-135.
2. McMillen, J. C.; Perry, W. J.; Sharman, K.; Djambazova, K. D.; Caprioli, R. M., Matrix-assisted laser desorption/ionization imaging mass spectrometry: technology and applications. In *Toxic Chemical and Biological Agents*, Sindona, G.; Banoub, J. H.; Di Gioia, M. L., Eds. Springer Netherlands: 2020.
3. McRae, R.; Bagchi, P.; Sumalekshmy, S.; Fahrni, C. J., In situ imaging of metals in cells and tissues. *Chemical reviews* **2009**, *109* (10), 4780-4827.
4. Buchwalow, I. B. B., Werner, Immunohistochemistry: Basics and Methods. Springer, Berlin, Heidelberg: 2010.
5. Giesen, C.; Wang, H. A. O.; Schapiro, D.; Zivanovic, N.; Jacobs, A.; Hattendorf, B.; Schüffler, P. J.; Grolimund, D.; Buhmann, J. M.; Brandt, S.; Varga, Z.; Wild, P. J.; Günther, D.; Bodenmiller, B., Highly multiplexed imaging of tumor tissues with subcellular resolution by mass cytometry. *Nature Methods* **2014**, *11*, 417.
6. Baker, M. J.; Trevisan, J.; Bassan, P.; Bhargava, R.; Butler, H. J.; Dorling, K. M.; Fielden, P. R.; Fogarty, S. W.; Fullwood, N. J.; Heys, K. A.; Hughes, C.; Lasch, P.; Martin-Hirsch, P. L.; Obinaju, B.; Sockalingum, G. D.; Sulé-Suso, J.; Strong, R. J.; Walsh, M. J.; Wood, B. R.; Gardner, P.; Martin, F. L., Using Fourier transform IR spectroscopy to analyze biological materials. *Nat Protoc* **2014**, *9* (8), 1771-1791.
7. Porta Siegel, T.; Hamm, G.; Bunch, J.; Cappell, J.; Fletcher, J. S.; Schwamborn, K., Mass Spectrometry Imaging and Integration with Other Imaging Modalities for Greater Molecular Understanding of Biological Tissues. *Molecular Imaging and Biology* **2018**, *20* (6), 888-901.
8. Schwamborn, K.; Caprioli, R. M., MALDI Imaging Mass Spectrometry – Painting Molecular Pictures. *Molecular Oncology* **2010**, *4* (6), 529-538.
9. Hillenkamp, F.; Karas, M.; Beavis, R. C.; Chait, B. T., Matrix-Assisted Laser Desorption/Ionization Mass Spectrometry of Biopolymers. *Analytical Chemistry* **1991**, *63* (24), 1193A-1203A.
10. Holzlechner, M.; Bonta, M.; Lohninger, H.; Limbeck, A.; Marchetti-Deschmann, M., Multisensor Imaging—From Sample Preparation to Integrated Multimodal Interpretation of LA-ICPMS and MALDI MS Imaging Data. *Analytical Chemistry* **2018**, *90* (15), 8831-8837.
11. Juttukonda, L. J.; Berends, E. T. M.; Zackular, J. P.; Moore, J. L.; Stier, M. T.; Zhang, Y.; Schmitz, J. E.; Beavers, W. N.; Wijers, C. D.; Gilston, B. A.; Kehl-Fie, T. E.; Atkinson, J.; Washington, M. K.; Peebles, R. S.; Chazin, W. J.; Torres, V. J.; Caprioli, R. M.; Skaar, E. P., Dietary Manganese Promotes Staphylococcal Infection of the Heart. *Cell Host & Microbe* **22** (4), 531-542.e8.
12. Kehl-Fie, T. E.; Zhang, Y.; Moore, J. L.; Farrand, A. J.; Hood, M. I.; Rathi, S.; Chazin, W. J.; Caprioli, R. M.; Skaar, E. P., MntABC and MntH Contribute to Systemic *Staphylococcus aureus* Infection by Competing with Calprotectin for Nutrient Manganese. *Infection and Immunity* **2013**, *81* (9), 3395-3405.
13. Cassat, J. E.; Moore, J. L.; Wilson, K. J.; Stark, Z.; Prentice, B. M.; Van de Plas, R.; Perry, W. J.; Zhang, Y.; Virostko, J.; Colvin, D. C.; Rose, K. L.; Judd, A. M.; Reyzer, M. L.; Spraggins, J. M.; Grunewald, C. M.; Gore, J. C.; Caprioli, R. M.; Skaar, E. P., Integrated

molecular imaging reveals tissue heterogeneity driving host-pathogen interactions. *Science Translational Medicine* **2018**, *10* (432).

14. Caprioli, R. M.; Farmer, T. B.; Gile, J., Molecular Imaging of Biological Samples: Localization of Peptides and Proteins Using MALDI-TOF MS. *Analytical Chemistry* **1997**, *69* (23), 4751-4760.

15. Wiley, W. C.; McLaren, I. H., Time-of-Flight Mass Spectrometer with Improved Resolution. *Review of Scientific Instruments* **1955**, *26* (12), 1150-1157.

16. Spraggins, J. M.; Rizzo, D. G.; Moore, J. L.; Noto, M. J.; Skaar, E. P.; Caprioli, R. M., Next-generation technologies for spatial proteomics: Integrating ultra-high speed MALDI-TOF and high mass resolution MALDI FTICR imaging mass spectrometry for protein analysis. *PROTEOMICS* **2016**, *16* (11-12), 1678-1689.

17. Marshall, A. G.; Hendrickson, C. L.; Jackson, G. S., Fourier transform ion cyclotron resonance mass spectrometry: A primer. *Mass Spectrometry Reviews* **1998**, *17* (1), 1-35.

18. Thomas, A.; Charbonneau, J. L.; Fournaise, E.; Chaurand, P., Sublimation of New Matrix Candidates for High Spatial Resolution Imaging Mass Spectrometry of Lipids: Enhanced Information in Both Positive and Negative Polarities after 1,5-Diaminonaphthalene Deposition. *Analytical Chemistry* **2012**, *84* (4), 2048-2054.

19. Yang, J.; Caprioli, R. M., Matrix sublimation/recrystallization for imaging proteins by mass spectrometry at high spatial resolution. *Anal Chem* **2011**, *83* (14), 5728-34.

20. Fujino, Y.; Minamizaki, T.; Yoshioka, H.; Okada, M.; Yoshiko, Y., Imaging and mapping of mouse bone using MALDI-imaging mass spectrometry. *Bone Rep* **2016**, *5*, 280-285.

21. Judd, A. M.; Gutierrez, D. B.; Moore, J. L.; Patterson, N. H.; Yang, J.; Romer, C. E.; Norris, J. L.; Caprioli, R. M., A recommended and verified procedure for in situ tryptic digestion of formalin-fixed paraffin-embedded tissues for analysis by matrix-assisted laser desorption/ionization imaging mass spectrometry. *Journal of Mass Spectrometry* **2019**, *54* (8), 716-727.

22. Dufresne, M.; Patterson, N. H.; Norris, J. L.; Caprioli, R. M., Combining Salt Doping and Matrix Sublimation for High Spatial Resolution MALDI Imaging Mass Spectrometry of Neutral Lipids. *Analytical Chemistry* **2019**.

23. Drake, R. R.; Powers, T. W.; Norris-Caneda, K.; Mehta, A. S.; Angel, P. M., In Situ Imaging of N-Glycans by MALDI Imaging Mass Spectrometry of Fresh or Formalin-Fixed Paraffin-Embedded Tissue. *Current Protocols in Protein Science* **2018**, *94* (1), e68.

24. Powers, T. W.; Neely, B. A.; Shao, Y.; Tang, H.; Troyer, D. A.; Mehta, A. S.; Haab, B. B.; Drake, R. R., MALDI Imaging Mass Spectrometry Profiling of N-Glycans in Formalin-Fixed Paraffin Embedded Clinical Tissue Blocks and Tissue Microarrays. *PLOS ONE* **2014**, *9* (9), e106255.

25. Thomas, A.; Chaurand, P., Advances in tissue section preparation for MALDI imaging MS. *Bioanalysis* **2014**, *6* (7), 967-982.

26. Fowler, C. B.; O'Leary, T. J.; Mason, J. T., Toward improving the proteomic analysis of formalin-fixed, paraffin-embedded tissue. *Expert Review of Proteomics* **2013**, *10* (4), 389-400.

27. Paine, M. R. L.; Ellis, S. R.; Maloney, D.; Heeren, R. M. A.; Verhaert, P. D. E. M., Digestion-Free Analysis of Peptides from 30-year-old Formalin-Fixed, Paraffin-Embedded Tissue by Mass Spectrometry Imaging. *Analytical Chemistry* **2018**, *90* (15), 9272-9280.

28. Ly, A.; Buck, A.; Balluff, B.; Sun, N.; Gorzolka, K.; Feuchtinger, A.; Janssen, K.-P.; Kuppen, P. J. K.; van de Velde, C. J. H.; Weirich, G.; Erlmeier, F.; Langer, R.; Aubele, M.; Zitzelsberger, H.; McDonnell, L.; Aichler, M.; Walch, A., High-mass-resolution MALDI mass

spectrometry imaging of metabolites from formalin-fixed paraffin-embedded tissue. *Nat Protoc* **2016**, *11*, 1428.

29. Buck, A.; Ly, A.; Balluff, B.; Sun, N.; Gorzolka, K.; Feuchtinger, A.; Janssen, K.-P.; Kuppen, P. J.; van de Velde, C. J.; Weirich, G.; Erlmeier, F.; Langer, R.; Aubele, M.; Zitzelsberger, H.; Aichler, M.; Walch, A., High-resolution MALDI-FT-ICR MS imaging for the analysis of metabolites from formalin-fixed, paraffin-embedded clinical tissue samples. *The Journal of Pathology* **2015**, *237* (1), 123-132.

30. Angel, P. M.; Spraggins, J. M.; Baldwin, H. S.; Caprioli, R., Enhanced Sensitivity for High Spatial Resolution Lipid Analysis by Negative Ion Mode Matrix Assisted Laser Desorption Ionization Imaging Mass Spectrometry. *Analytical Chemistry* **2012**, *84* (3), 1557-1564.

31. Gill, E. L.; Yost, R. A.; Vedam-Mai, V.; Garrett, T. J., Precast Gelatin-Based Molds for Tissue Embedding Compatible with Mass Spectrometry Imaging. *Analytical chemistry* **2017**, *89* (1), 576-580.

32. Stoeckli, M.; Staab, D.; Schweitzer, A., Compound and metabolite distribution measured by MALDI mass spectrometric imaging in whole-body tissue sections. *International Journal of Mass Spectrometry* **2007**, *260* (2), 195-202.

33. Sun, G.; Yang, K.; Zhao, Z.; Guan, S.; Han, X.; Gross, R. W., Matrix-Assisted Laser Desorption/Ionization Time-of-Flight Mass Spectrometric Analysis of Cellular Glycerophospholipids Enabled by Multiplexed Solvent Dependent Analyte–Matrix Interactions. *Analytical Chemistry* **2008**, *80* (19), 7576-7585.

34. Yang, H.; Ji, W.; Guan, M.; Li, S.; Zhang, Y.; Zhao, Z.; Mao, L., Organic washes of tissue sections for comprehensive analysis of small molecule metabolites by MALDI MS imaging of rat brain following status epilepticus. *Metabolomics* **2018**, *14* (4), 50.

35. Grey, A. C.; Chaurand, P.; Caprioli, R. M.; Schey, K. L., MALDI Imaging Mass Spectrometry of Integral Membrane Proteins from Ocular Lens and Retinal Tissue. *Journal of Proteome Research* **2009**, *8* (7), 3278-3283.

36. Leinweber, B. D.; Tsaprailis, G.; Monks, T. J.; Lau, S. S., Improved MALDI-TOF imaging yields increased protein signals at high molecular mass. *Journal of the American Society for Mass Spectrometry* **2009**, *20* (1), 89-95.

37. Franck, J.; Longuespée, R.; Wisztorski, M.; Van Remoortere, A.; Van Zeijl, R.; Deelder, A.; Salzet, M.; McDonnell, L.; Fournier, I., MALDI mass spectrometry imaging of proteins exceeding 30,000 daltons. *Medical Science Monitor: International Medical Journal of Experimental and Clinical Research* **2010**, *16* (9), BR293-9.

38. Seeley, E. H.; Oppenheimer, S. R.; Mi, D.; Chaurand, P.; Caprioli, R. M., Enhancement of Protein Sensitivity for MALDI Imaging Mass Spectrometry after Chemical Treatment of Tissue Sections. *Journal of the American Society for Mass Spectrometry* **2008**, *19* (8), 1069-1077.

39. Källback, P.; Shariatgorji, M.; Nilsson, A.; Andrén, P. E., Novel mass spectrometry imaging software assisting labeled normalization and quantitation of drugs and neuropeptides directly in tissue sections. *Journal of Proteomics* **2012**, *75* (16), 4941-4951.

40. Zavalin, A.; Yang, J.; Hayden, K.; Vestal, M.; Caprioli, R. M., Tissue protein imaging at 1 μ m laser spot diameter for high spatial resolution and high imaging speed using transmission geometry MALDI TOF MS. *Analytical and Bioanalytical Chemistry* **2015**, *407* (8), 2337-2342.

41. Yang, J.; Norris, J. L.; Caprioli, R., Novel vacuum stable ketone-based matrices for high spatial resolution MALDI imaging mass spectrometry. *Journal of Mass Spectrometry* **0** (0).

42. Ulmer, L.; Mattay, J.; Torres-Garcia, H. G.; Luftmann, H., Letter: The Use of 2-[(2E)-3-(4-Tert-Butylphenyl)-2-Methylprop-2-Enylidene]Malononitrile as a Matrix for Matrix-Assisted

Laser Desorption/Ionization Mass Spectrometry. *European Journal of Mass Spectrometry* **2000**, 6 (1), 49-52.

43. Stübiger, G.; Belgacem, O., Analysis of Lipids Using 2,4,6-Trihydroxyacetophenone as a Matrix for MALDI Mass Spectrometry. *Analytical Chemistry* **2007**, 79 (8), 3206-3213.

44. Beavis, R. C.; Chaudhary, T.; Chait, B. T., Alpha-cyano-4-hydroxycinnamic acid as a matrix for matrix-assisted laser desorption mass spectrometry. *Org. Mass Spectrom.* **1992**, 27 (2), 156-158.

45. Strupat, K.; Karas, M.; Hillenkamp, F., 2,5-Dihydroxybenzoic acid - a new matrix for laser desorption ionization mass spectrometry. *Int. J. Mass Spectrom. Ion Process.* **1991**, 111, 89-102.

46. Xu, N. X.; Huang, Z. H.; Watson, J. T.; Gage, D. A., Mercaptobenzothiazoles: A new class of matrices for laser desorption ionization mass spectrometry. *Journal of the American Society for Mass Spectrometry* **1997**, 8 (2), 116-124.

47. Vermillion-Salsbury, R. L.; Hercules, D. M., 9-aminoacridine as a matrix for negative mode matrix-assisted laser desorption/ionization. *Rapid Communications in Mass Spectrometry* **2002**, 16 (16), 1575-1581.

48. Shi, C. Y.; Deng, C. H., Recent advances in inorganic materials for LDI-MS analysis of small molecules. *Analyst* **2016**, 141 (10), 2816-2826.

49. Schröter, J.; Fülöp, A.; Hopf, C.; Schiller, J., The combination of 2,5-dihydroxybenzoic acid and 2,5-dihydroxyacetophenone matrices for unequivocal assignment of phosphatidylethanolamine species in complex mixtures. *Analytical and Bioanalytical Chemistry* **2018**, 410 (9), 2437-2447.

50. Groseclose, M. R.; Castellino, S., A Mimetic Tissue Model for the Quantification of Drug Distributions by MALDI Imaging Mass Spectrometry. *Analytical Chemistry* **2013**, 85 (21), 10099-10106.

51. Fuchs, B.; Bischoff, A.; Süß, R.; Teuber, K.; Schürenberg, M.; Suckau, D.; Schiller, J., Phosphatidylcholines and -ethanolamines can be easily mistaken in phospholipid mixtures: a negative ion MALDI-TOF MS study with 9-aminoacridine as matrix and egg yolk as selected example. *Analytical and Bioanalytical Chemistry* **2009**, 395 (8), 2479.

52. Eriksson, C.; Masaki, N.; Yao, I.; Hayasaka, T.; Setou, M., MALDI Imaging Mass Spectrometry-A Mini Review of Methods and Recent Developments. *Mass Spectrom (Tokyo)* **2013**, 2 (Spec Iss), S0022-S0022.

53. Hankin, J. A.; Barkley, R. M.; Murphy, R. C., Sublimation as a Method of Matrix Application for Mass Spectrometric Imaging. *Journal of the American Society for Mass Spectrometry* **2007**, 18 (9), 1646-1652.

54. Anderson, D. M. G.; Ablonczy, Z.; Koutalos, Y.; Spraggins, J.; Crouch, R. K.; Caprioli, R. M.; Schey, K. L., High Resolution MALDI Imaging Mass Spectrometry of Retinal Tissue Lipids. *Journal of The American Society for Mass Spectrometry* **2014**, 25 (8), 1394-1403.

55. Andreini, C.; Bertini, I.; Cavallaro, G.; Holliday, G. L.; Thornton, J. M., Metal ions in biological catalysis: from enzyme databases to general principles. *JBIC Journal of Biological Inorganic Chemistry* **2008**, 13 (8), 1205-1218.

56. Haraguchi, H., Metallomics as integrated biometal science. *Journal of Analytical Atomic Spectrometry* **2004**, 19 (1), 5-14.

57. Bourassa, M. W.; Miller, L. M., Metal imaging in neurodegenerative diseases. *Metallomics* **2012**, 4 (8), 721-738.

58. Gozzelino, R.; Arosio, P., Iron Homeostasis in Health and Disease. *Int J Mol Sci* **2016**, 17 (1), 130.

59. Little, P. J.; Bhattacharya, R.; Moreyra, A. E.; Korichneva, I. L., Zinc and cardiovascular disease. *Nutrition* **2010**, *26* (11), 1050-1057.
60. Wang, Y.; Yu, L.; Ding, J.; Chen, Y., Iron Metabolism in Cancer. *Int J Mol Sci* **2018**, *20* (1), 95.
61. Palmer, L. D.; Skaar, E. P., Transition Metals and Virulence in Bacteria. *Annual Review of Genetics* **2016**, *50* (1), 67-91.
62. Stewart, T. J., Across the spectrum: integrating multidimensional metal analytics for in situ metallomic imaging. *Metallomics* **2019**, *11* (1), 29-49.
63. Jenkins, R., History and Development of X-Ray Fluorescence Spectrometry. In *X-Ray Fluorescence Spectrometry, Volume 152, Second Edition*, Jenkins, R., Ed. John Wiley & Sons, Inc.: 2012.
64. Tsuji, K.; Matsuno, T.; Takimoto, Y.; Yamanashi, M.; Kometani, N.; Sasaki, Y. C.; Hasegawa, T.; Kato, S.; Yamada, T.; Shoji, T.; Kawahara, N., New developments of X-ray fluorescence imaging techniques in laboratory. *Spectrochimica Acta Part B: Atomic Spectroscopy* **2015**, *113*, 43-53.
65. Taylor, A.; Barlow, N.; Day, M. P.; Hill, S.; Martin, N.; Patriarca, M., Atomic Spectrometry Update: review of advances in the analysis of clinical and biological materials, foods and beverages. *Journal of Analytical Atomic Spectrometry* **2018**, *33* (3), 338-382.
66. Houk, R. S.; Fassel, V. A.; Flesch, G. D.; Svec, H. J.; Gray, A. L.; Taylor, C. E., Inductively coupled argon plasma as an ion source for mass spectrometric determination of trace elements. *Analytical Chemistry* **1980**, *52* (14), 2283-2289.
67. Kindness, A.; Sekaran, C. N.; Feldmann, J., Two-Dimensional Mapping of Copper and Zinc in Liver Sections by Laser Ablation–Inductively Coupled Plasma Mass Spectrometry. *Clinical Chemistry* **2003**, *49* (11), 1916-1923.
68. Gray, A. L., Solid sample introduction by laser ablation for inductively coupled plasma source mass spectrometry. *Analyst* **1985**, *110* (5), 551-556.
69. Agüi-Gonzalez, P.; Jähne, S.; Phan, N. T. N., SIMS imaging in neurobiology and cell biology. *Journal of Analytical Atomic Spectrometry* **2019**.
70. Fletcher, J. S., Latest applications of 3D ToF-SIMS bio-imaging. *Biointerphases* **2015**, *10* (1), 018902.
71. DeLeo, F. R.; Otto, M.; Kreiswirth, B. N.; Chambers, H. F., Community-associated methicillin-resistant *Staphylococcus aureus*. *The Lancet* **2010**, *375* (9725), 1557-1568.
72. Klevens, R.; Morrison, M. A.; Nadle, J.; et al., Invasive methicillin-resistant *Staphylococcus aureus* infections in the united states. *JAMA* **2007**, *298* (15), 1763-1771.
73. Graham, P. L.; Iii; Lin, S. X.; Larson, E. L., A u.s. population-based survey of *Staphylococcus aureus* colonization. *Annals of Internal Medicine* **2006**, *144* (5), 318-325.
74. Klevens, R. M.; Edwards, J. R.; Tenover, F. C.; McDonald, L. C.; Horan, T.; Gaynes, R., Changes in the Epidemiology of Methicillin-Resistant *Staphylococcus aureus* in Intensive Care Units in US Hospitals, 1992–2003. *Clinical Infectious Diseases* **2006**, *42* (3), 389-391.
75. Casadevall, A.; Pirofski, L.-a., Host-Pathogen Interactions: Basic Concepts of Microbial Commensalism, Colonization, Infection, and Disease. *Infection and Immunity* **2000**, *68* (12), 6511-6518.
76. Cheng, A. G.; DeDent, A. C.; Schneewind, O.; Missiakas, D., A play in four acts: *Staphylococcus aureus* abscess formation. *Trends in microbiology* **2011**, *19* (5), 225-232.
77. Moore, J. L.; Caprioli, R. M.; Skaar, E. P., Advanced mass spectrometry technologies for the study of microbial pathogenesis. *Current Opinion in Microbiology* **2014**, *19*, 45-51.

78. Dye, E. S.; Kapral, F. A., Characterization of a bactericidal lipid developing within staphylococcal abscesses. *Infection and Immunity* **1981**, *32* (1), 98-104.
79. Sheldon, J. R.; Heinrichs, D. E., Recent developments in understanding the iron acquisition strategies of gram positive pathogens. *FEMS Microbiology Reviews* **2015**, *39* (4), 592-630.
80. Peschel, A.; Jack, R. W.; Otto, M.; Collins, L. V.; Staubitz, P.; Nicholson, G.; Kalbacher, H.; Nieuwenhuizen, W. F.; Jung, G.; Tarkowski, A.; van Kessel, K. P. M.; van Strijp, J. A. G., *Staphylococcus aureus* Resistance to Human Defensins and Evasion of Neutrophil Killing via the Novel Virulence Factor Mprf Is Based on Modification of Membrane Lipids with Lysine. *The Journal of Experimental Medicine* **2001**, *193* (9), 1067-1076.
81. Weinberg, E. D., Iron and Susceptibility to Infectious Disease. *Science* **1974**, *184* (4140), 952-956.
82. Fink, S. L.; Campbell, S., Chapter 3 - Infection and Host Response. In *Molecular Pathology (Second Edition)*, Coleman, W. B.; Tsongalis, G. J., Eds. Academic Press: 2018; pp 45-69.
83. Fraunholz, M.; Sinha, B., Intracellular *Staphylococcus aureus*: Live-in and let die. *Frontiers in Cellular and Infection Microbiology* **2012**, *2*, 43.
84. Kobayashi, S. D.; Malachowa, N.; DeLeo, F. R., Pathogenesis of *Staphylococcus aureus* Abscesses. *The American Journal of Pathology* **2015**, *185* (6), 1518-1527.
85. Rigby, K. M.; DeLeo, F. R., Neutrophils in innate host defense against *Staphylococcus aureus* infections. *Seminars in Immunopathology* **2012**, *34* (2), 237-259.
86. Moore, J. L.; Caprioli, R. M.; Skaar, E. P., Advanced Mass Spectrometry Technologies for the Study of Microbial Pathogenesis. *Current opinion in microbiology* **2014**, *0*, 45-51.
87. Spraggins, J. M.; Rizzo, D. G.; Moore, J. L.; Rose, K. L.; Hammer, N. D.; Skaar, E. P.; Caprioli, R. M., MALDI FTICR IMS of Intact Proteins: Using Mass Accuracy to Link Protein Images with Proteomics Data. *Journal of The American Society for Mass Spectrometry* **2015**, *26* (6), 974-985.
88. Wakeman, C. A.; Moore, J. L.; Noto, M. J.; Zhang, Y.; Singleton, M. D.; Prentice, B. M.; Gilston, B. A.; Doster, R. S.; Gaddy, J. A.; Chazin, W. J.; Caprioli, R. M.; Skaar, E. P., The innate immune protein calprotectin promotes *Pseudomonas aeruginosa* and *Staphylococcus aureus* interaction. **2016**, *7*, 11951.
89. Kehl-Fie, T. E.; Skaar, E. P., Nutritional immunity beyond iron: a role for manganese and zinc. *Current Opinion in Chemical Biology* **2010**, *14* (2), 218-224.
90. Nakashige, T. G.; Zhang, B.; Krebs, C.; Nolan, E. M., Human calprotectin is an iron-sequestering host-defense protein. *Nature Chemical Biology* **2015**, *11*, 765.
91. Lichtman, J. W.; Conchello, J.-A., Fluorescence microscopy. *Nature Methods* **2005**, *2* (12), 910-919.
92. Renz, M., Fluorescence microscopy—A historical and technical perspective. *Cytometry Part A* **2013**, *83* (9), 767-779.
93. Jones, M. A.; Cho, S. H.; Patterson, N. H.; Van de Plas, R.; Spraggins, J. M.; Boothby, M. R.; Caprioli, R. M., Discovering new lipidomic features using cell type specific fluorophore expression to provide spatial and biological specificity in a multimodal workflow with MALDI Imaging Mass Spectrometry. *Analytical Chemistry* **2020**.
94. Patterson, N. H.; Tuck, M.; Van de Plas, R.; Caprioli, R. M., Advanced Registration and Analysis of MALDI Imaging Mass Spectrometry Measurements through Autofluorescence Microscopy. *Analytical Chemistry* **2018**.

95. Verbeeck, N.; Yang, J.; De Moor, B.; Caprioli, R. M.; Waelkens, E.; Van de Plas, R., Automated Anatomical Interpretation of Ion Distributions in Tissue: Linking Imaging Mass Spectrometry to Curated Atlases. *Analytical Chemistry* **2014**, *86* (18), 8974-8982.
96. Verbeeck, N.; Spraggins, J. M.; Murphy, M. J. M.; Wang, H.-d.; Deutch, A. Y.; Caprioli, R. M.; Van de Plas, R., Connecting imaging mass spectrometry and magnetic resonance imaging-based anatomical atlases for automated anatomical interpretation and differential analysis. *Biochimica et Biophysica Acta (BBA) - Proteins and Proteomics* **2017**, *1865* (7), 967-977.
97. Patterson, N. H.; Yang, E.; Kranjec, E.-A.; Chaurand, P., Co-registration and analysis of multiple imaging mass spectrometry datasets targeting different analytes. *Bioinformatics* **2018**, *bty780-bty780*.
98. Patterson, N. H.; Tuck, M.; Lewis, A.; Kaushansky, A.; Norris, J. L.; Van de Plas, R.; Caprioli, R. M., Next Generation Histology-Directed Imaging Mass Spectrometry Driven by Autofluorescence Microscopy. *Analytical Chemistry* **2018**, *90* (21), 12404-12413.
99. Svirikova, A.; Turyanskaya, A.; Perneckzy, L.; Streli, C.; Marchetti-Deschmann, M., Multimodal imaging of undecalcified tissue sections by MALDI MS and μ XRF. *Analyst* **2018**, *143* (11), 2587-2595.
100. Ackerman, C. M.; Weber, P. K.; Xiao, T.; Thai, B.; Kuo, T. J.; Zhang, E.; Pett-Ridge, J.; Chang, C. J., Multimodal LA-ICP-MS and nanoSIMS imaging enables copper mapping within photoreceptor megamitochondria in a zebrafish model of Menkes disease. *Metallomics* **2018**, *10* (3), 474-485.
101. Pushie, M. J.; Kelly, M. E.; Hackett, M. J., Direct label-free imaging of brain tissue using synchrotron light: a review of new spectroscopic tools for the modern neuroscientist. *Analyst* **2018**, *143* (16), 3761-3774.
102. Hackett, M. J.; Hollings, A.; Majimbi, M.; Brook, E.; Cochran, B.; Giles, C.; Lam, V.; Nesbit, M.; Rye, K.-A.; Mamo, J. C. L.; Takechi, R., Multimodal Imaging Analyses of Brain Hippocampal Formation Reveal Reduced Cu and Lipid Content and Increased Lactate Content in Non-Insulin-Dependent Diabetic Mice. *ACS Chemical Neuroscience* **2019**, *10* (5), 2533-2540.
103. Fimognari, N.; Hollings, A.; Lam, V.; Tidy, R. J.; Kewish, C. M.; Albrecht, M. A.; Takechi, R.; Mamo, J. C. L.; Hackett, M. J., Biospectroscopic Imaging Provides Evidence of Hippocampal Zn Deficiency and Decreased Lipid Unsaturation in an Accelerated Aging Mouse Model. *ACS Chemical Neuroscience* **2018**, *9* (11), 2774-2785.
104. Summers, K. L.; Fimognari, N.; Hollings, A.; Kiernan, M.; Lam, V.; Tidy, R. J.; Paterson, D.; Tobin, M. J.; Takechi, R.; George, G. N.; Pickering, I. J.; Mamo, J. C.; Harris, H. H.; Hackett, M. J., A Multimodal Spectroscopic Imaging Method To Characterize the Metal and Macromolecular Content of Proteinaceous Aggregates ("Amyloid Plaques"). *Biochemistry* **2017**, *56* (32), 4107-4116.
105. Williamson Michael, R.; Dietrich, K.; Hackett Mark, J.; Caine, S.; Nadeau Colby, A.; Aziz Jasmine, R.; Nichol, H.; Paterson Phyllis, G.; Colbourne, F., Rehabilitation Augments Hematoma Clearance and Attenuates Oxidative Injury and Ion Dyshomeostasis After Brain Hemorrhage. *Stroke* **2017**, *48* (1), 195-203.
106. Blum, R. S. L., Zheng, *Multi-Sensor Image Fusion and Its Applications*. CRC Press: 2005.
107. Van de Plas, R.; Yang, J.; Spraggins, J.; Caprioli, R. M., Fusion of mass spectrometry and microscopy: a multi-modality paradigm for molecular tissue mapping. *Nature methods* **2015**, *12* (4), 366-372.
108. Neumann, E. K.; Comi, T. J.; Spegazzini, N.; Mitchell, J. W.; Rubakhin, S. S.; Gillette, M. U.; Bhargava, R.; Sweedler, J. V., Multimodal Chemical Analysis of the Brain by High Mass

- Resolution Mass Spectrometry and Infrared Spectroscopic Imaging. *Analytical Chemistry* **2018**, *90* (19), 11572-11580.
109. Ryabchykov, O.; Popp, J.; Bocklitz, T., Fusion of MALDI Spectrometric Imaging and Raman Spectroscopic Data for the Analysis of Biological Samples. *Frontiers in Chemistry* **2018**, *6* (257).
110. Milillo, T.; Hard, R.; Yatzor, B.; Miller, M. E.; Gardella, J., Image fusion combining SEM and ToF-SIMS images. *Surface and Interface Analysis* **2015**, *47* (3), 371-376.
111. Perry, W. J.; Patterson, N. H.; Prentice, B. M.; Neumann, E. K.; Caprioli, R. M.; Spraggins, J. M., Uncovering Matrix Effects on Lipid Analyses in MALDI Imaging Mass Spectrometry Experiments. *Journal of Mass Spectrometry* *n/a* (n/a), e4491.
112. Caprioli, R. M., Imaging mass spectrometry: Molecular microscopy for enabling a new age of discovery. *Proteomics* **2014**, *14* (7-8), 807-809.
113. McDonnell, L. A.; Heeren, R. M. A., Imaging mass spectrometry. *Mass Spectrometry Reviews* **2007**, *26* (4), 606-643.
114. Wyatt, M. F.; Stein, B. K.; Brenton, A. G., Characterization of Various Analytes Using Matrix-Assisted Laser Desorption/Ionization Time-of-Flight Mass Spectrometry and 2-[(2E)-3-(4-tert-Butylphenyl)-2-methylprop-2-enylidene]malononitrile Matrix. *Analytical Chemistry* **2006**, *78* (1), 199-206.
115. Jaskolla, T.; Fuchs, B.; Karas, M.; Schiller, J., The New Matrix 4-Chloro- α -Cyanocinnamic Acid Allows the Detection of Phosphatidylethanolamine Chloramines by MALDI-TOF Mass Spectrometry. *Journal of the American Society for Mass Spectrometry* **2009**, *20* (5), 867-874.
116. Wang, J.; Qiu, S.; Chen, S.; Xiong, C.; Liu, H.; Wang, J.; Zhang, N.; Hou, J.; He, Q.; Nie, Z., MALDI-TOF MS Imaging of Metabolites with a N-(1-Naphthyl) Ethylenediamine Dihydrochloride Matrix and Its Application to Colorectal Cancer Liver Metastasis. *Analytical Chemistry* **2015**, *87* (1), 422-430.
117. Fukuyama, Y.; Nakajima, C.; Furuichi, K.; Taniguchi, K.; Kawabata, S.-i.; Izumi, S.; Tanaka, K., Alkylated Trihydroxyacetophenone as a MALDI Matrix for Hydrophobic Peptides. *Analytical Chemistry* **2013**, *85* (20), 9444-9448.
118. Calvano, C. D.; Monopoli, A.; Cataldi, T. R. I.; Palmisano, F., MALDI matrices for low molecular weight compounds: an endless story? *Analytical and Bioanalytical Chemistry* **2018**, *410* (17), 4015-4038.
119. Armstrong, D. W.; Zhang, L.-K.; He, L.; Gross, M. L., Ionic Liquids as Matrixes for Matrix-Assisted Laser Desorption/Ionization Mass Spectrometry. *Analytical Chemistry* **2001**, *73* (15), 3679-3686.
120. Schiller, J.; Süß, R.; Fuchs, B.; Müller, M.; Petković, M.; Zschörnig, O.; Waschipky, H., The suitability of different DHB isomers as matrices for the MALDI-TOF MS analysis of phospholipids: which isomer for what purpose? *European Biophysics Journal* **2007**, *36* (4), 517-527.
121. Li, S.; Zhang, Y.; Liu, J. a.; Han, J.; Guan, M.; Yang, H.; Lin, Y.; Xiong, S.; Zhao, Z., Electrospray deposition device used to precisely control the matrix crystal to improve the performance of MALDI MSI. *Scientific Reports* **2016**, *6*, 37903.
122. Gemperline, E.; Rawson, S.; Li, L., Optimization and Comparison of Multiple MALDI Matrix Application Methods for Small Molecule Mass Spectrometric Imaging. *Analytical Chemistry* **2014**, *86* (20), 10030-10035.

123. Korte, A. R.; Lee, Y. J., MALDI-MS analysis and imaging of small molecule metabolites with 1,5-diaminonaphthalene (DAN). *Journal of Mass Spectrometry* **2014**, *49* (8), 737-741.
124. Grove, K. J.; Frappier, S. L.; Caprioli, R. M., Matrix Pre-Coated MALDI MS Targets for Small Molecule Imaging in Tissues. *Journal of The American Society for Mass Spectrometry* **2011**, *22* (1), 192-195.
125. Shanta, S. R.; Zhou, L.-H.; Park, Y. S.; Kim, Y. H.; Kim, Y.; Kim, K. P., Binary Matrix for MALDI Imaging Mass Spectrometry of Phospholipids in Both Ion Modes. *Analytical Chemistry* **2011**, *83* (4), 1252-1259.
126. Meriaux, C.; Franck, J.; Wisztorski, M.; Salzet, M.; Fournier, I., Liquid ionic matrixes for MALDI mass spectrometry imaging of lipids. *Journal of Proteomics* **2010**, *73* (6), 1204-1218.
127. Astigarraga, E.; Barreda-Gómez, G.; Lombardero, L.; Fresnedo, O.; Castaño, F.; Giralt, M. T.; Ochoa, B.; Rodríguez-Puertas, R.; Fernández, J. A., Profiling and Imaging of Lipids on Brain and Liver Tissue by Matrix-Assisted Laser Desorption/Ionization Mass Spectrometry Using 2-Mercaptobenzothiazole as a Matrix. *Analytical Chemistry* **2008**, *80* (23), 9105-9114.
128. Francese, S.; Bradshaw, R.; Flinders, B.; Mitchell, C.; Bleay, S.; Cicero, L.; Clench, M. R., Curcumin: A Multipurpose Matrix for MALDI Mass Spectrometry Imaging Applications. *Analytical Chemistry* **2013**, *85* (10), 5240-5248.
129. Cerruti, C. D.; Benabdellah, F.; Laprévotte, O.; Touboul, D.; Brunelle, A., MALDI Imaging and Structural Analysis of Rat Brain Lipid Negative Ions with 9-Aminoacridine Matrix. *Analytical Chemistry* **2012**, *84* (5), 2164-2171.
130. Fülöp, A.; Porada, M. B.; Marsching, C.; Blott, H.; Meyer, B.; Tambe, S.; Sandhoff, R.; Junker, H.-D.; Hopf, C., 4-Phenyl- α -cyanocinnamic Acid Amide: Screening for a Negative Ion Matrix for MALDI-MS Imaging of Multiple Lipid Classes. *Analytical Chemistry* **2013**, *85* (19), 9156-9163.
131. Patterson, N. H.; Thomas, A.; Chaurand, P., Monitoring time-dependent degradation of phospholipids in sectioned tissues by MALDI imaging mass spectrometry. *Journal of Mass Spectrometry* **2014**, *49* (7), 622-627.
132. Jaskolla, T. W.; Karas, M.; Roth, U.; Steinert, K.; Menzel, C.; Reihls, K., Comparison Between Vacuum Sublimed Matrices and Conventional Dried Droplet Preparation in MALDI-TOF Mass Spectrometry. *Journal of the American Society for Mass Spectrometry* **2009**, *20* (6), 1104-1114.
133. Zemski Berry, K. A.; Hankin, J. A.; Barkley, R. M.; Spraggins, J. M.; Caprioli, R. M.; Murphy, R. C., MALDI Imaging of Lipid Biochemistry in Tissues by Mass Spectrometry. *Chemical Reviews* **2011**, *111* (10), 6491-6512.
134. Beceiro, A.; Tomás, M.; Bou, G., Antimicrobial Resistance and Virulence: a Successful or Deleterious Association in the Bacterial World? *Clinical Microbiology Reviews* **2013**, *26* (2), 185-230.
135. Kohanski, M. A.; Dwyer, D. J.; Collins, J. J., How antibiotics kill bacteria: from targets to networks. *Nature Reviews Microbiology* **2010**, *8* (6), 423-435.
136. Muthaiyan, A.; Silverman, J. A.; Jayaswal, R. K.; Wilkinson, B. J., Transcriptional Profiling Reveals that Daptomycin Induces the *Staphylococcus aureus* Cell Wall Stress Stimulon and Genes Responsive to Membrane Depolarization. *Antimicrobial Agents and Chemotherapy* **2008**, *52* (3), 980-990.
137. Slavetinsky, C.; Kuhn, S.; Peschel, A., Bacterial aminoacyl phospholipids – Biosynthesis and role in basic cellular processes and pathogenicity. *Biochimica et Biophysica Acta (BBA) - Molecular and Cell Biology of Lipids* **2017**, *1862* (11), 1310-1318.

138. Cheng, A. G.; Kim, H. K.; Burts, M. L.; Krausz, T.; Schneewind, O.; Missiakas, D. M., Genetic requirements for *Staphylococcus aureus* abscess formation and persistence in host tissues. *FASEB journal : official publication of the Federation of American Societies for Experimental Biology* **2009**, *23* (10), 3393-3404.
139. Ernst, C. M.; Staubitz, P.; Mishra, N. N.; Yang, S.-J.; Hornig, G.; Kalbacher, H.; Bayer, A. S.; Kraus, D.; Peschel, A., The Bacterial Defensin Resistance Protein MprF Consists of Separable Domains for Lipid Lysinylation and Antimicrobial Peptide Repulsion. *PLOS Pathogens* **2009**, *5* (11), e1000660.
140. Ernst, C. M.; Peschel, A., MprF-mediated daptomycin resistance. *International Journal of Medical Microbiology* **2019**, *309* (5), 359-363.
141. Baltz, R. H., Daptomycin: mechanisms of action and resistance, and biosynthetic engineering. *Current Opinion in Chemical Biology* **2009**, *13* (2), 144-151.
142. Mishra, N. N.; Bayer, A. S., Correlation of Cell Membrane Lipid Profiles with Daptomycin Resistance in Methicillin-Resistant *Staphylococcus aureus*. *Antimicrobial Agents and Chemotherapy* **2013**, *57* (2), 1082-1085.
143. Perry, W. J.; Spraggins, J. M.; Sheldon, J. R.; Grunenwald, C. M.; Heinrichs, D. E.; Cassat, J. E.; Skaar, E. P.; Caprioli, R. M., *Staphylococcus aureus* exhibits heterogeneous siderophore production within the vertebrate host. *Proceedings of the National Academy of Sciences* **2019**, 201913991.
144. Blanc, L.; Lenaerts, A.; Dartois, V.; Prideaux, B., Visualization of Mycobacterial Biomarkers and Tuberculosis Drugs in Infected Tissue by MALDI-MS Imaging. *Analytical Chemistry* **2018**, *90* (10), 6275-6282.
145. Scott, A. J.; Post, J. M.; Lerner, R.; Ellis, S. R.; Lieberman, J.; Shirey, K. A.; Heeren, R. M. A.; Bindila, L.; Ernst, R. K., Host-based lipid inflammation drives pathogenesis in *Francisella* infection. *Proceedings of the National Academy of Sciences* **2017**, *114* (47), 12596-12601.
146. Spraggins, J. M.; Djambazova, K. V.; Rivera, E. S.; Migas, L.; Neumann, E. K.; Fuetterer, A.; Suetering, J.; Goedecke, N.; Ly, A.; Van de Plas, R.; Caprioli, R. M., High Performance Molecular Imaging with MALDI Trapped Ion Mobility Time-of-Flight (timsTOF) Mass Spectrometry. *Analytical Chemistry* **2019**.
147. Niehaus, M.; Soltwisch, J.; Belov, M. E.; Dreisewerd, K., Transmission-mode MALDI-2 mass spectrometry imaging of cells and tissues at subcellular resolution. *Nature Methods* **2019**, *16* (9), 925-931.
148. Prentice, B. M.; Ryan, D. J.; Van de Plas, R.; Caprioli, R. M.; Spraggins, J. M., Enhanced Ion Transmission Efficiency up to m/z 24 000 for MALDI Protein Imaging Mass Spectrometry. *Analytical Chemistry* **2018**, *90* (8), 5090-5099.
149. Lin, L.-E.; Chen, C.-L.; Huang, Y.-C.; Chung, H.-H.; Lin, C.-W.; Chen, K.-C.; Peng, Y.-J.; Ding, S.-T.; Wang, M.-Y.; Shen, T.-L.; Hsu, C.-C., Precision biomarker discovery powered by microscopy image fusion-assisted high spatial resolution ambient ionization mass spectrometry imaging. *Analytica Chimica Acta* **2020**, *1100*, 75-87.
150. Thuny, F.; Grisoli, D.; Collart, F.; Habib, G.; Raoult, D., Management of infective endocarditis: challenges and perspectives. *The Lancet* **2012**, *379* (9819), 965-975.
151. Cahill, T. J.; Baddour, L. M.; Habib, G.; Hoen, B.; Salaun, E.; Pettersson, G. B.; Schäfers, H. J.; Prendergast, B. D., Challenges in Infective Endocarditis. *Journal of the American College of Cardiology* **2017**, *69* (3), 325-344.

152. Pettersson, G. B.; Hussain, S. T.; Shrestha, N. K.; Gordon, S.; Fraser, T. G.; Ibrahim, K. S.; Blackstone, E. H., Infective endocarditis: An atlas of disease progression for describing, staging, coding, and understanding the pathology. *The Journal of Thoracic and Cardiovascular Surgery* **2014**, *147* (4), 1142-1149.e2.
153. Yao, D.; Yu, F.-y.; Qin, Z.-q.; Chen, C.; He, S.-s.; Chen, Z.-q.; Zhang, X.-q.; Wang, L.-x., Molecular characterization of *Staphylococcus aureus* isolates causing skin and soft tissue infections (SSTIs). *BMC Infectious Diseases* **2010**, *10* (1), 133.
154. Staubitz, P.; Neumann, H.; Schneider, T.; Wiedemann, I.; Peschel, A., MprF-mediated biosynthesis of lysylphosphatidylglycerol, an important determinant in staphylococcal defensin resistance. *FEMS Microbiology Letters* **2004**, *231* (1), 67-71.
155. Duthie, E. S.; Lorenz, L. L., Staphylococcal Coagulase: Mode of Action and Antigenicity. *Microbiology* **1952**, *6* (1-2), 95-107.
156. Corbin, B. D.; Seeley, E. H.; Raab, A.; Feldmann, J.; Miller, M. R.; Torres, V. J.; Anderson, K. L.; Dattilo, B. M.; Dunman, P. M.; Gerads, R.; Caprioli, R. M.; Nacken, W.; Chazin, W. J.; Skaar, E. P., Metal Chelation and Inhibition of Bacterial Growth in Tissue Abscesses. *Science* **2008**, *319* (5865), 962-965.
157. Aisen, P.; Leibman, A.; Zweier, J., Stoichiometric and site characteristics of the binding of iron to human transferrin. *Journal of Biological Chemistry* **1978**, *253* (6), 1930-7.
158. Neilands, J. B., A Crystalline Organo-iron Pigment from a Rust Fungus (*Ustilago sphaerogena*)¹. *Journal of the American Chemical Society* **1952**, *74* (19), 4846-4847.
159. Ahmed, E.; Holmström, S. J. M., Siderophores in environmental research: roles and applications. *Microbial biotechnology* **2014**, *7* (3), 196-208.
160. Saha, M.; Sarkar, S.; Sarkar, B.; Sharma, B. K.; Bhattacharjee, S.; Tribedi, P., Microbial siderophores and their potential applications: a review. *Environmental Science and Pollution Research* **2016**, *23* (5), 3984-3999.
161. Swinkels, D. W.; Kortman, G. A. M.; Tjalsma, H.; Raffatellu, M., Nutritional iron turned inside out: intestinal stress from a gut microbial perspective. *FEMS Microbiology Reviews* **2014**, *38* (6), 1202-1234.
162. Hood, M. I.; Skaar, E. P., Nutritional immunity: transition metals at the pathogen-host interface. *Nature reviews. Microbiology* **2012**, *10* (8).
163. Stubbendieck, R. M.; May, D. S.; Chevrette, M. G.; Temkin, M. I.; Wendt-Pienkowski, E.; Cagnazzo, J.; Carlson, C. M.; Gern, J. E.; Currie, C. R., Competition among nasal bacteria suggests a role for siderophore-mediated interactions in shaping the human nasal microbiota. *Applied and Environmental Microbiology* **2018**, e02406-18.
164. Nriagu, J. O.; Skaar, E. P., *Trace metals and infectious diseases*. The MIT Press: Cambridge, MA, 2015.
165. Beasley, F. C.; Marolda, C. L.; Cheung, J.; Buac, S.; Heinrichs, D. E., *Staphylococcus aureus* transporters Hts, Sir, and Sst capture iron liberated from human transferrin by Staphyloferrin A, Staphyloferrin B, and catecholamine stress hormones, respectively, and contribute to virulence. *Infection and immunity* **2011**, *79* (6), 2345-2355.
166. Konetschny-Rapp, S.; Jung, G.; Meiwes, J.; Zahner, H., Staphyloferrin A: a structurally new siderophore from staphylococci. *European Journal of Biochemistry* **1990**, *191* (1), 65-74.
167. Cheung, J.; Beasley, F. C.; Liu, S.; Lajoie, G. A.; Heinrichs, D. E., Molecular characterization of staphyloferrin B biosynthesis in *Staphylococcus aureus*. *Molecular Microbiology* **2009**, *74* (3), 594-608.

168. Yang, J.; Caprioli, R. M., Matrix Sublimation/Recrystallization for Imaging Proteins by Mass Spectrometry at High Spatial Resolution. *Analytical chemistry* **2011**, *83* (14), 5728-5734.
169. Dufresne, M.; Thomas, A.; Breault-Turcot, J.; Masson, J.-F.; Chaurand, P., Silver-Assisted Laser Desorption Ionization For High Spatial Resolution Imaging Mass Spectrometry of Olefins from Thin Tissue Sections. *Analytical Chemistry* **2013**, *85* (6), 3318-3324.
170. Shrum, B.; Anantha, R. V.; Xu, S. X.; Donnelly, M.; Haeryfar, S. M.; McCormick, J. K.; Mele, T., A robust scoring system to evaluate sepsis severity in an animal model. *BMC Research Notes* **2014**, *7* (1), 233.
171. Beasley, F. C.; Vinés, E. D.; Grigg, J. C.; Zheng, Q.; Liu, S.; Lajoie, G. A.; Murphy, M. E. P.; Heinrichs, D. E., Characterization of staphyloferrin A biosynthetic and transport mutants in *Staphylococcus aureus*. *Molecular Microbiology* **2009**, *72* (4), 947-963.
172. Sheldon, J. R.; Marolda, C. L.; Heinrichs, D. E., TCA cycle activity in *Staphylococcus aureus* is essential for iron-regulated synthesis of staphyloferrin A, but not staphyloferrin B: the benefit of a second citrate synthase. *Molecular Microbiology* **2014**, *92* (4), 824-839.
173. Laakso, H. A.; Marolda, C. L.; Pinter, T. B.; Stillman, M. J.; Heinrichs, D. E., A Heme-responsive Regulator Controls Synthesis of Staphyloferrin B in *Staphylococcus aureus*. *Journal of Biological Chemistry* **2016**, *291* (1), 29-40.
174. Bemis, K. D.; Harry, A.; Eberlin, L. S.; Ferreira, C.; van de Ven, S. M.; Mallick, P.; Stolowitz, M.; Vitek, O., Cardinal: an R package for statistical analysis of mass spectrometry-based imaging experiments. *Bioinformatics* **2015**, *31* (14), 2418-2420.
175. Leopold, J.; Popkova, Y.; Engel, K. M.; Schiller, J., Recent Developments of Useful MALDI Matrices for the Mass Spectrometric Characterization of Lipids. *Biomolecules* **2018**, *8* (4), 173.
176. Teuber, K.; Schiller, J.; Fuchs, B.; Karas, M.; Jaskolla, T. W., Significant sensitivity improvements by matrix optimization: a MALDI-TOF mass spectrometric study of lipids from hen egg yolk. *Chemistry and Physics of Lipids* **2010**, *163* (6), 552-560.
177. Tsai, M.-T.; Lee, S.; Lu, I.-C.; Chu, K. Y.; Liang, C.-W.; Lee, C. H.; Lee, Y. T.; Ni, C.-K., Ion-to-neutral ratio of 2,5-dihydroxybenzoic acid in matrix-assisted laser desorption/ionization. *Rapid Communications in Mass Spectrometry* **2013**, *27* (9), 955-963.
178. Wang, C. C.; Lai, Y. H.; Ou, Y. M.; Chang, H. T.; Wang, Y. S., Critical factors determining the quantification capability of matrix-assisted laser desorption/ionization- time-of-flight mass spectrometry. *Philos Trans A Math Phys Eng Sci* **2016**, *374* (2079).
179. Mowry, C. D.; Johnston, M. V., Simultaneous detection of ions and neutrals produced by matrix-assisted laser desorption. *Rapid Communications in Mass Spectrometry* **1993**, *7* (7), 569-575.
180. Kostrzewa, M., Application of the MALDI Biotyper to clinical microbiology: progress and potential. *Expert review of proteomics* **2018**, *15* (3), 193-202.
181. Attia, A. S.; Schroeder, K. A.; Seeley, E. H.; Wilson, K. J.; Hammer, N. D.; Colvin, D. C.; Manier, M. L.; Nicklay, J. J.; Rose, K. L.; Gore, J. C.; Caprioli, R. M.; Skaar, E. P., Monitoring the inflammatory response to infection through the integration of MALDI IMS and MRI. *Cell host & microbe* **2012**, *11* (6), 664-673.
182. Glaros, T. G.; Blancett, C. D.; Bell, T. M.; Natesan, M.; Ulrich, R. G., Serum biomarkers of *Burkholderia mallei* infection elucidated by proteomic imaging of skin and lung abscesses. *Clinical Proteomics* **2015**, *12* (1), 7.

183. Negrão, F.; de O. Rocha, D. F.; Jaeger, C. F.; Rocha, F. J. S.; Eberlin, M. N.; Giorgio, S., Murine cutaneous leishmaniasis investigated by MALDI mass spectrometry imaging. *Molecular BioSystems* **2017**, *13* (10), 2036-2043.
184. Cornett, D. S.; Frappier, S. L.; Caprioli, R. M., MALDI-FTICR Imaging Mass Spectrometry of Drugs and Metabolites in Tissue. *Analytical Chemistry* **2008**, *80* (14), 5648-5653.
185. Zackular, J. P.; Moore, J. L.; Jordan, A. T.; Juttukonda, L. J.; Noto, M. J.; Nicholson, M. R.; Crews, J. D.; Semler, M. W.; Zhang, Y.; Ware, L. B.; Washington, M. K.; Chazin, W. J.; Caprioli, R. M.; Skaar, E. P., Dietary zinc alters the microbiota and decreases resistance to *Clostridium difficile* infection. *Nature Medicine* **2016**, *22*, 1330.
186. Knippel, R. J.; Zackular, J. P.; Moore, J. L.; Celis, A. I.; Weiss, A.; Washington, M. K.; DuBois, J. L.; Caprioli, R. M.; Skaar, E. P., Heme sensing and detoxification by HatRT contributes to pathogenesis during *Clostridium difficile* infection. *PLOS Pathogens* **2018**, *14* (12), e1007486.
187. Palmer, A. D.; Alexandrov, T., Serial 3D Imaging Mass Spectrometry at Its Tipping Point. *Analytical Chemistry* **2015**, *87* (8), 4055-4062.
188. Ghosal, S.; Fallon, S. J.; Leighton, T. J.; Wheeler, K. E.; Kristo, M. J.; Hutcheon, I. D.; Weber, P. K., Imaging and 3D Elemental Characterization of Intact Bacterial Spores by High-Resolution Secondary Ion Mass Spectrometry. *Analytical Chemistry* **2008**, *80* (15), 5986-5992.
189. Moreno, M. A.; Mouton, I.; Chevalier, N.; Barnes, J.-P.; Bassani, F.; Gautier, B., Combined ToF-SIMS and AFM protocol for accurate 3D chemical analysis and data visualization. *Journal of Vacuum Science & Technology B* **2018**, *36* (3), 03F122.
190. Hare, D. J.; Lee, J. K.; Beavis, A. D.; van Gramberg, A.; George, J.; Adlard, P. A.; Finkelstein, D. I.; Doble, P. A., Three-Dimensional Atlas of Iron, Copper, and Zinc in the Mouse Cerebrum and Brainstem. *Analytical Chemistry* **2012**, *84* (9), 3990-3997.
191. Van Malderen, S. J. M.; Laforce, B.; Van Acker, T.; Nys, C.; De Rijcke, M.; de Rycke, R.; De Bruyne, M.; Boone, M. N.; De Schampelaere, K.; Borovinskaya, O.; De Samber, B.; Vincze, L.; Vanhaecke, F., Three-Dimensional Reconstruction of the Tissue-Specific Multielemental Distribution within *Ceriodaphnia dubia* via Multimodal Registration Using Laser Ablation ICP-Mass Spectrometry and X-ray Spectroscopic Techniques. *Analytical Chemistry* **2017**, *89* (7), 4161-4168.
192. Van Malderen, S. J. M.; Laforce, B.; Van Acker, T.; Vincze, L.; Vanhaecke, F., Imaging the 3D trace metal and metalloid distribution in mature wheat and rye grains via laser ablation-ICP-mass spectrometry and micro-X-ray fluorescence spectrometry. *Journal of Analytical Atomic Spectrometry* **2017**, *32* (2), 289-298.
193. Caprioli, R. M., Imaging Mass Spectrometry: A Perspective. *J Biomol Tech* **2019**, *30* (1), 7-11.
194. Ryan, D. J.; Spraggins, J. M.; Caprioli, R. M., Protein identification strategies in MALDI imaging mass spectrometry: a brief review. *Current opinion in chemical biology* **2019**, *48*, 64-72.

CURRICULUM VITAE

William J. Perry

Nashville, TN (931)206-6779

wjperry22@gmail.com

LinkedIn: [linkedin.com/in/william-perry-64969699/](https://www.linkedin.com/in/william-perry-64969699/)

DISSERTATION ABSTRACT

Infection and disease are rooted in chemical changes at or below the cellular level. Many of the causative chemical changes that result in potentially deadly conditions localize to specific structures or cells within tissues such as cancerous tumors or infectious foci. This research leverages imaging mass spectrometry (IMS), a technology that allows for visualization of molecular distributions from a tissue section, in combination with other imaging modalities for interrogation of *Staphylococcus aureus* tissue infections. *S. aureus* pathogenic molecular responses to circumvent innate or nutritional immunity were mapped across multiple sites of infection. IMS in tandem with other imaging modalities increase the information attainable from these infections. Research of host-pathogen interactions, such as this, is imperative to increase understanding of microbial pathogen proliferation to ultimately devise alternative therapeutics for treatment of infectious diseases.

Education

Jan. 2016 – July 2020

Doctor of Philosophy, Vanderbilt University (Nashville, TN)

Imaging Mass Spectrometry of *Staphylococcus aureus* Infection: Mapping Pathogenic Adaptations that Circumvent Host Nutritional and Innate Immunity

Mentors: Dr. Richard M. Caprioli, Dr. Eric P. Skaar, & Dr. Jeffrey M. Spraggins

(Expected Completion June 2020)

Aug. 2011 – Dec. 2015

Bachelor of Science in Chemistry: Biochemistry, University of Tennessee at Chattanooga (Chattanooga, TN)

Analysis and quantification of defensive alkaloid compounds in *Coccinella septempunctata*

Mentor: Dr. Manuel Santiago

Previous Employment

May 2014 – Apr. 2015

Chemist Internship, Tandus Centiva (Dalton, GA)

Develop and perform quality control GC-MS on recycled polymers used in manufacturing carpet backing

Manager: Adam Grasham

Publications

Perry, W. J.; Grunenwald, C. M.; Witten, J. C.; Martin, D.; Apte, S.; Pettersson, G. B.; Peschel, A.; Cassat, J.; Spraggins, J. M.; Skaar, E. P.; Caprioli R. M., Multimodal imaging of the infectious interface maps heterogeneous *S. aureus* pathogenic membrane modification. *In Preparation*.

McMillen, J. C.; **Perry, W. J.;** Sharman, K.; Djambazova, K. V.; Caprioli, R. M., Matrix-assisted laser desorption/ionization imaging mass spectrometry: technology and applications. North American Treaty Organization Science for Peace and Security Advanced Study Institute (NATO SPS ASI) G5535; Proceedings of Detection, diagnosis, and health concerns of toxic chemical and biological agents. (Cetraro, Italy). *In Press*.

Laut, C. L.; **Perry, W. J.;** Metzger, A. L.; Weiss, A.; Stauff, D. L.; Caprioli, R. M.; Skaar, E. P., *Bacillus anthracis* responds to targocil induced envelope damage through EdsRS activation of cardiolipin synthesis. *mBio*. *Accepted*.

Perry, W. J.*; Weiss, A.*; Van de Plas, R.; Spraggins, J. M.; Caprioli, R. M.; Skaar, E. P., Integrated molecular imaging technologies for investigation of metals in biological systems: a brief review. *Current Opinion in Chemical Biology* **2020**, 55, 127-135.

Perry, W. J.; Patterson, N. H.; Prentice, B. M.; Neumann, E. K.; Caprioli, R. M.; Spraggins, J. M., Uncovering matrix effects on lipid analyses in MALDI imaging mass spectrometry experiments. *Journal of Mass Spectrometry* **2019**, e4491.

Ryan, D. J.; Patterson, N. H.; Putnam, N. E.; Wilde, A. D.; Weiss, A.; **Perry, W. J.;** Cassat, J. E.; Skaar, E. P.; Caprioli, R. M.; Spraggins, J. M., MicroLESA: Integrating Autofluorescence Microscopy, In Situ Micro-Digestions, and Liquid Extraction Surface Analysis for High Spatial Resolution Targeted Proteomic Studies. *Analytical Chemistry* **2019**, 91 (12), 7578-7585.

Perry, W. J.; Spraggins, J. M.; Sheldon, J. R.; Grunenwald, C. M.; Heinrichs, D. E.; Cassat, J. E.; Skaar, E. P.; Caprioli, R. M., *Staphylococcus aureus* exhibits heterogeneous siderophore production within the vertebrate host. *Proceedings of the National Academy of Sciences* **2019**, 201913991.

Cassat, J. E.; Moore, J. L.; Wilson, K. J.; Stark, Z.; Prentice, B. M.; Van de Plas, R.; **Perry, W. J.;** Zhang, Y.; Virostko, J.; Colvin, D. C.; Rose, K. L.; Judd, A. M.; Reyzer, M. L.; Spraggins, J. M.; Grunenwald, C. M.; Gore, J. C.; Caprioli, R. M.; Skaar, E. P., Integrated molecular imaging reveals tissue heterogeneity driving host-pathogen interactions. *Science Translational Medicine* **2018**, 10 (432), ean6361.

Oral Presentations

Oct. 2019

North American Treaty Organization Science for Peace and Security Advanced Study Institute (NATO SPS ASI) G5535; Detection, diagnosis, and health concerns of toxic chemical and biological agents. (Cetraro, Italy)

- Multimodal imaging to visualize staphylococcal molecular adaptation within the infectious microenvironment
- Apr. 2019 **Advanced Imaging Mass Spectrometry Course, Special Topics Speaker**
Multimodal IMS technologies to interrogate the host-pathogen interface
- April 2019 **2019 Mass Spectrometry Applied to the Clinical Lab 11th Annual Conference**
Multimodal imaging mass spectrometry technologies to visualize staphylococcal molecular adaptation within the infectious microenvironment
- Mar. 2018 **Vanderbilt Chemistry Department Student Third Year Seminar Series**
Investigating the Host-Pathogen Infectious Interface Using Multimodal Imaging

Awards

- Aug. 2019 **2019 Vanderbilt Institute for Chemical Biology Symposium Poster Award**
- Apr. 2019 **2019 Mass Spectrometry Applied to the Clinical Lab 11th Annual Conference Young Investigator Travel Award**
- Sept. 2018 **AbbVie Analytical Research Symposium 2018 Attendee**
- Jan. 2018 **2018 Mass Spectrometry Applied to the Clinical Lab 10th Annual Conference Young Investigator Travel Award**
- Jan. 2018 **2018 Mass Spectrometry Applied to the Clinical Lab 10th Annual Conference Poster Award**
- 2016 **Aegis Training Grant Recipient**

Teaching Experience

- June 2019 **Aspirnaut High School Summer Internships (Vanderbilt University)**
Assisted in mentoring Mariham Mousa from STEM Prep High School (Nashville, TN) in her project: Impact of Age on Metal Concentration in the Lens
- Apr. 2019 **Advanced Imaging Mass Spectrometry (AIMS) Course Workshop Leader (Vanderbilt University)**

- IMS Data Analysis Using SCiLS
Matrix Application: TM Sprayer
Sample Preparation with Fresh Frozen Tissue: Washing and Staining
- Oct. 2018 **Mass Spectrometry Research Center Lecture Series (Vanderbilt University)**
Cell Phenotyping and Imaging Techniques: Using Antibody Probes for Analysis by Mass Spectrometry
- Apr. 2018 **Advanced Imaging Mass Spectrometry (AIMS) Course Workshop Leader (Vanderbilt University)**
IMS Data Analysis Using SCiLS
Matrix Application: TM Sprayer
- Advanced Imaging Mass Spectrometry (AIMS) Course Workshop Assistant (Vanderbilt University)**
Sample Preparation with Fresh Frozen Tissue: Washing and Staining
- May 2017 **Mass Spectrometry Research Center Lecture Series (Vanderbilt University)**
Native Mass Spectrometry
- Apr. 2017 **Advanced Imaging Mass Spectrometry (AIMS) Course Workshop Assistant (Vanderbilt University)**
Matrix Application: TM Sprayer
- Jan. 2016 – May 2016 **Teaching Assistant, Chemistry II Laboratory (Vanderbilt University)**
- Aug. 2015 – Dec. 2015 **Teaching Assistant, Chemistry I Laboratory & Physical Chemistry I: Thermodynamics Laboratory (University of Tennessee at Chattanooga)**

Poster Presentations
(W.J.P. presenter)

William J. Perry, Caroline M. Grunenwald, Jessica R. Sheldon, Jeffrey M. Spraggins, Eric P. Skaar, and Richard M. Caprioli. *Multimodal MALDI IMS to Visualize Staphylococcal Molecular Adaptation within the Infectious Microenvironment*. **North American Treaty Organization Science for Peace and Security Advanced Study Institute (NATO SPS ASI) G5535; Detection, diagnosis, and health concerns of toxic chemical and biological agents**; 2019 October; Cetraro, Italy.

William J. Perry, Caroline M. Grunenwald, Jessica R. Sheldon, Jeffrey M. Spraggins, Eric P. Skaar, and Richard M. Caprioli. *Multimodal MALDI IMS to Visualize Staphylococcal Molecular*

Adaptation within the Infectious Microenvironment. 2019 Vanderbilt Institute for Chemical Biology (VICB) Student Research Symposium; 2019 August; Nashville, TN.

William J. Perry, Caroline M. Grunenwald, Jessica R. Sheldon, Jeffrey M. Spraggins, Eric P. Skaar, and Richard M. Caprioli. *Multimodal MALDI IMS to Visualize Staphylococcal Molecular Adaptation within the Infectious Microenvironment. 67th American Society for Mass Spectrometry (ASMS) Conference on Mass Spectrometry*; 2019 June; Atlanta, GA.

William J. Perry, Caroline M. Grunenwald, Jessica R. Sheldon, Jeffrey M. Spraggins, Eric P. Skaar, and Richard M. Caprioli. *Multimodal MALDI IMS to Visualize Staphylococcal Molecular Adaptation within the Infectious Microenvironment. 2019 Vanderbilt Institute for Infection, Immunology, and Inflammation (VI4) Annual Symposium*; 2019 April; Nashville, TN.

William J. Perry, Caroline Grunenwald, N. Heath Patterson, Jessica L. Moore, Boone M. Prentice, James E. Cassat, Eric p. Skaar, Jeffrey M. Spraggins, Richard M. Caprioli. *Molecular Definition of the Infectious Microenvironment Using Multi-modal MALDI Imaging Mass Spectrometry. 2018 AbbVie Analytical Research Symposium*; 2018 August; North Chicago, IL.

William J. Perry, Caroline Grunenwald, N. Heath Patterson, Audra M. Judd, Jessica L. Moore, Danielle Gutierrez, Carrie Romer, James E. Cassat, Eric P. Skaar, Jeffrey M. Spraggins, Richard M. Caprioli. *Comparing molecular abundance at the host-pathogen interface using multi-modal MALDI imaging mass spectrometry. 2018 Vanderbilt Institute for Chemical Biology (VICB) Student Research Symposium*; 2018 August; Nashville, TN.

William J. Perry, N. Heath Patterson, Caroline Grunenwald, Jessica L. Moore, Boone M. Prentice, James E. Cassat, Raf Van de Plas, Eric P. Skaar, Jeffrey M. Spraggins, Richard M. Caprioli. *Molecular insight into the lipidome of the staphylococcal infectious interface using multi-modal MALDI imaging mass spectrometry. 2018 Vanderbilt Institute for Infection, Immunology, and Inflammation (VI4) Annual Symposium*; 2018 April; Nashville, TN.

William J. Perry, N. Heath Patterson, Jessica R. Sheldon, Jessica L. Moore, Caroline Grunenwald, Boone M. Prentice, James E. Cassat, Raf Van de Plas, Eric P. Skaar, Jeffrey M. Spraggins, Richard M. Caprioli. *Visualizing differential molecular abundance at the host-pathogen interface using imaging mass spectrometry. Mass Spectrometry Applied to the Clinical Laboratory (MSACL) 2018 US 10th Annual Conference*; 2018 January; Palm Springs, CA.

William J. Perry, Jeffrey M. Spraggins, N. Heath Patterson, Marissa Jones, Boone M. Prentice, Raf Van de Plas, Richard M. Caprioli. *Global lipidomic changes associated with MALDI matrices using MALDI FTICR imaging mass spectrometry. 2017 Vanderbilt Institute for Chemical Biology (VICB) Student Research Symposium*; 2017 August; Nashville, TN.

William J. Perry, Jeffrey M. Spraggins, N. Heath Patterson, Marissa Jones, Boone M. Prentice, Raf Van de Plas, Richard M. Caprioli. *Global lipidomic changes associated with MALDI matrices using MALDI FTICR imaging mass spectrometry. 65th American Society*

for Mass Spectrometry (ASMS) Conference on Mass Spectrometry; 2017 June;
Indianapolis, IN.

William Perry, Yukie Kajita, Manuel Santiago. *Ladybirds: Detection and determination of alkaloid compounds*. **Southeast Regional Meeting of the American Chemistry Society – Southwest Regional Meeting (SERMACS-SWRM); 2015 November; Memphis, TN.**